



Publicly Accessible Penn Dissertations


1-1-2012

Semiconductor Nanowires: Optical Properties and All-Optical Switching

Brian Edward Piccione

University of Pennsylvania, brian.piccione@gmail.com

Follow this and additional works at: <http://repository.upenn.edu/edissertations>

 Part of the [Mechanics of Materials Commons](#), [Nanoscience and Nanotechnology Commons](#), and the [Optics Commons](#)

Recommended Citation

Piccione, Brian Edward, "Semiconductor Nanowires: Optical Properties and All-Optical Switching" (2012). *Publicly Accessible Penn Dissertations*. 560.

<http://repository.upenn.edu/edissertations/560>

This paper is posted at ScholarlyCommons. <http://repository.upenn.edu/edissertations/560>

For more information, please contact libraryrepository@pobox.upenn.edu.

Semiconductor Nanowires: Optical Properties and All-Optical Switching

Abstract

The optical properties of semiconductor nanowires are both important from a fundamental materials physics standpoint and necessary to understand in engineering applications: nanowire photovoltaic devices, sensors, and lasers, among others, could all benefit. Unfortunately, these optical properties are not easy to ascertain. Transmission times are short, in-coupling of white probe light is difficult, and the angle-resolved measurements typically used to determine material dispersion relations in bulk materials are hindered by diffraction effects at subwavelength nanowire end facets.

Here, we present a series of experimental techniques and theoretical models developed to study of the optical properties of active nanowire waveguides. Beginning with a technique for determining the waveguide dispersion of individual ZnSe nanowires, we demonstrate enhanced properties with respect to bulk material. After investigating propagation loss in individual CdS nanowires, the theoretical model was then refined to quantify the strength of light-matter coupling, where size-dependence was observed. The knowledge gained from these studies was put to use in the first demonstration of all-optical switching in individual semiconductor nanowires. The switch concept was then extended into an all-optical nanowire NAND gate. These developments highlight the importance of semiconductor nanowires as both model materials systems and novel devices.

Degree Type

Dissertation

Degree Name

Doctor of Philosophy (PhD)

Graduate Group

Materials Science & Engineering

First Advisor

Ritesh Agarwal

Keywords

CdS, Materials, Nanophotonics, Nanowires, Optics, Polaritons

Subject Categories

Mechanics of Materials | Nanoscience and Nanotechnology | Optics

SEMICONDUCTOR NANOWIRES:
OPTICAL PROPERTIES AND ALL-OPTICAL SWITCHING

Brian Piccione

A DISSERTATION

in

Materials Science and Engineering

Presented to the Faculties of the University of Pennsylvania

in

Partial Fulfillment of the Requirements for the

Degree of Doctor of Philosophy

2012

Supervisor of Dissertation

Signature _____

Ritesh Agarwal, Associate Professor, Materials Science and Engineering

Graduate Group Chairperson

Signature _____

Russell Composto, Associate Professor, Materials Science and Engineering

Dissertation Committee

Dawn Bonnell, Trustees Chair Professor, Materials Science and Engineering

Ertugrul Cubukcu, Assistant Professor, Materials Science and Engineering

Arjun Yodh, James M. Skinner Professor of Science, Physics

SEMICONDUCTOR NANOWIRES: OPTICAL PROPERTIES AND ALL-OPTICAL
SWITCHING

COPYRIGHT

2012

Brian Edward Piccione

ACKNOWLEDGEMENT

I would like to acknowledge all the support I've received for the past five years. My father Ed, my mother Michele, and my brothers Matt and Ed have always been there for support. Christine Fox was an inspiration and gave me the strength to keep going. In no particular order, I'd like to thank everyone else who's helped me along the way: Rose Mutiso and Mike Deaven, Mark and Mindy Licurse, Dave Kim and Jenica Abram, Kristen Metkus, Kate Murphy, Lisa Chen, Anindita Basu, Matt Caporizzo, Dagny Fleischman, Pat Overend, Profs. Russ Composto, Peter Davies, Cherie Kagan, and John Blendell, Bart and Lauren Burgess, Mike Burke, Nick Luciano, Alexandria and Aaron Coble, Kasey and Jill Soska, Mike Willis, Rob Huber, Ryan and Karisa Greecher, Sarah Selzer and Jason Pfeiger, Kate Hoch, Michael Kovach, Jason Lally, Abigail Fox, Heather Hurst, Jasmine Malik, Nicole Marotta, Jenn DeLuca, David Ewoldt, Nikki Cooper, and Matt Stanford.

I'd like to thank my dissertation committee: Profs. Dawn Bonnell, Ertugrul Cubukcu, and Arjun Yodh. My adviser, Prof. Ritesh Agarwal, has made all of this possible, and I will always be grateful for his guidance. From the Agarwal group: Drs. Lambert K van Vugt, Chang-Hee Cho, Yeonwoong Jung, and Chris Rodd, Aaron Wirshba, Carlos Aspetti, Joohee Park, Pavan Nukala, Rahul Agarwal, Siddharth Ghosh, Karthik Kumar, Tyler Zimmerman, Thomas Walsh, and Andrew Jennings.

Finally, I would like to thank Kate Huber and Temple University for saving me countless trips to Penn's archives.

ABSTRACT

SEMICONDUCTOR NANOWIRES:

OPTICAL PROPERTIES AND ALL-OPTICAL SWITCHING

Brian Piccione

Ritesh Agarwal

The optical properties of semiconductor nanowires are both important from a fundamental materials physics standpoint and necessary to understand in engineering applications: nanowire photovoltaic devices, sensors, and lasers, among others, could all benefit. Unfortunately, these optical properties are not easy to ascertain. Transmission times are short, in-coupling of white probe light is difficult, and the angle-resolved measurements typically used to determine material dispersion relations in bulk materials are hindered by diffraction effects at subwavelength nanowire end facets.

Here, we present a series of experimental techniques and theoretical models developed to study of the optical properties of active nanowire waveguides. Beginning with a technique for determining the waveguide dispersion of individual ZnSe nanowires, we demonstrate enhanced properties with respect to bulk material. After investigating propagation loss in individual CdS nanowires, the theoretical model was then refined to quantify the strength of light-matter coupling, where size-dependence was observed. The knowledge gained from these studies was put to use in the first demonstration of all-

optical switching in individual semiconductor nanowires. The switch concept was then extended into an all-optical nanowire NAND gate. These developments highlight the importance of semiconductor nanowires as both model materials systems and novel devices.

TABLE OF CONTENTS

Chapter 1.	Introduction.....	1
1.1.	Semiconductor nanowires.....	1
1.2.	Optical properties of optically active semiconductor nanowires	4
1.3.	All-optical switching in semiconductor nanowires.....	7
Chapter 2.	Nanowire Growth and Experimental Methods	18
Chapter 3.	Size-Dependent Waveguide Dispersion in Nanowire Optical Cavities.....	24
3.1.	Experimental procedures	25
3.2.	Numerical calculations.....	29
3.3.	Discussion.....	30
Chapter 4.	Propagation Loss Spectroscopy on Single Nanowire Active Waveguides.	40
4.1.	Experimental procedures	41
4.2.	Discussion.....	47
Chapter 5.	Variable Temperature Spectroscopy of As-Grown and Passivated CdS Nanowire Waveguide Cavities	58
5.1.	Experimental methods	60
5.2.	Results and discussion	60
Chapter 6.	Incorporating Polaritonic Effects in Semiconductor Nanowire Waveguide Dispersion	81
Chapter 7.	One-Dimensional Polaritons With Size-Tunable and Enhanced Coupling Strengths in Semiconductor Nanowires.....	91
7.1.	Materials and methods	93
7.2.	Experimental results.....	93
7.3.	Numerical mode volume calculations.....	97
7.4.	Analysis of enhanced oscillator strengths.....	100
Chapter 8.	All-Optical Active Switching in Individual Semiconductor Nanowires ..	109
8.1.	Experimental setup.....	110
8.2.	Results.....	113

8.3. Analysis of switching mechanisms	115
Chapter 9. Future Work	127
Chapter 10. Conclusions.....	133

LIST OF TABLES

Table 4.1: Diameter, length, and propagation loss coefficients at 2.525 eV.	52
--	----

LIST OF ILLUSTRATIONS

Figure 1.1: Schematic of the vapor-liquid-solid (VLS) growth mechanism.	3
Figure 1.2: Field intensity distribution for the fundamental waveguide mode inside glass-rod-in-air photonic nanowires for various sub-micron core radii and a wavelength of 800 nm.	10
Figure 2.1: SEM image of CdS nanowires as grown and TEM image of single nanowire transferred onto a carbon lace sample grid.	19
Figure 2.2: Micro-photoluminescence setup used in most optical measurements.	21
Figure 3.1: a) Scanning electron microscopy image of a ZnSe nanowire dispersed onto a 300nm thick SiO ₂ covered Si wafer.	27
Figure 3.2: a) SEM images of four ZnSe nanowires having radii of 110, 100, 90 and 80 nm and lengths of 5.98, 2.08, 11.51 and 22.28 μm respectively (left to right). Scale bars are 100 nm.	32
Figure 3.3: Emission spectra acquired from the ends of nanowires with radii of 75, 65, 50 and 40 nm and lengths of 8.52, 8.02, 33.15 and 14.01 μm respectively, with increasing diameters from top to bottom trace, and dispersion of the HE ₁₁ mode of the nanowires with radii of 75 nm, 65 nm, 50 nm, and 40 nm, respectively.	34
Figure 3.4: Emission spectrum acquired from the end of a nanowire, mode dispersion, and group index obtained by differentiating the mode dispersions	36

Figure 4.1: Scanning electron microscopy images of three CdS nanowires dispersed onto a 300 nm thick SiO ₂ -covered Si wafer on which optical measurements were performed, and real color optical image of a CdS nanowire under focused 458 nm Ar+ laser illumination.	43
Figure 4.2: Illustration of CdS nanowire under focused 458nm Ar+ laser excitation at 300 K, spatially resolved excitation images obtained at energies 2.304 and 2.440 eV, and normalized intensity vs. distance of the excitation laser from the end facet line profiles extracted from the spatially resolved images.	45
Figure 4.3: Propagation loss spectrum at 300 K, plotted alongside photoluminescence from nanowire end facets.	47
Figure 4.4: Propagation loss spectrum at a cryostat-reported temperature of 77.6 K, obtained by plotting propagation loss coefficient as a function of energy. A waveguided photoluminescence spectrum from the same nanowire, exhibiting longitudinal Fabry-Pérot resonances, is also shown.	49
Figure 4.5: Propagation loss spectra at 77.6 K, ordered according to propagation loss coefficient at 2.525 eV.	52
Figure 4.6: Photoluminescence and dispersion for a nanowire at a cryostat-reported temperature of 77.6 K.	54
Figure 5.1: SEM image of the nanowire growth substrate, SEM image of an individual nanowire, on the optical measurement substrate, and an x-ray diffractogram of a CdS nanowire.	62

Figure 5.2: Spatially resolved optical measurement geometry, reflected white light microscopy image of a single CdS nanowire, and photoluminescence image of a nanowire.....	64
Figure 5.3: Room temperature photoluminescence spectra of body emission and end emission of an unpassivated CdS nanowire, and 77.6 K photoluminescence spectra of body emission and end emission.....	66
Figure 5.4: Photoluminescence spectra of body and end emission of an unpassivated CdS wire over the 77.6 K to 298 K temperature range.....	68
Figure 5.5: TEM image of a 5 nm SiO ₂ ALD coated CdS nanowire, and fourier transform infrared absorption (FTIR) spectrum of an ensemble of SiO ₂ passivated (blue line) and unpassivated (black line) CdS nanowires.	70
Figure 5.6: Room temperature photoluminescence spectra of body emission and end emission of an unpassivated CdS nanowire, and 77.6 K photoluminescence spectra of body emission and end emission.....	72
Figure 5.7: Photoluminescence spectra of body and end emissions of a SiO ₂ coated CdS wire over the 77.6 K to 298 K temperature range, and temperature dependence of the observed photoluminescence peaks	74
Figure 5.8: Photoluminescence spectra of body and end emissions of a SiO ₂ coated CdS wire at 77.6 K, and propagation loss spectrum of this same wire.	76

Figure 6.1: Waveguide dispersion for the waveguide modes of a CdS nanowire with a radius of 120 nm calculated using a Sellmeier equation for material dispersion and the polaritonic model	84
Figure 6.2: Emission spectra of guided photoluminescence light for multiple nanowires.	87
Figure 6.3: Group index vs. energy for purely photonic and polaritonic modes of two nanowires	88
Figure 7.1: CdS nanowire waveguide cavity and low-temperature spatially-resolved micro-photoluminescence experimental geometry	95
Figure 7.2: Photoluminescence spectra of the guided emission and size-dependent light-matter coupling strength.	96
Figure 7.3: Numerical mode volume calculations of CdS nanowire waveguide cavities.	99
Figure 7.4: The transition from the bulk-polariton to the confined cavity-polariton regime.	102
Figure 7.5: $n \times f$ for nanowires in the constant coupling strength regime plotted against real nanowire volume V	104
Figure 8.1: Creation of on-chip laser light sources for optical switching.....	111

Figure 8.2: PL spectrum collected from nanowire end facet at 4.1 K showing laser emission at 2.527 eV, consistent with known literature values for exciton-exciton lasing in CdS nanowires..	112
Figure 8.3: All optical active switching in CdS nanowires	114
Figure 8.4: Photoluminescence collected from the center of a passivated CdS nanowire held at 77K under different applied pump powers.....	116
Figure 8.5: Photoluminescence spectra collected from bottommost facet of a nanowire illustrating the determination of the switching mechanism	118
Figure 8.6: Mechanism of switching phenomena in CdS nanowires.....	121
Figure 8.7: All optical nanowire NAND gate.....	123
Figure 9.1: Illustration of scanning detection experiment setup.....	129
Figure 9.2: SEM image of CdS nanowire cut using a focused beam of gallium ions. ...	130

MAIN TEXT

Chapter 1. **Introduction**

Portions in preparation for submission to Philosophical Magazine.

1.1. Semiconductor nanowires

Semiconductor nanowires, one-dimensional semiconductor structures with nanometer-scale dimensions, have received significant attention in the last decade.¹ First synthesized by Wagner and Ellis in 1964,² the novel nanostructures have since been proposed as active components, and interconnects, in a multitude of nanoscale devices: biosensors,^{3, 4} gas sensors,⁵⁻⁷ nanogenerators,^{8, 9} light-emitting diodes,^{10, 11} electrically-driven lasers,¹² solar cells,¹³ and complete programmable circuits¹⁴ have all been demonstrated. Benefits gained from high-surface-to-volume ratios, as well as electrical or optical confinement in the radial direction, are easily accessible via connections to nanowire long axes, making nanowires the ideal morphology for many of these applications. While nanowire synthesis cannot yet produce large-scale integrated systems as complex as those possible via “top-down” fabrication methods, where bulk material is reduced in size to desired dimensions, the “bottom-up” methods utilized in nanowire synthesis, which rely on self-assembly of molecular components by principles of molecular recognition, typically result in high yields with consistent physical properties and comparatively superior surface conditions.¹⁵

Among the most common synthesis methods, solution growth offers the potential for high-volume synthesis at near-ambient environmental conditions,¹⁶ but low length-to-diameter aspect ratios and poor control over vertical alignment when deposited on

substrates currently limit its utility in integrated device applications. Electrochemical deposition in combination with nanoporous templates (e.g., anodic aluminum oxide) can produce much higher aspect ratios at comparably inexpensive environmental conditions;¹⁷ however, the crystals which result are typically either amorphous or polycrystalline in nature, somewhat limiting their potential in electronic applications and severely hindering their utility in optical applications. When semiconductor nanowires possessing both high aspect ratios and crystalline quality are desired, the most reliable method is currently the same as that first used by Wagner and Ellis, known as the vapor-liquid-solid (VLS) process.

As shown in Figure 1.1, the VLS mechanism can be described as a two-step process.¹⁸ After small metal clusters are deposited on the desired growth substrate, the assembly is placed in a reaction tube and heated until the clusters melt: frequently achieved by the metal forming an alloy with the substrate, with a reduced melting point compared to the pure metal. A gas containing the semiconductor growth material is then introduced to the reaction tube and begins to saturate the liquid alloy. When this alloy reaches the point of supersaturation, the semiconductor component is expelled at the liquid/substrate interface, resulting in vertical growth of the desired semiconductor nanowire crystal. Nanowire composition, morphology, and orientation can all be controlled through variations on the basic technique: superlattice structures can be produced by alternating the vapor phase reactants,¹⁹ core/shell structures can be produced by altering vapor phase pressure to induce radial growth,²⁰ and substrate lattice matching can be used for epitaxial growth.²¹ In addition to this, the size of the metal particles as

deposited determines final nanowire diameters, and controlled placement²² can be used to create ordered arrays.

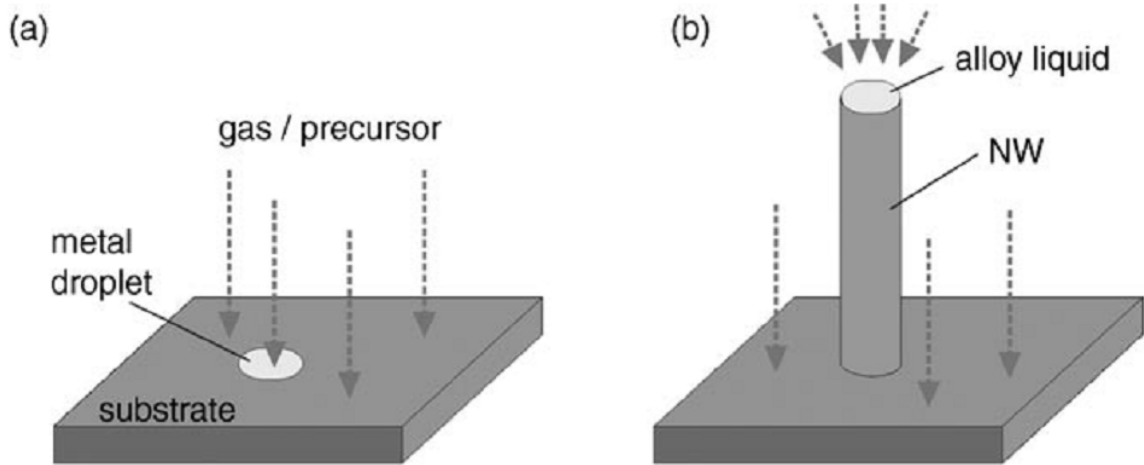


Figure 1.1: Schematic of the vapor-liquid-solid (VLS) growth mechanism. **a)** A substrate coated with metal clusters is heated until the metal melts, and gas containing the desired nanowire material is introduced to the growth chamber. **b)** Upon supersaturation, the droplet expels material at the substrate surface, resulting in vertical nanowire growth.¹⁸

Control over physical properties of nanowires during growth subsequently allows for control over properties: among many others, electrical,²³ magnetic,²⁴ thermal,²⁵ and mechanical²⁶ properties are all altered in the nanowire form. Most relevant to this dissertation, however, are the optical properties of nanowires. Section 1.2 discusses these properties in more detail, while Section 1.3 details a novel exploitation of the enhanced optical properties: all-optical switching in individual semiconductor nanowires.

1.2. Optical properties of optically active semiconductor nanowires

In regards to optical properties, self-assembled, single-crystalline nanowires occupy an important niche among nanostructure morphologies. Due to a high refractive index mismatch with their surroundings, semiconductor nanowires with diameters in the subwavelength regime can strongly confine optical waves in the radial direction while guiding light in the axial direction,^{27, 28} a unique combination which makes them ideally suited for the development of many nanophotonic systems including modulators,²⁹ switches,³⁰ probes,³¹ and sensors.³² Achieving the full potential of nanowire systems, however, requires a fundamental understanding of how properties vary as a function of size, and the size dependence of nanowire optical phenomena was, until recently, poorly covered in the literature. While photoluminescence,³³ optically-pumped lasing,^{34, 35} waveguiding,³⁶ and photoconductivity,³⁷ for example, have been extensively documented in individual nanowires, explicit studies of these phenomena and their underlying physical causes as a function of size have only recently reached sufficient volume for critical meta-analysis. Massively parallel synthesis methods^{38, 39} resulting in large quantities of nanowires per batch allow for a higher probability of obtaining a single suitable crystal demonstrating a novel phenomenon, but systematic study as a function of size has significantly more stringent requirements. In addition to controlled synthesis of consistently high-quality, single-crystalline nanostructures of narrow size distribution, optical studies of individual nanowires have an additional barrier towards actuation in that their diameters are typically smaller than the wavelengths of light utilized in far-field optical analysis.

The resulting diffraction limitations in this one dimension certainly do not preclude study of all optical properties, and indeed, the earliest studies of optical properties (e.g. effects of quantum confinement⁴⁰ and non-radiative surface recombination⁴¹ on luminescence) were not hindered by this issue. However, a comprehensive, quantitative analysis of light-matter interaction within any condensed matter system requires knowledge of the full energy-wavevector dispersion relation, and its measurement of this which is made difficult by the nanowire geometry. Direct measurements are commonly performed by angle-resolved transmission or emission experiments^{42, 43} and time-resolved transmission experiments can measure its derivative, the group velocity.⁴⁴ For nanowires these measurements are hindered by the scrambling effect of the subwavelength apertures at the wire ends due to diffraction,⁴⁵ the short transmission times involved⁴⁶ and the difficulty of in-coupling of probe light with a large energy and wavevector distribution.⁴⁷

The complete energy-wavevector dispersion relation is ultimately defined by both the nanowire geometry and the materials system, and in the case of active optical materials, resonant coupling between the light field and the material considerably complicates waveguide behavior in comparison with passive waveguides. It is known that due to the substantially larger oscillator strength of electron-hole pairs (excitons) than that of free electron and hole (band to band) recombination, excitons can strongly couple to the light field resulting in the formation of composite quasiparticles with both electronic and photonic character known as exciton-polaritons.⁴⁸ Energy oscillates back and forth between the excitonic and photonic states with what is known as the Rabi frequency, which is expressed by the formation of anti-crossing upper and lower

polariton branches (UPB and LPB) in the material dispersion relation, and drastic changes to the dielectric function. It is through this polaritonic coupling mechanism, as well as effects such as giant exciton oscillator strength and superradiance effects,^{49, 50} that finite crystal sizes comparable to the optical wavelengths can result in material dispersion that is significantly different from that of macroscopic crystals.⁵¹

Among materials which exhibit polaritonic effects, popular choices for active nanowire waveguides include ZnO, ZnSe, CdS, GaN, and SnO₂, all semiconductors exhibiting a relatively high refractive index, a direct electronic bandgap, and the formation of excitons as dictated by their relatively large exciton binding energies.⁵² Nanowires of two different semiconducting materials were synthesized for the purposes of this dissertation. The material used in Chapter 3 is zinc selenide (ZnSe), a direct bandgap II-VI semiconductor which has been employed in both light-emitting^{53, 54} and detecting⁵⁵ configurations, as well as transmissive optical components due to its generally low absorption coefficient in the infrared.⁵⁶ The following chapters, however, focus on cadmium sulfide (CdS), another direct bandgap II-VI semiconductor which has been extensively studied in bulk⁵⁷⁻⁶⁰ where it has been established that in its wurtzite crystal structure, the crystal field and spin-orbit coupling⁶¹⁻⁶³ cause the valence band to split into three levels, giving rise to A, B, and C excitons. Due to a high exciton binding energy of 27 meV⁶⁴ and high oscillator strengths of 1.84 and 1.35 meV for the A and B excitons, respectively,^{65, 66} these excitons can couple strongly to the optical field, significantly altering the dielectric function and waveguide dispersion of the material.⁶⁷ Signatures of exciton-polaritons such as strong dispersion,⁶⁸ reduced group velocity⁶⁹ and increased band edge absorption⁷⁰ have been found in numerous studies on bulk CdS crystals.

Though the groundwork for obtaining complete dispersion relations from individual nanowires was first laid by van Vugt et al.⁷¹ using ZnO,⁷² and the resulting experimental waveguide dispersion relation was also found to be substantially modified from bulk material, the size-dependence data and analysis tools necessary to draw quantitative conclusions regarding the strength of light-matter enhancement in the nanowire morphology were not yet available before the work presented in this dissertation. Following a brief overview of our experimental setup in Chapter 2, Chapter 3 presents the first use of the analytical tools developed by van Vugt to obtain size-dependent data from ZnSe nanowires. Chapter 4, details a method for obtaining propagation losses in individual nanowires, Chapter 5 discusses a surface passivation method which led to improved optical properties, and Chapter 6 details refinements to the theoretical waveguide model which allows for quantification of light-matter coupling strength enhancement. In Chapter 7, all previous developments are combined for a quantitative size-dependent study of light-matter coupling in CdS nanowires, unambiguously showing the transition from bulk- to cavity-polaritons for the first time.

1.3. All-optical switching in semiconductor nanowires

The condition in which two different output intensities are possible for a given optical input intensity, traditionally defined as optical bistability,^{73, 74} was first described theoretically and observed experimentally using an absorptive optical nonlinearity by Szoke *et al* in 1969.⁷⁵ Though the condition can manifest in vapors⁷⁶ and soft matter,⁷⁷ optical bistability in semiconductors⁷⁸ in particular was the subject of intense interest in the 1980s and early 1990s for its potential for use in digital optical computers based upon

solid-state optically bistable elements.⁷⁹ Though digital optical computers offer the potential advantage of very short switching times and massive parallelism in data processing,⁸⁰ interest in their development gradually faded due in part to the elements' power disadvantages when compared with their all-electronic counterparts.⁸¹ The power requirements of these early devices were not symptomatic of optical bistability itself, rather, they were a consequence of the necessity for strong optical nonlinearity, which itself benefits from high optical intensities. When combined with suitable feedback, this nonlinearity will give rise to a static hysteresis loop in the relation between incident and transmitted (or reflected) light intensities characteristic of optically bistable systems.

More recently, computing applications of photonics have regained relevance. Imminent bandwidth limitations of electronic integrated circuits⁸² is stimulating intense activity in the area of nanophotonics for the development of on-chip optical components, and solutions incorporating direct bandgap semiconductors are important to this end.⁸³ The exciting prospects of optical processing⁸⁴ and interconnects⁸⁵ require a large toolbox of high-performance components that includes emitters, detectors, modulators, waveguides and switches. Semiconductor nanowires with superior surface properties⁸⁶ and strong optical confinement in comparison to components fabricated via top-down methods can serve as both candidates for nanowire-based optical networks,⁸⁷ as well as model systems for furthering the understanding of optical processes in confined structures.⁸⁸

As mentioned earlier, high power requirements are not an inherent flaw of optically bistable systems, rather, the high optical intensities necessary to bring about nonlinear optical effects themselves have high power requirements in bulk materials.

Additionally, achieving these high intensities in bulk materials requires tight focusing, which leads to a shortened light-matter interaction length due to the reduced confocal parameter.⁸⁹ Attempts to circumvent these issues thus far have resulted in various integrated solutions, including vertical-cavity optical amplifiers⁹⁰ and ring resonators,⁹¹ all of which show promise but can exhibit an unnecessarily large footprint. Various hybrid electro-optic switches⁹²⁻⁹⁴ and even electro-optic nanowire modulators⁹⁵ have been realized, but these devices cannot fully exploit the speed advantages offered by all-optical counterparts and would be incompatible with an all-optical circuit architecture.

Within the realm of all-optical devices, the nanowire waveguide geometry is an ideal structure for minimizing the input power needed to induce bistability since it both maximizes light confinement in the radial direction and provides an effective light-matter interaction length as long as the nanowire itself. Though dielectric contrast between the waveguide core (refractive index n_{core}) and its cladding (refractive index n_{clad}) ceases to tightly confine light beneath a certain critical radius r_c where evanescent fields begin to dominate, as shown in Figure 1.1, even the modest contrast between a glass rod ($n_{core}=1.42$) and air ($n_{clad}=1$) provides maximal fundamental waveguide mode light intensity for radii well below a micron. The empirical relationship for r_c (Equation 1.1)⁹⁶,⁹⁷ makes explicit that for a given vacuum wavelength λ the critical radius is inversely proportional to the quantity $n_{core}-n_{clad}$: simply increasing the core refractive index to $n_{core}=2.2$ while maintaining air cladding yields r_c well below 100 nm for blue light.

Glass rod in air: $\lambda = 800$ nm, circular cross-section

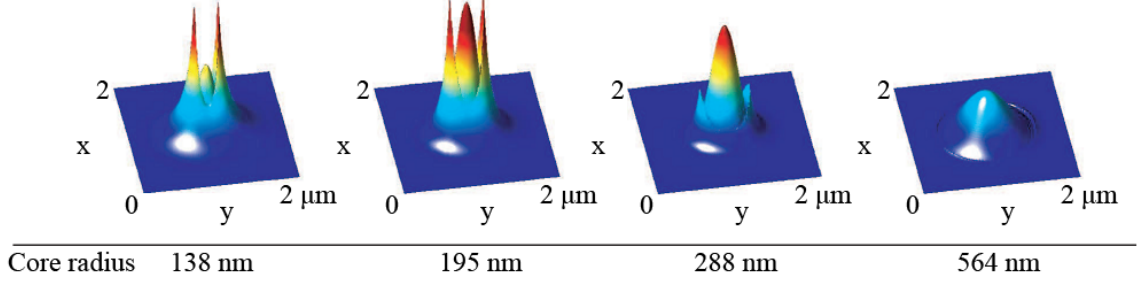


Figure 1.2: Field intensity distribution for the fundamental waveguide mode inside glass-rod-in-air photonic nanowires for various sub-micron core radii and a wavelength of 800 nm. The field confinement increases as the core is reduced until a point where the evanescent field dominates. This critical radius at which maximal intensity is reached decreases as dielectric contrast between the core and its cladding is increased.⁸⁹

$$r_c = \sqrt{\frac{0.573\lambda^2}{\pi(n_{core} + n_{clad})^{1.2}(n_{core} - n_{clad})^{0.8}}} \quad \text{Eq. 1.1}$$

Upon reaching sufficient intensity, nonlinear interactions will begin to occur between the light and a nonlinear waveguide medium, and in the case of a semiconducting nanowire core, these interactions can occur through many different physical mechanisms. Though the specific mechanism is currently thought to lie outside of those traditionally associated with the term “optical bistability,” Chapter 8 details, for the first time, optically driven active switching in individual CdS nanowire cavities with sub-wavelength dimensions via stimulated polariton scattering mechanism which relies on the intense fields maintained in the highly confining structures. In addition to this, we demonstrate a functional nanowire NAND gate built from multiple switches. The unique device designs utilize very strong light-matter coupling in nanowires and therefore result in total footprints a fraction that of comparable silicon-based dielectric contrast^{98, 99} and

photonic crystal¹⁰⁰ devices, demonstrating a practical application of the physics explored elsewhere in this dissertation.

References

1. Lu, W. & Lieber, C.M. Semiconductor nanowires. *Journal of Physics D: Applied Physics* **39**, R387 (2006).
2. Wagner, R.S. & Ellis, W.C. Vapor-Liquid-Solid Mechanism of Single Crystal Growth. *Applied Physics Letters* **4**, 89-90 (1964).
3. Yeh, P.-H., Li, Z. & Wang, Z.L. Schottky-Gated Probe-Free ZnO Nanowire Biosensor. *Advanced Materials* **21**, 4975-4978 (2009).
4. Zhang, G.-J. et al. Highly sensitive measurements of PNA-DNA hybridization using oxide-etched silicon nanowire biosensors. *Biosensors and Bioelectronics* **23**, 1701-1707 (2008).
5. Wan, Q. et al. Fabrication and ethanol sensing characteristics of ZnO nanowire gas sensors. *Applied Physics Letters* **84**, 3654-3656 (2004).
6. Cvelbar, U., Ostrikov, K., Drenik, A. & Mozetic, M. Nanowire sensor response to reactive gas environment. *Applied Physics Letters* **92**, 133505-3 (2008).
7. Wang, B., Zhu, L.F., Yang, Y.H., Xu, N.S. & Yang, G.W. Fabrication of a SnO₂ Nanowire Gas Sensor and Sensor Performance for Hydrogen. *The Journal of Physical Chemistry C* **112**, 6643-6647 (2008).
8. Wang, X., Song, J., Liu, J. & Wang, Z.L. Direct-Current Nanogenerator Driven by Ultrasonic Waves. *Science* **316**, 102-105 (2007).
9. Wang, Z.L. & Song, J. Piezoelectric Nanogenerators Based on Zinc Oxide Nanowire Arrays. *Science* **312**, 242-246 (2006).
10. Bao, J., Zimmler, M.A., Capasso, F., Wang, X. & Ren, Z.F. Broadband ZnO Single-Nanowire Light-Emitting Diode. *Nano Letters* **6**, 1719-1722 (2006).
11. Konenkamp, R., Word, R.C. & Schlegel, C. Vertical nanowire light-emitting diode. *Applied Physics Letters* **85**, 6004-6006 (2004).
12. Duan, X., Huang, Y., Agarwal, R. & Lieber, C.M. Single-nanowire electrically driven lasers. *Nature* **421**, 241-245 (2003).
13. Law, M., Greene, L.E., Johnson, J.C., Saykally, R. & Yang, P. Nanowire dye-sensitized solar cells. *Nat Mater* **4**, 455-459 (2005).
14. Yan, H. et al. Programmable nanowire circuits for nanoprocessors. *Nature* **470**, 240-244 (2011).
15. Lu, W. & Lieber, C.M. Nanoelectronics from the bottom up. *Nat Mater* **6**, 841-850 (2007).
16. Choy, J.H. et al. Soft Solution Route to Directionally Grown ZnO Nanorod Arrays on Si Wafer; Room-Temperature Ultraviolet Laser. *Advanced Materials* **15**, 1911-1914 (2003).
17. Routkevitch, D., Bigioni, T., Moskovits, M. & Xu, J.M. Electrochemical Fabrication of CdS Nanowire Arrays in Porous Anodic Aluminum Oxide Templates. *The Journal of Physical Chemistry* **100**, 14037-14047 (1996).
18. Fan, H.J., Werner, P. & Zacharias, M. Semiconductor Nanowires: From Self-Organization to Patterned Growth. *Small* **2**, 700-717 (2006).

19. Gudiksen, M.S., Lauhon, L.J., Wang, J., Smith, D.C. & Lieber, C.M. Growth of nanowire superlattice structures for nanoscale photonics and electronics. *Nature* **415**, 617-620 (2002).
20. Lauhon, L.J., Gudiksen, M.S., Wang, D. & Lieber, C.M. Epitaxial core-shell and core-multishell nanowire heterostructures. *Nature* **420**, 57-61 (2002).
21. Wu, Z.H., Mei, X.Y., Kim, D., Blumin, M. & Ruda, H.E. Growth of Au-catalyzed ordered GaAs nanowire arrays by molecular-beam epitaxy. *Applied Physics Letters* **81**, 5177-5179 (2002).
22. Jensen, L.E. et al. Role of Surface Diffusion in Chemical Beam Epitaxy of InAs Nanowires. *Nano Letters* **4**, 1961-1964 (2004).
23. Long, Y. et al. Electrical conductivity of single CdS nanowire synthesized by aqueous chemical growth. *Applied Physics Letters* **86**, 153102-3 (2005).
24. Zeng, H. et al. Magnetic properties of self-assembled Co nanowires of varying length and diameter. *Journal of Applied Physics* **87**, 4718-4720 (2000).
25. Li, D. et al. Thermal conductivity of individual silicon nanowires. *Applied Physics Letters* **83**, 2934-2936 (2003).
26. San Paulo, Á. et al. Suspended Mechanical Structures Based on Elastic Silicon Nanowire Arrays. *Nano Letters* **7**, 1100-1104 (2007).
27. Tong, L., Lou, J. & Mazur, E. Single-mode guiding properties of subwavelength-diameter silica and silicon wire waveguides. *Optics Express* **12**, 1025 (2004).
28. Tong, L. et al. Subwavelength-diameter silica wires for low-loss optical wave guiding. *Nature (London)* **426**, 816-819 (2003).
29. Andrew, B.G., Carl, J.B., Yat, L. & Charles, M.L. Semiconductor nanowire laser and nanowire waveguide electro-optic modulators. *Applied Physics Letters* **87**, 151103 (2005).
30. Piccione, B., Cho, C.-H., Vugt, L.K.v. & Agarwal, R. All-Optical Active Switching in Individual Semiconductor Nanowires. *Submitted* (2012).
31. Nakayama, Y. et al. Tunable nanowire nonlinear optical probe. *Nature* **447**, 1098 (2007).
32. Sirbulu, D.J., Tao, A., Law, M., Fan, R. & Yang, P. Multifunctional Nanowire Evanescent Wave Optical Sensors. *Advanced Materials* **19**, 61-66 (2007).
33. Wang, J., Gudiksen, M.S., Duan, X., Cui, Y. & Lieber, C.M. Highly Polarized Photoluminescence and Photodetection from Single Indium Phosphide Nanowires. *Science* **293**, 1455-1457 (2001).
34. Johnson, J.C. et al. Single gallium nitride nanowire lasers. *Nat Mater* **1**, 106-110 (2002).
35. Agarwal, R., Barrelet, C.J. & Lieber, C.M. Lasing in Single Cadmium Sulfide Nanowire Optical Cavities. *Nano Letters* **5**, 917-920 (2005).
36. Barrelet, C.J., Greytak, A.B. & Lieber, C.M. Nanowire Photonic Circuit Elements. *Nano Letters* **4**, 1981-1985 (2004).
37. Soci, C. et al. ZnO Nanowire UV Photodetectors with High Internal Gain. *Nano Letters* **7**, 1003-1009 (2007).
38. Morales, A.M. & Lieber, C.M. A Laser Ablation Method for the Synthesis of Crystalline Semiconductor Nanowires. *Science* **279**, 208-211 (1998).

39. Holmes, J.D., Johnston, K.P., Doty, R.C. & Korgel, B.A. Control of Thickness and Orientation of Solution-Grown Silicon Nanowires. *Science* **287**, 1471-1473 (2000).
40. Gudiksen, M.S., Wang, J. & Lieber, C.M. Size-Dependent Photoluminescence from Single Indium Phosphide Nanowires. *The Journal of Physical Chemistry B* **106**, 4036-4039 (2002).
41. Shalish, I., Temkin, H. & Narayanamurti, V. Size-dependent surface luminescence in ZnO nanowires. *Physical Review B* **69**, 245401 (2004).
42. Freude, W., Hui-Hai, Y. & H. Zhi-Jian. Propagation Constant and Waveguide Dispersion of Single-Mode Fibers Measured from the Far-Field. *Journal of Lightwave Technology* **6**, 318-322 (1988).
43. Houdré, R. et al. Measurement of Cavity-Polariton Dispersion Curve from Angle-Resolved Photoluminescence Experiments. *Physical Review Letters* **73**, 2043 (1994).
44. Thévenaz, L. Slow and fast light in optical fibres. *Nature Photonics* **2**, 474 (2008).
45. Vugt, L.K.v., Rühle, S. & Vanmaekelbergh, D. Phase-correlated non-directional laser emission from ZnO nanowires. *Nanoletters* **6**, 2707-2711 (2006).
46. Krauss, T.F. Why do we need slow light? *Nature Photonics* **2**, 448 (2008).
47. Voss, T. et al. High Order Waveguide Modes in ZnO Nanowires. *Nanoletters* **7**, 3675-3680 (2007).
48. Hopfield, J.J. Theory of the contribution of Excitons to the Complex Dielectric Constant of Crystals. *Physical Review* **112**, 1555-1567 (1958).
49. Gil, B. & Kavokin, A.V. Giant exciton-light coupling in ZnO quantum dots. *Applied Physics Letters* **81**, 748-750 (2002).
50. Scheibner, M. et al. Superradiance of quantum dots. *Nature Physics* **3**, 106-110 (2007).
51. Vugt, L.K.v. et al. Exciton-Polaritons Confined in a ZnO Nanowire Cavity. *Physical Review Letters* **97**, 147401 (2006).
52. Agarwal, R. Heterointerfaces in Semiconductor Nanowires. *Small* **4**, 1872 - 1893 (2008).
53. Ryall, M.D. & Allen, J.W. Exciton emission from forward-biased zinc selenide Schottky diodes. *Journal of Physics and Chemistry of Solids* **34**, 2137-2141 (1973).
54. Ding, J. et al. Excitonic gain and laser emission in ZnSe-based quantum wells. *Physical Review Letters* **69**, 1707 (1992).
55. Hitoshi, I., Tomoki, A., Nariyuki, F., Hirofumi, K. & Koshi, A. Stable avalanche-photodiode operation of ZnSe-based p⁺-n structure blue-ultraviolet photodetectors. *Applied Physics Letters* **76**, 1069-1071 (2000).
56. Deneuve, A., Tanner, D. & Holloway, P.H. Optical constants of ZnSe in the far infrared. *Physical Review B* **43**, 6544 (1991).
57. Thomas, D.G. & Hopfield, J.J. Exciton Spectrum of Cadmium Sulfide. *Physical Review* **116**, 573 (1959).
58. Thomas, D.G. & Hopfield, J.J. Optical Properties of Bound Exciton Complexes in Cadmium Sulfide. *Physical Review* **128**, 2135 (1962).

59. Shalimova, K.V. & Khirin, V.N. Mechanism for the optical absorption of Cadmium Sulfide. *Soviet Physics Journal* **12**, 487-491 (1969).
60. Broser, I., Rosenzweig, M., Broser, R., Richard, M. & Birkicht, E. A Quantitative Study of Excitonic Polariton Reflectance in CdS. *Phys. Stat. Sol.* **90**, 77 (1978).
61. Birman, J.L. *Physical Review Letters* **2**, 157 (1959).
62. Birman, J.L. *Journal of Physics and Chemistry of Solids* **8**, 35 (1959).
63. Birman, J.L. *Physical Review* **114**, 1490 (1959).
64. Anedda, A. & Fortin, E. Temperature Shift of Excitons in CdS. *Phys. Stat. Sol.* **36**, 385 (1976).
65. Koteles, E.S. & Winterling, G. Direct Measurement of Three-Branch Exciton-Polariton Dispersion in CdS. *Physical Review Letters* **44**, 948 (1980).
66. Voigt, J., Sengner, M. & Ruckmann, I. Quantitative Analysis of Interference Structures in the Transmission Spectrum of Very Thin CdS Platelets. *Phys. Stat. Sol. B* **75**, 213 (1976).
67. van Vugt, L.K., Zhang, B., Piccione, B., Spector, A.A. & Agarwal, R. Size-Dependent Waveguide Dispersion in Nanowire Optical Cavities: Slowed Light and Dispersionless Guiding. *Nano Lett.* **9**, 1684-1688 (2009).
68. Dagenais, M. & Sharfin, W.F. Measurement of the Damping Dispersion of Exciton Polaritons in CdS. *Physical Review Letters* **58**, 1776 (1987).
69. Vlasov, G.K., Krytskii, A.V. & Cooptchenko, G.A. The Group Velocity of Light and Polaritons in CdS. *Optics Communications* **20**, 162 (1976).
70. Dutton, D. Fundamental Absorption Edge in Cadmium Sulfide. *Physical Review* **112**, 785 (1958).
71. van Vugt, L.K. et al. Exciton-Polaritons Confined in a ZnO Nanowire Cavity. *Physical Review Letters* **97**, 147401 (2006).
72. Thomas, D.G. The exciton spectrum of zinc oxide. *Journal of Physics and Chemistry of Solids* **15**, 86-96 (1960).
73. Boyd, R.W. *Nonlinear Optics* (Academic Press, New York, 2008).
74. Gibbs, H.M. *Optical Bistability: Controlling Light With Light* (eds. Liao, P.F. & Kelley, P.) (Academic Press, Orlando, 1985).
75. Szoke, A., Daneu, V., Goldhar, J. & Kurnit, N.A. Bistable Optical Element and its Applications. *Applied Physics Letters* **15**, 376-379 (1969).
76. Gibbs, H.M., McCall, S.L. & Venkatesan, T.N.C. Differential Gain and Bistability Using a Sodium-Filled Fabry-Perot Interferometer. *Physical Review Letters* **36**, 1135 (1976).
77. Noel, A.C. & Sven, T.L. Submicrosecond bistable electro-optic switching in liquid crystals. *Applied Physics Letters* **36**, 899-901 (1980).
78. Gibbs, H.M. et al. Optical bistability in semiconductors. *Applied Physics Letters* **35**, 451 (1979).
79. Peychambarian, N. & Gibbs, H.M. Optical nonlinearity, bistability, and signal processing in semiconductors. *J. Opt. Soc. Am. B* **2**, 1215-1227 (1985).
80. Smith, S.D. Optical bistability: Towards the optical computer. *Nature (London)* **307**, 315 (1984).
81. Klingshirm, C.F. *Semiconductor Optics* (Springer-Verlag, Berlin, 2007).

82. Kirchain, R. & Kimerling, L. A roadmap for nanophotonics. *Nat Photon* **1**, 303-305 (2007).
83. Roelkens, G. et al. III-V/silicon photonics for on-chip and intra-chip optical interconnects. *Laser & Photonics Reviews* **4**, 751-779 (2010).
84. Caulfield, H.J. & Dolev, S. Why future supercomputing requires optics. *Nat Photon* **4**, 261-263 (2010).
85. Integrating silicon photonics. *Nat Photon* **4**, 498-499 (2010).
86. van Vugt, L.K. et al. Variable Temperature Spectroscopy of As-Grown and Passivated CdS Nanowire Optical Waveguide Cavities. *The Journal of Physical Chemistry A* **115**, 3827-3833 (2011).
87. Barrelet, C.J., Greytak, A.B. & Lieber, C.M. Nanowire Photonic Circuit Elements. *Nano Lett.* **4**, 1981 (2004).
88. van Vugt, L.K., Piccione, B. & Agarwal, R. Incorporating polaritonic effects in semiconductor nanowire waveguide dispersion. *Applied Physics Letters* **97**, 061115 (2010).
89. Foster, M.A., Turner, A.C., Lipson, M. & Gaeta, A.L. Nonlinear optics in photonic nanowires. *Optics Express* **16**, 1300 (2008).
90. Wen, P., Sanchez, M., Gross, M. & Esener, S.C. Optical bistability in vertical-cavity semiconductor optical amplifiers. *Applied Optics* **45**, 6349 (2006).
91. Almeida, V.R. & Lipson, M. Optical bistability on a silicon chip. *Optics Letters* **29**, 2387 (2004).
92. Clark, N.A. & Lagerwall, S.T. Submicrosecond bistable electro-optic switching in liquid crystals. *Applied Physics Letters* **36**, 899 (1980).
93. Lin, Y.-H., Li, J.-K., Chu, T.-Y. & Hsu, H.-K. A bistable polarizer-free electro-optical switch using a droplet manipulation on a liquid crystal and polymer composite film. *Optics Express* **18**, 10104 (2010).
94. Sirleto, L., Petti, L., Mormile, P., Righini, G.C. & Abbate, G. Fast Integrated Electro-Optical Switch and Beam Deflector Based on Nematic Liquid Crystal Waveguides. *Fiber and Integrated Optics* **21**, 435 (2002).
95. Greytak, A.B., Barrelet, C.J., Li, Y. & Lieber, C.M. Semiconductor nanowire laser and nanowire waveguide electro-optic modulators. *Applied Physics Letters* **87**, 151103 (2005).
96. Foster, M.A., Moll, K.D. & Gaeta, A.L. Optimal waveguide dimensions for nonlinear interactions. *Optics Express* **12**, 2880 (2004).
97. Dimitropoulos, D., Jhaveri, R., Claps, R., Woo, J.C.S. & Jalali, B. Lifetime of photogenerated carriers in silicon-on-insulator rib waveguides. *Applied Physics Letters* **86**, 071115 (2005).
98. Xu, Q. & Lipson, M. All-optical logic based on silicon micro-ring resonators. *Opt. Express* **15**, 924-929 (2007).
99. Almeida, V.R., Barrios, C.A., Panepucci, R.R. & Lipson, M. All-optical control of light on a silicon chip. *Nature* **431**, 1081-1084 (2004).
100. Tanabe, T., Notomi, M., Mitsugi, S., Shinya, A. & Kuramochi, E. All-optical switches on a silicon chip realized using photonic crystal nanocavities. *Applied Physics Letters* **87**, 151112-3 (2005).

Chapter 2. Nanowire Growth and Experimental Methods

Though the particular details of specific experimental conditions are discussed in each chapter, an overview is provided here for the sake of providing a unified orientation. All nanowires discussed in this dissertation were synthesized via the VLS mechanism with chemical vapor deposition (CVD) used to provide the vapor. In this process, a Si wafer is cleaned and covered by a 5 nm thick metal layer using plasma sputter deposition, placed in the center of a tube furnace and annealed, during which time surface forces cause the layer to separate into droplets with a diameter distribution roughly centered around 150 nm. Early attempts at colloidal gold seeds generally did not produce satisfactory results, though this speaks more towards the nuances in our particular furnace than anything else. After cooling, solid, elemental precursors were introduced upstream of the substrate, the tube evacuated, and argon carrier gas introduced to encourage transfer.[†] The tube was then rapidly heated and held at an elevated temperature during growth, during which time precursors begin to collect in the metallic catalyst droplets. As discussed in Chapter 1, once the liquid droplets saturate, solid nanowires nucleate at the droplet/substrate interface and continue to grow as long as precursor is provided. At the end of the growth period, the furnace is cooled via forced airflow.

In order to illustrate typical growth results, CdS nanowires as-grown on a silicon substrate are shown in Figure 2.1a. Nanowires were consistently shown to be single-crystalline when transferred onto carbon lace sample grids via dry transfer and

[†] Organometallic precursors were tested, and did generally produce nanowires of appropriate size and morphology, but significant defect emission under photoluminescence showed that nanowires produced via this method were generally inferior to those produced using elemental precursors. This result is not unexpected, as incomplete dissociation of the organic group tied to organometallic precursors is known to occasionally lead to undesirable carbon incorporation in deposited thin films.¹

characterized under HRTEM (Figure 2.1b), though diameter, morphology, and length were all found to vary between individual growth sessions. Gradual refinement of growth parameters (e.g. temperature, pressure, carrier gas flow rate) and a switch from Au/Pd metallic catalyst to pure gold eventually aided in producing more uniform nanowires during a given session.

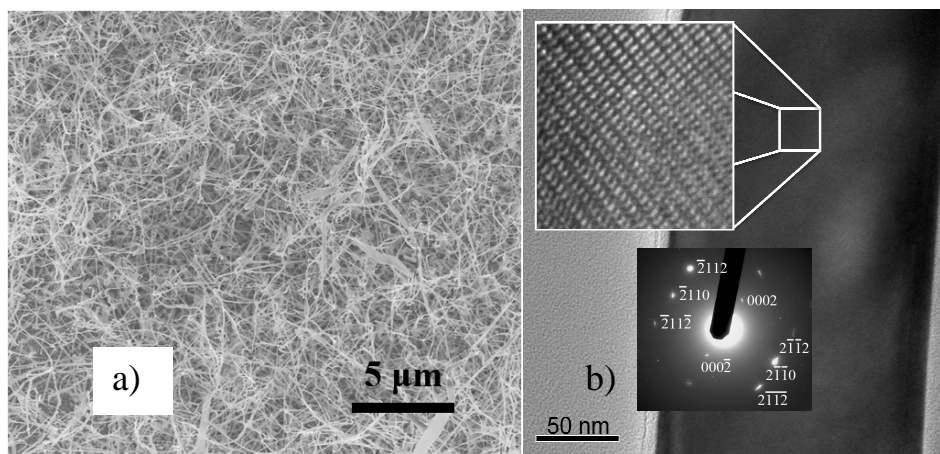


Figure 2.1: SEM image of CdS nanowires as grown **a)** and TEM image of single nanowire transferred onto a carbon lace sample grid. **b)** Top inset: Atomic resolution showing typical single-crystalline, wurtzite structure. Bottom inset: Selected area diffraction pattern showing a high-index growth orientation.

In order to optically characterize individual nanowires, wires were typically dry transferred from the growth substrate onto a marked SiO₂ substrate, a process which allows nanowires to be addressed individually against the enhanced optical contrast provided by the SiO₂ background. This presented a challenge in structural characterization once samples of interest were identified, however: the substrates are too thick for use in a TEM, and transferring individual nanowires to an electron-transparent grid with a nanomanipulator would be time-consuming and costly. Instead the

crystallographic orientation of individual nanowires with respect to growth direction was determined using an environmental SEM (FEI XL30) equipped with an electron-backscattered diffraction (EBSD) detector (see Chapter 7). Despite small interaction volumes, sufficient signal was obtained from the nanowires to both re-confirm the wurtzite CdS structure and determine growth orientation. Of the samples analyzed, most were found to grow along the crystallographic a -axis, though even wires from the same growth substrate were not consistent: some were found to grow along the crystallographic c -axis, others along higher-order axes, with no outwardly discernable difference aside from the diffraction data.

As shown in Figure 2.2, the SiO₂ substrates were typically glued with silver paint to the cold finger of a free flowing liquid nitrogen cryostat fitted with a fused silica window (Janis), so that optical measurements in the 4.2 K-298 K temperature range could be made. The spatially resolved photoluminescence excitation and detection setup consisted of a homebuilt microscope using a 60X 0.7 N.A. objective (Nikon) and an $f = 750$ mm tube lens, giving a total optical magnification of 267X. Laser light from an argon ion laser (Coherent MotoFred) at a wavelength of 457.9 nm was spatially filtered and expanded to a beam of 5 mm waist and was subsequently focused on the sample by the objective to a spot of ~800 nm waist. A frequency doubled titanium-sapphire (Ti:Sapph) laser (Coherent Chameleon Ultra II, pulse width 140 fs, repetition rate 80 MHz) was also focused on the sample for the experiments described in Chapter 8. Using piezoelectric translator stages (Physik Instrumente) holding the first lens in a telescope setup, both laser spots could be moved on the sample with an accuracy of ~50 nm. The resulting PL from the sample was collected by the same objective and was spectrally split

off by a dichroic mirror and long wavelength pass filter combination giving a detection wavelength range of 480-700 nm. A spatial resolution in the detection of ~ 500 nm could be obtained by placing an optical fiber connected to the entrance slit of 0.3 M spectrometer fitted with 150 and 600 g/m (Acton) gratings, at the projected sample plane on piezoelectric translator stages. A cooled CCD camera (Pixis 2K, Princeton Instruments) was used for detection of the dispersed light, giving a maximum wavelength resolution of ~ 0.1 nm ($500 \mu\text{eV}$).

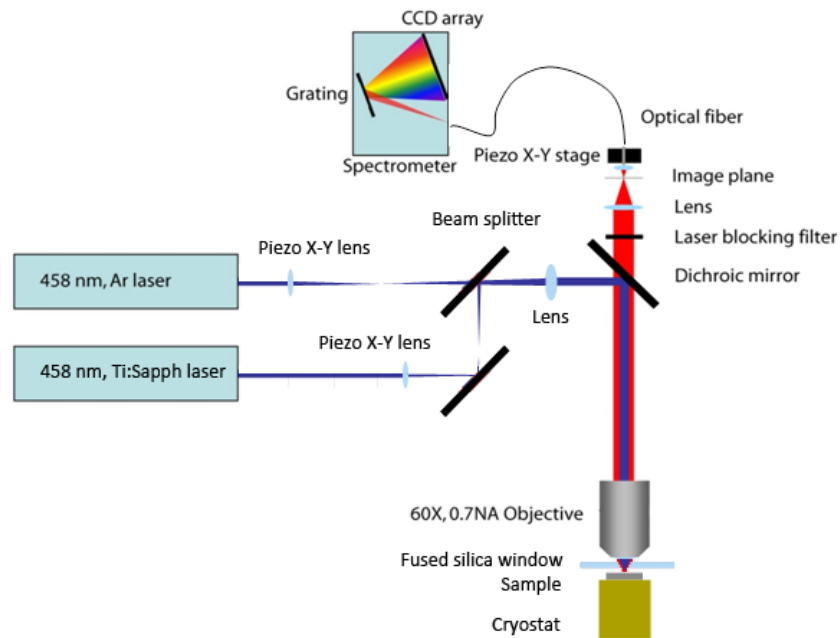


Figure 2.2: Micro-photoluminescence setup used in most optical measurements. Argon ion and titanium:sapphire laser positions on the sample surface were computer controlled with lenses mounted on piezoelectric stages. An optical fiber mounted on a third set of piezoelectric stages in the image plane was used to send photoluminescence from specific portions of the image output to a spectrometer. Samples were typically mounted on a cryostat and viewed under a 60X 0.7 N.A. objective.

Following optical measurements, data was converted, parsed, and analyzed using a number of commercial software packages. Mathematica was employed for a number of

programming tasks, Origin was generally used for plotting data, and COMSOL Multiphysics was used to model the nanowire/substrate system.

References

1. Kuech, T.F. & Veuhoff, E. Mechanism of carbon incorporation in MOCVD GaAs. *Journal of Crystal Growth* **68**, 148-156 (1984).

Chapter 3. **Size-Dependent Waveguide Dispersion in Nanowire Optical Cavities**

Reproduced in part with permission from Nano Letters, Volume 9, Issue 4, Pages 1684-1688. Copyright 2009 American Chemical Society.

Central to the appeal of utilizing semiconductor nanowires for nanophotonic applications is their ability to confine and guide light at the nanoscale, enabling functionalities such as optical transport,^{1,2} resonators,³ lasers,⁴ and sensors.⁵ By virtue of the high refractive index mismatch with their surroundings, semiconductor nanowires of subwavelength width strongly confine optical waves and are ideally suited for the development of integrated nanophotonic systems.^{6,7} The various confined optical modes propagating in dielectric nanowire waveguides are characterized by their energy-wavevector dispersion, which theory predicts to be strongly size dependent at the nanoscale.⁸ Knowledge of the size dependence of the waveguide mode dispersion is crucial for understanding the fundamental size effects of strong optical confinement and the optimal design of nanowire-based photonic devices where a specific dispersion and/or group velocity dispersion may be required. For instance, in optical communication high speed transmission with a low group velocity dispersion is desirable in order to preserve signal pulse shapes⁹ whereas slowed light would, due to increased interaction times and increased electromagnetic densities, be advantageous in optical nonlinearity based applications¹⁰ or optical sensing.¹¹

While the theoretical mode properties of dielectric (nano)fiber waveguides have been elaborately treated,^{6, 8, 12, 13} no experimental data on the size dependence of the waveguide dispersion of subwavelength dielectric nanowires has been reported. Direct measurements of the energy-wavevector dispersion are commonly performed by angle-

resolved transmission or emission experiments^{14, 15} and time-resolved transmission experiments can measure its derivative, the group velocity.¹⁶ However, for nanowires these measurements are hindered by the scrambling effect of the subwavelength apertures at the wire ends due to diffraction,¹⁷ the short transmission times involved¹⁰ and the difficulty of in-coupling of the probe light with a large energy and wavevector distribution.¹⁸

In this chapter we report on the experimentally determined strong size dependence of optical dispersion and associated group velocities in subwavelength width ZnSe nanowire waveguide cavities, using Fabry-Pérot resonator modes as probes over a wide energy range. Furthermore, we observed subwavelength ($\lambda/9$) dispersionless waveguiding and significant slowing of the propagating light by 90% ($c/8$). These results, in addition to providing insights into nanoscale optical transport, will facilitate the rational design of nanophotonic devices with dispersion and group velocity tailored towards specific functions including optical computation,¹⁹ sensing¹¹ and communication.⁹

3.1. Experimental Procedures

ZnSe nanowires were synthesized in a quartz tube furnace using evaporation of elemental Zn and Se powders. 4 mg of Se powder was placed in a quartz boat at 12.9 cm upstream (referenced to the middle of the tube), 5 mg of Zn powder was placed in a quartz boat at 9.4 cm upstream and Si substrates covered by a 5 nm thick Au/Pd layer using plasma sputter deposition were placed 16.4 cm downstream. The tube was evacuated to 20 mTorr and argon carrier gas was introduced at a flow of 20 SCCM to

reach a stable pressure of 50 Torr. The tube was rapidly heated to 1000 °C and kept there for 60 minutes after which the furnace was cooled by a forced airflow. After synthesis, the nanowires were transferred to Si substrates covered with a 300 nm thermal oxide by dry transfer. The measurement substrates were lithographically patterned to contain markers so that individual wires could be characterized by both electron and optical microscopy (Figure 3.1a). Optical experiments were carried out under the photoluminescence setup shown in Figure 2.2, using a beam expander/spatial filter to enlarge the Ar⁺ laser excitation spot to around 1 mm, giving an average excitation power density of 4 W/cm². Detail of the experimental geometry is shown in Figure 3.1b. Photoluminescence from the individual wires was spatially and spectrally resolved using the methods discussed in Chapter 2. After optical measurements, the lengths (+/-20 nm) and widths (+/-4 nm) of the nanowires were determined by Scanning Electron Microscopy (FEI Strata DB235 FIB) with the widest part of the wire taken as the width (diameter) i.e. ignoring any faceting.

A photoluminescence image of a nanowire (Figure 3.1c) shows, in addition to emission from the nanowire body, pronounced emission from the end facets. Further investigation of the nature of the body and end emission by spatially resolving the spectra shows that the emission from the nanowire body (Figure 3.1d, black trace) consists of a broad peak centered at 2.15 eV in addition to minor band-edge emission centered at 2.65 eV, characteristic of ZnSe defect emission caused by interstitial Zn ions and exciton recombination respectively.²⁰ The emission spectra obtained from the nanowire ends however show a pronounced modulation over a wide spectral range (Figure 3.1d, red and blue traces), with the modulation period inversely proportional to nanowire length

(Figure 3.1d, right inset) demonstrating that the nanowire functions as an optical Fabry-Pérot resonator along its length.

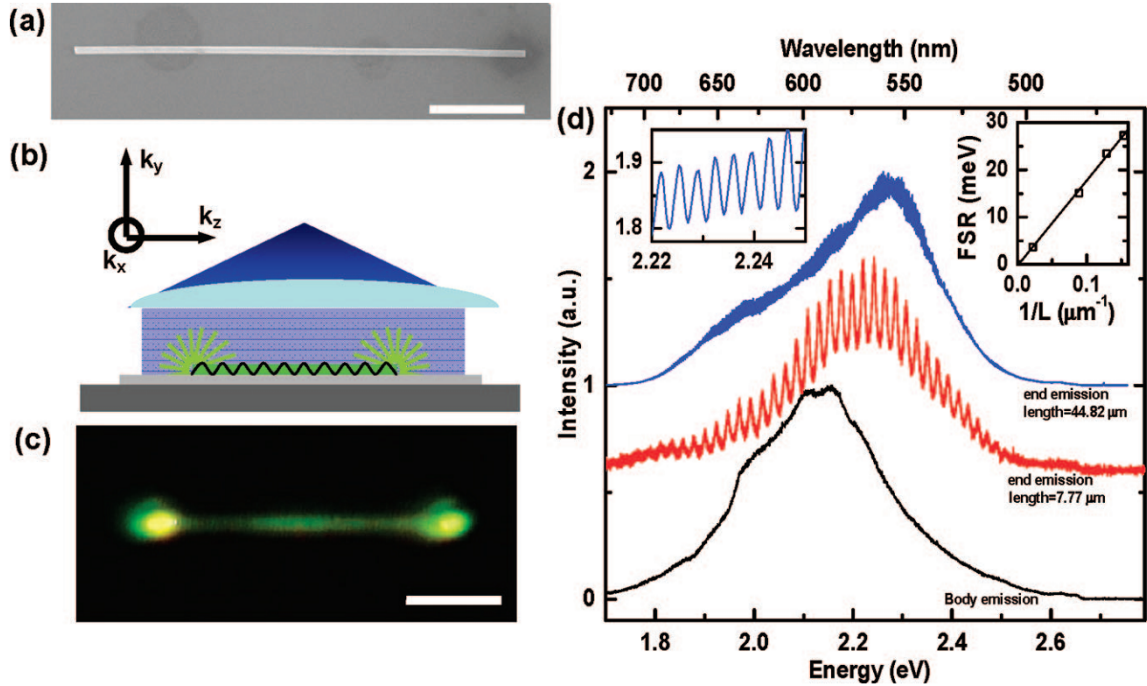


Figure 3.1: **a)** Scanning electron microscopy image of a ZnSe nanowire dispersed onto a 300 nm thick SiO_2 covered Si wafer. Scale bar, 2 μm . **b)** experimental geometry whereby the nanowire is uniformly excited perpendicular to its long axis. **c)** real color optical image of the emission of a ZnSe nanowire under uniform laser illumination. Scale bar, 2 μm . **d)** Typical emission spectra collected at the middle part of the nanowire (lower trace, black) and from the end of a 7.77 μm short nanowire (middle trace, red) and at the end of a 44.82 μm long wire (upper trace, blue) shows Fabry-Pérot modes of the nanowire resonator. A magnification of the upper trace is shown in the left inset. (Right inset) mode spacing at 2.1 eV for nanowires of comparable widths as a function of their reciprocal length, fitted by a least squares linear fit.

As introduced in Section 1.3, the internally generated light is confined due to the large refractive index mismatch between the nanowire and its surroundings and is waveguided to the ends where it is partially reflected. If the reflection at the ends of the

nanowire is sufficiently high and the losses along the length of the wire are sufficiently low, standing optical waves can develop, giving rise to interference peaks in the spectrum of the leaked light at the nanowire ends. In wavevector space these interference peaks are equally spaced at integral multiples of π/L_z (L_z , wire length).²¹ Thus, by plotting the peak positions in the energy space versus incremental wavevector multiples of π/L_z , the shape of the energy-wavevector dispersion can be determined. Since our measurements are obtained in the far-field, the absolute values of the parallel wavevectors cannot be determined. However, by comparison with theoretical calculations based on the numerical solutions of the Maxwell's equations for the measured nanowire, precise assignment of the absolute parallel wavevectors and the waveguided mode-type (e.g., hybrid-electric, transverse-electric) can be made, which also helps to identify novel nanowire dispersion features owing to their small diameters.

3.2. Numerical calculations

In order to calculate the allowed photonic modes in our nanowires, we simplified the wire geometry to a cylindrical one with a homogeneous refractive index profile inside the ZnSe core and an air cladding so that analytical expressions can be used. Since the observed interference phenomena are due to light propagating along the length of the wires, in the z -direction (confined by the surface in x and y) we calculated the mode dispersion in this direction. The propagation constant β of confined waveguide modes of a step index profile dielectric cylinder waveguide can be calculated using the following transcendental exact eigenvalue equations for the transverse electric $TE_{\nu m}$, transverse

magnetic TM_{vm} and hybrid EH_{vm} HE_{vm} modes, where the subscript v denotes the order and the subscript m denotes the m^{th} root:

$$HE_{vm} EH_{vm}: \quad \frac{J_1(U)}{UJ_0(U)} + \frac{K_1(W)}{WK_0(W)} = 0 \quad \text{Eq. 3.1}$$

$$TE_{0m}: \quad \left\{ \frac{J'_v(U)}{UJ_v(U)} + \frac{K'_v(W)}{WK_v(W)} \right\} \left\{ \frac{J'_v(U)}{UJ_v(U)} + \frac{n_{cl}^2 K'_v(W)}{n_{co}^2 WK_v(W)} \right\} = \left(\frac{v\beta}{kn_{co}} \right)^2 \left(\frac{V}{UW} \right)^4 \quad \text{Eq. 3.2}$$

$$TM_{0m}: \quad \frac{n_{co}^2 J_1(U)}{UJ_0(U)} + \frac{n_{cl}^2 K_1(W)}{WK_0(W)} = 0 \quad \text{Eq. 3.3}$$

$$\text{With:} \quad U = r\sqrt{k^2 n_{co}^2 - \beta^2} \quad \text{Eq. 3.4}$$

$$V = rk\sqrt{n_{co}^2 - n_{cl}^2} \quad \text{Eq. 3.5}$$

$$W = r\sqrt{\beta^2 - k^2 n_{cl}^2} \quad \text{Eq. 3.6}$$

and J the Bessel function of the first kind, K the modified Bessel function of the second kind, r the cylinder radius, k the free space wavevector, λ the free space wavelength n_{co} the core refractive index and n_{cl} the cladding refractive index. These equations were made specific for the ZnSe material by the inclusion of the known dispersion of the refractive index of ZnSe. The calculated propagation constant β can in general be complex; therefore in this chapter k_z was used to denote the real solutions of the eigenvalue equations. The cutoffs of the TE_{01} modes (Figure 3.2c inset, solid lines) were

obtained by setting the waveguide parameter V (optical frequency normalized to the waveguide radius) equal to 2.40512. The group velocity ($\partial\omega/\partial k_z$) was obtained by numerically differentiating the obtained mode dispersions. Since the obtained experimental data points consist of relative k_z values, typically an offset amount consisting of an integer number of (π/L_z) was added to the relative k_z values in order to obtain the absolute mode wavevectors.

3.3. Discussion

In order to examine the influence of the nanowire width on the mode dispersion, emission spectra were taken from the ends of nanowires with varying width as determined by SEM (Figure 3.2a). Figure 3.2b shows the spectra of these wires with radii of 110 nm, 100 nm, 90 and 80 nm. Aside from the different interference peak spacings caused by the different wire lengths, the spectra show a decrease in the modulation intensity towards lower energy, eventually leading to smooth and unmodulated spectra. This low energy cutoff, as is indicated by arrows, shifts to higher energy with a decrease of the nanowire width. A plot of the measured interference peaks as a function of incremental wavevector steps for the four different nanowires of different diameters is shown in Figure 3.2c. The solid lines represent the solutions of the numerically solved eigenvalue equation of an air-clad dielectric cylinder waveguide⁸ with the measured nanowire radius and the energy-dependent refractive index as determined from a bulk ZnSe crystal,²² as input parameters. The nanowire width dependence of the measured mode dispersion and their cutoffs corresponds well with the lowest order mode possessing a cutoff, the transverse electric TE_{01} mode. In the inset of Figure 3.2c the

measured TE_{01} mode cutoffs as a function of nanowire width, and hence the boundary between multi- and single mode guiding (indicated by II and I respectively) are plotted along with the results of the calculations. The good correspondence of the experimental points with the results of the calculations shows that although the nanowires are of subwavelength widths, classical electromagnetic theory can be used to predict the dispersion properties. These results also clearly demonstrate that an increase in the confinement of optical waves leads to a systematic increase in the energy of the energy-wavevector dispersions and the cut-off frequency, analogous to electron waves in quantum-confined nanostructures, but explained by purely classical optical wave phenomena.

We further investigated the nanowires in the reduced size regime where only the lowest order, single HE_{11} mode can be guided with no “theoretical” cut-off limit in order to study their size-dependence and to determine the longest wavelength that can be guided in the “practical” limit. The spectra obtained from the ends of nanowires with radii ranging from 75 nm to 40 nm (Figure 3.3a) show no low-energy cutoffs, in accordance with the theoretical predictions for the lowest order HE_{11} mode.⁸ Plots of the Fabry-Pérot mode energy maxima as a function of incremental wavevectors (Figure 3.3b-d) along with the solutions of the aforementioned eigenvalue equations show excellent agreement and demonstrate that in this size regime the dispersion is highly sensitive to nanowire width. For instance, the wire with a radius of 65 nm shows dispersion more similar to that of ZnSe whereas the wire with a radius of 50 nm shows dispersion more similar to that of the air cladding. For the smallest wire (radius of 40 nm) we find that the dispersion totally coincides with that of light in vacuum i.e. the light propagates with a

group and phase velocity equal to that of light in air. This can be understood by considering that a significant portion of optical waves in the wavelength range of 730-540 nm travels outside of the 40 nm radius nanowire, in the air cladding. It is however surprising that this light is still bound within the nanowire to complete at least one full roundtrip along the 14.01 μm long wire to display the Fabry-Pérot modes with a reasonably high quality factor of ~ 100 , suggesting sufficient mode confinement. This intriguing result shows that nanowires of extremely small widths ($\lambda/9$) can still guide light, without dispersion, which can be very useful for evanescent-wave optical sensors.

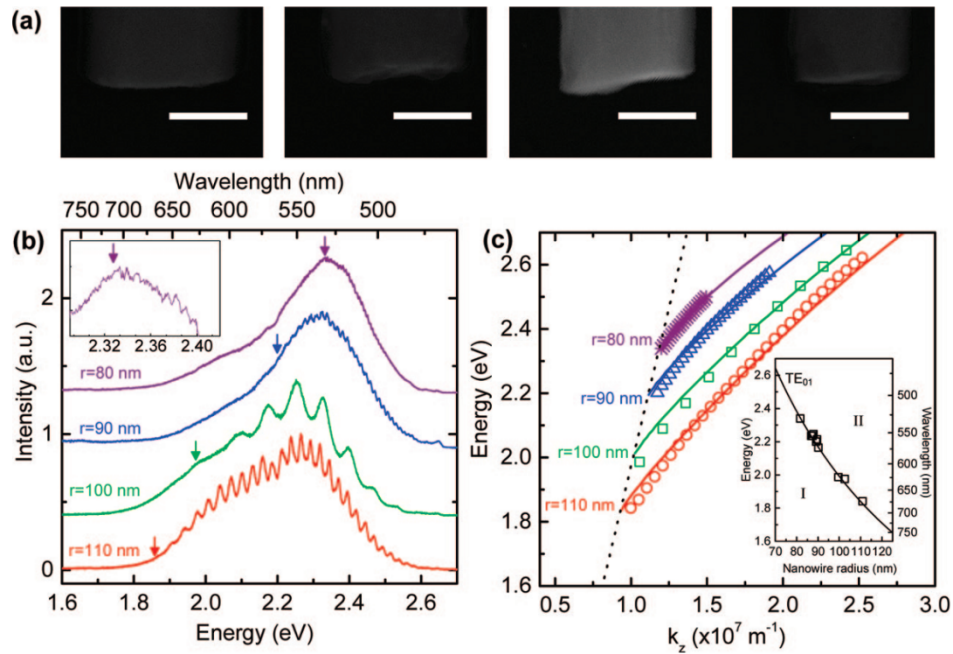


Figure 3.2: **a)** SEM images of four ZnSe nanowires having radii of 110, 100, 90 and 80 nm and lengths of 5.98, 2.08, 11.51 and 22.28 μm respectively (left to right). Scale bars are 100 nm. **b)** Emission spectra acquired from the ends of these wires with increasing diameters from top to bottom trace. The inset shows a magnification of the emission spectrum of the thinnest wire (radius 80 nm) in the 2.30-2.40 eV spectral range. The arrows indicate the mode cutoff. **c)** Dispersion of the TE₀₁ mode of the nanowires with a radius of 110 nm (circles), 100 nm (squares), 90 nm (triangles) and 80 nm (asterisks). The solid lines are the numerical solutions for the eigenvalue equation of the TE₀₁ mode of a dielectric cylinder and the dashed line is the dispersion of light in vacuum. In the inset the measured size dependence of the TE₀₁ mode cutoff is shown for measurements performed on many more wires with the solid line the result of the calculations.

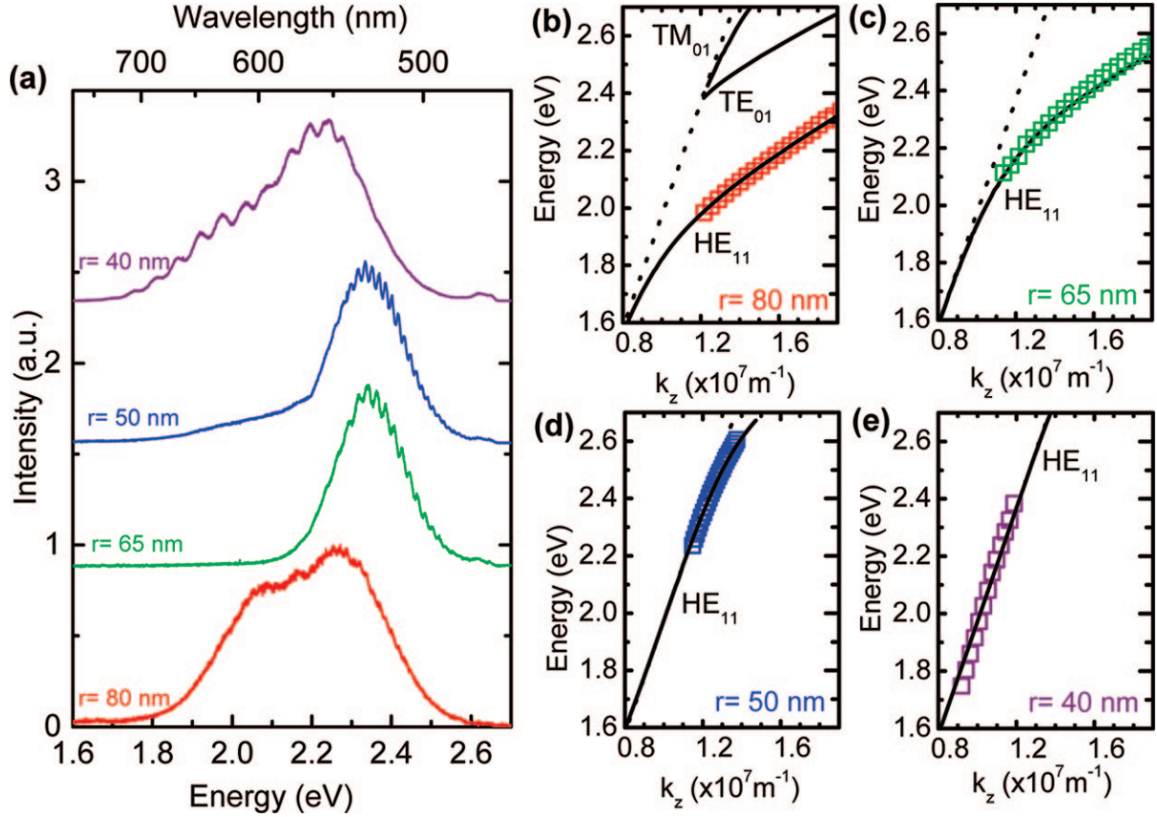


Figure 3.3: **a)** Emission spectra acquired from the ends of nanowires with radii of 75, 65, 50 and 40 nm and lengths of 8.52, 8.02, 33.15 and 14.01 μm respectively, with increasing diameters from top to bottom trace. **b-e)** Dispersion of the HE₁₁ mode of the nanowires with radii of 75 nm, 65 nm, 50 nm, and 40 nm, respectively. The solid lines are the results of the numerical solutions for the eigenvalue equation of the HE₁₁ mode of a dielectric cylinder and the dashed line is the dispersion of light in vacuum. In panels d) and e) the mode dispersion overlaps with the dispersion of light in vacuum.

We also studied relatively thicker nanowires, which can guide multiple modes simultaneously. The emission spectrum obtained from the end of a 150 nm radius nanowire shows intense Fabry-Pérot modulations (Figure 3.4a), which upon closer inspection (Figure 3.4a, inset) display an irregular peak spacing suggesting that at least two sets of modes participate in the standing wave formation. The energy-wavector dispersion of this nanowire (Figure 3.4b) together with the calculation results show that

the spectrum is dominated by the HE_{11} and TE_{01} modes, and not by TM_{01} mode, due to its poor reflectivity.¹² The calculated dispersion shows that in our observation range there is no low energy cut-off for these modes, which is corroborated by the observation of interference peaks down to the lowest observed emission energies. Interestingly, this thicker wire allows us to observe interference peaks up to close to the bandgap (2.69 eV at room temperature).²² It can be seen (Figure 3.4b and inset) that at energies approaching the bandgap of ZnSe, the experimental data deviates strongly from the calculated HE_{11} dispersion. This effect is more clearly seen in Figure 3.4c where the group index (group velocity normalized to the light speed) of these modes is plotted as a function of emission energy. It can be seen that at low energies (sub-bandgap) the group velocity is reduced by 35% for the two guided modes with respect to bulk ZnSe (Figure 3.4c, dotted line), solely due to the lateral confinement of the photon modes. However, more significant effects are observed close to the ZnSe band-edge (2.6 eV) where the group velocity reaches a value of $c/8$, which is clearly not predicted by the calculations. Due to the ZnSe exciton binding energy of 19 meV²² and the small observed exciton related luminescence peak we expect that close to the bandgap strong light-matter coupling between excitons and photons can occur,²³ resulting in a flattening of the dispersion and hence slowing of light (Figure 3.4b, c).¹⁶ This effect for macroscopic crystals is already included in the calculations by means of the dispersion of the refractive index which takes into account excitonic contributions.²² The strength of light-matter coupling in microcavity structures depends on the ratio of the oscillator strength to the optical mode volume.²⁴ In nanowires it is not unreasonable to assume that the mode volume is considerably reduced compared to larger crystals therefore giving rise to

enhanced light-matter interaction as a result of the higher electric field intensities inside the wire, which also agrees with earlier observations in ZnO nanowires.²⁵ More detailed experiments are being performed to quantify the strength of light-matter interaction in nanowire cavities.

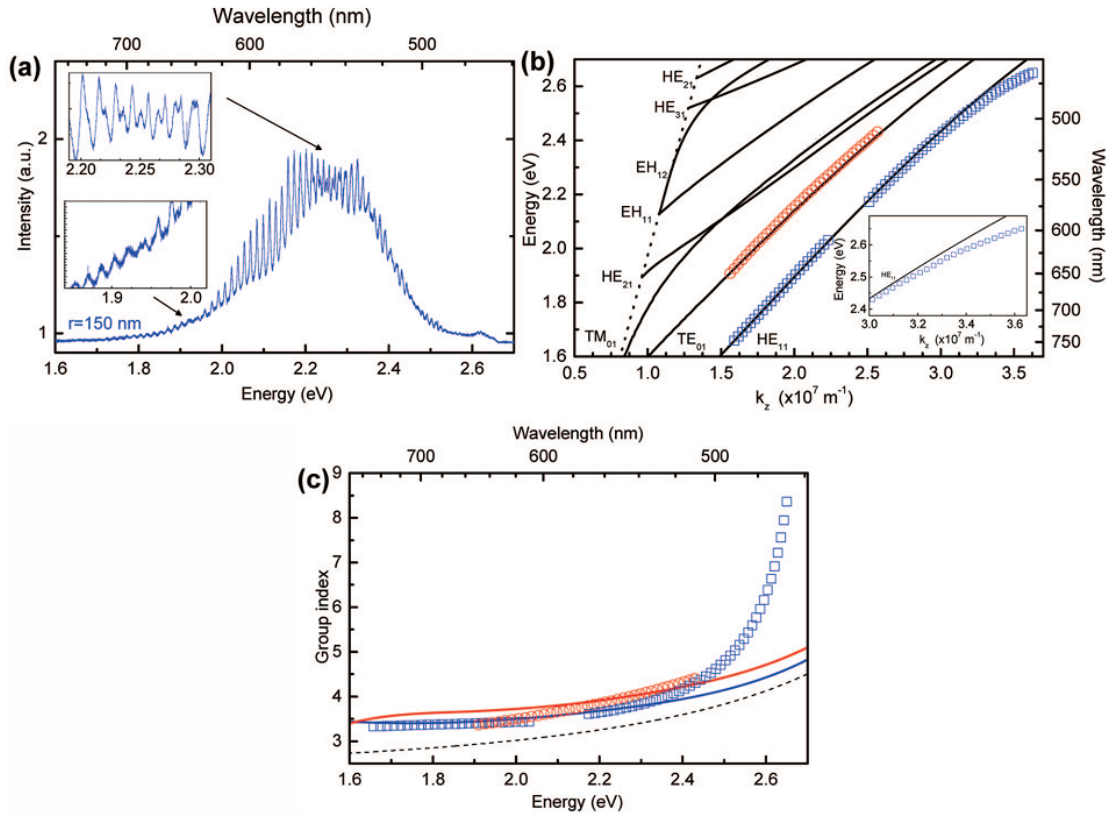


Figure 3.4: **a)** Emission spectrum acquired from the end of a nanowire with a radius of 150 nm. This spectrum shows three series of peaks which can be identified due to their spectral overlap giving rise to irregular periodicity (shown in the insets). **b)** Mode dispersion obtained from the spectrum shown in panel a). The solid lines are the results of the numerical solutions for the eigenvalue equation of the modes of a dielectric cylinder and the dashed line is the dispersion of light in vacuum. Inset: Energy-wavevector dispersion close to the bandgap region. Close to the band-edge of ZnSe (2.69 eV),²² a strong deviation of the experimental points from the calculations can be seen. **c)**

Group index obtained by differentiating the mode dispersions in panel b).

Experimentally measured group index of HE_{11} (blue squares) and TE_{01} (red circles) modes along with the numerical calculation results based on cylindrical waveguide modes (HE_{11} solid blue line; TE_{01} solid red line). The dashed line represents the group index in a bulk ZnSe crystal. Close to the band edge a pronounced slowing of the light can be seen for the HE_{11} mode.

In conclusion, we have demonstrated strong size dependent optical dispersion and group velocities in subwavelength ZnSe nanowire waveguide cavities using Fabry-Pérot resonator modes as probes. The measured dispersions show good correspondence with the calculations for an air-clad dielectric ZnSe cylinder where deviations from cylindrical morphology of the nanowire, substrate interaction and crystal anisotropy do not have significant effects. Furthermore, we observed subwavelength ($\lambda/9$) dispersionless guiding in the sub-bandgap range and significant slowing of the propagating light by 90% ($c/8$) due to enhanced light-matter interaction close to the exciton resonance. These results open the way to a rational design of semiconductor nanowire photonic devices in which the dispersion and signal speed can be tailored to specific functions, such as enhanced non-linear effects for optical switching and computing, and high-speed, near-dispersionless transmission of optical signals, and enhanced surface propagating waves for evanescent-wave sensor applications.

References

1. Law, M. et al. Nanoribbon Waveguides for Subwavelength Photonics Integration. *Science (Washington, D. C., 1883-)* **305**, 1269-1273 (2004).
2. Barrelet, C.J., Greytak, A.B. & Lieber, C.M. *Nano Lett.* **4**, 1981 (2004).
3. Johnson, J.C., Yan, H., Yang, P. & Saykally, R.J. Optical Cavity Effects in ZnO Nanowire Lasers and waveguides. *Journal of Physical Chemistry B* **107**, 8816-8828 (2003).
4. Duan, X., Huang, Y., Agarwal, R. & Lieber, C.M. Single-nanowire electrically driven lasers. *Nature (London)* **421**, 241-245 (2003).
5. Sirbuly, D.J., Tao, A., Law, M., Fan, R. & Yang, P. Multifunctional Nanowire Evanescent Wave Optical Sensors. *Advanced Materials (Weinheim, Federal Republic of Germany)* **19**, 61-66 (2007).
6. Tong, L., Lou, J. & Mazur, E. Single-mode guiding properties of subwavelength-diameter silica and silicon wire waveguides. *Optics Express* **12**, 1025 (2004).
7. Tong, L. et al. Subwavelength-diameter silica wires for low-loss optical wave guiding. *Nature (London)* **426**, 816-819 (2003).
8. Snyder, W. & Love, J.D. *Optical Waveguide Theory* (Chapman and Hall, London, 1983).
9. Cadien, K.C. et al. Challenges for On-Chip Optical Interconnects. *Proceedings of SPIE* **5730**, 133-143 (2005).
10. Krauss, T.F. Why do we need slow light? *Nature Photonics* **2**, 448 (2008).
11. Mortensen, N.A. & Xiao, S. Slow-light enhancement of Beer-Lambert-Bouguer absorption. *Applied Physics Letters* **30**, 141108 (2007).
12. Maslov, A.V. & Ning, C.Z. Reflection of guided modes in a semiconductor nanowire laser. *Applied Physics Letters* **83**, 1237-1239 (2003).
13. Seo, M.-K. et al. Modal Characteristics in a Single-Nanowire Cavity with a Triangular Cross Section. *Nanoletters* **8**, 4534-4538 (2008).
14. Freude, W., Hui-Hai, Y. & H. Zhi-Jian. Propagation Constant and Waveguide Dispersion of Single-Mode Fibers Measured from the Far-Field. *Journal of Lightwave Technology* **6**, 318-322 (1988).
15. Houdré, R. et al. Measurement of Cavity-Polariton Dispersion Curve from Angle-Resolved Photoluminescence Experiments. *Physical Review Letters* **73**, 2043 (1994).
16. Thévenaz, L. Slow and fast light in optical fibres. *Nature Photonics* **2**, 474 (2008).
17. Vugt, L.K.v., Rühle, S. & Vanmaekelbergh, D. Phase-correlated non-directional laser emission from ZnO nanowires. *Nanoletters* **6**, 2707-2711 (2006).
18. Voss, T. et al. High Order Waveguide Modes in ZnO Nanowires. *Nanoletters* **7**, 3675-3680 (2007).
19. Lukin, M.D. & Imamoglu, A. Optics and Quantum Entanglement of Ultraslow Single Photons. *Physical Review Letters* **84**, 1419 (2000).
20. Philipose, U. et al. Defect studies of ZnSe nanowires. *Nanotechnology* **19**, 215715 (2008).

21. Kiselev, V.A., Razbirin, B.S. & Uraltsev, I.N. Additional Waves and Fabry-Perot Interference of Photoexcitons (Polaritons) in Thin II-VI Crystals. *Physica Status Solidi B: Basic Research* **72**, 161-172 (1975).
22. Adachi, S. & Taguchi, T. Optical properties of ZnSe. *Physical Review B: Condensed Matter* **43**, 9569-9577 (1991).
23. Hopfield, J.J. Theory of the contribution of Excitons to the Complex Dielectric Constant of Crystals. *Physical Review* **112**, 1555-1567 (1958).
24. Reithmaier, J.P. et al. Strong coupling in a single quantum dot–semiconductor microcavity system. *Nature (London)* **432**, 197-200 (2004).
25. Vugt, L.K.v. et al. Exciton-Polaritons Confined in a ZnO Nanowire Cavity. *Physical Review Letters* **97**, 147401 (2006).

Chapter 4. **Propagation Loss Spectroscopy on Single Nanowire Active**

Waveguides

Reproduced in part with permission from Nano Letters, Volume 10, Issue 6, Pages 2251-2256. Copyright 2010 American Chemical Society.

Despite the recently increased activity in the field of active optical waveguides,^{1,2} not much attention has been focused on the understanding of the light-matter interaction and photonic propagation properties in nanoscale optical waveguides, which can lead to observation of novel phenomena originating from tight confinement in comparison to bulk materials and can assist in optimal nanophotonic device design. However, it is not trivial to characterize the propagation properties of nanoscale waveguides since their diminutive dimensions make direct loss measurements troublesome due to in- and out-coupling losses³ as well as strong absorption close to the electronic band-edge of the material. These challenges require development of new measurement techniques to characterize nanoscale optical cavities. Waveguide losses in nanowires have been characterized previously,^{4, 5} however only limited or no spectral information was obtained, missing propagation loss dispersion information. Propagation loss dispersion is especially important in direct bandgap semiconductors where propagation close to the band-edge occurs by mixed photonic-electronic excitations (polaritons) that form due to strong light-matter interaction of excitons with photons,⁶ thereby making the propagation particularly sensitive to the electronic structure of the wire.⁷

CdS nanowires have previously been studied by micro-photoluminescence measurements to determine their electronic resonances,⁸ waveguiding,⁴ and lasing properties.⁹ However, this method is limited in that wavelengths near electronic

resonances are reabsorbed too strongly for detection in the photoluminescence measurements. Additionally, such direct photoluminescence measurements cannot provide information on propagation length (or loss) and its dispersion, crucial for design of devices utilizing semiconductor nanowire waveguide elements. Absorption-based measurements are required for these situations where emission spectroscopy does not provide useful information near electronic resonances.

In this chapter, we report on spatially and spectrally resolved laser excitation scanning measurements on CdS nanowires at room temperature and at 77.6 K, from which the waveguide propagation losses and dispersion could be determined. By utilizing a measurement method involving scanning a laser spot over the body of the nanowire whilst detecting the spectrally resolved waveguided photoluminescence emerging at one of the nanowire end facets, propagation loss spectra in the strongly absorbing near-bandedge region could be found as well as signatures of the CdS A and B excitons via observation of both resonance peaks and their interaction with waveguided light. These signatures serve to highlight the importance of polaritonic interactions in active nanowire waveguide systems as well as inform the design of future active nanowire waveguide devices.

4.1. Experimental Procedures

CdS nanowires (Figure 4.1) were obtained by the vapor-liquid-solid method¹⁰ in a quartz tube furnace using evaporation of 99.995% pure CdS powder (Aldrich). 130 mg of CdS powder was placed in a quartz boat in the middle of the tube, and Si substrates covered by a 5 nm thick Au/Pd layer using plasma sputter deposition were placed 13.7

cm downstream (referenced to the middle of the tube). The tube was evacuated to 20 mTorr and argon carrier gas was introduced at a flow of 100 SCCM to reach a stable pressure of 294 Torr. The tube was rapidly heated to 760 °C and kept there for 180 minutes after which the furnace was cooled by a forced airflow. After synthesis, the nanowires were transferred to 0.5 mm-thick Si substrates covered with a 300 nm thermal oxide by dry transfer, and the substrates were mounted on the temperature-controlled liquid nitrogen microscope cryostat using silver paint. The measurement substrates were marked so that individual wires could be characterized by optical and electron microscopy techniques. Optical experiments were carried out using the photoluminescence setup shown in Figure 2.2. The 457.9 nm laser line of a continuous wave argon ion laser was expanded onto the back aperture of the objective resulting in a Gaussian spot with a width of 800 nm, giving an average excitation power density of $6 \times 10^4 \text{ W/cm}^2$. Waveguided photoluminescence from the individual wires was collected by the same objective and projected onto either a small CCD for color imaging or the focal plane of an optical fiber fitted with a focusing lens. The light collected by the fiber was coupled to the Acton spectrometer and detected by the cooled 2048 horizontal pixel Princeton Instruments CCD, resulting in a full width at half-maximum (FWHM) wavelength resolution of 0.1 nm. After the optical measurements, the lengths and widths of the nanowires were determined by scanning electron microscopy (FEI Strata DB235 FIB).

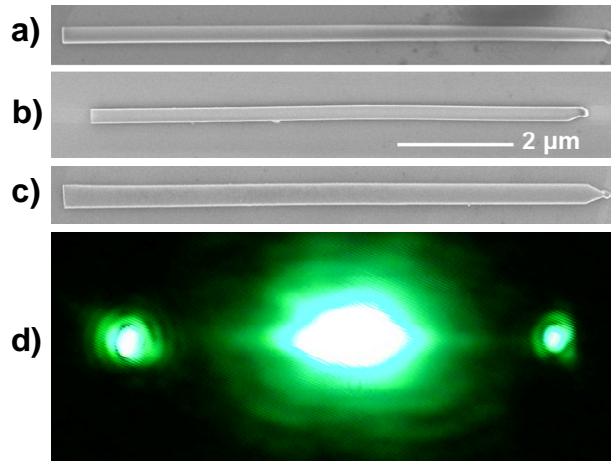


Figure 4.1: a)-c) Scanning electron microscopy images of three CdS nanowires dispersed onto a 300 nm thick SiO₂-covered Si wafer on which optical measurements were performed. These nanowires have lengths of 9.74, 8.96, and 9.58 μm, and diameters of 245, 260, and 400 nm respectively. d) Real color optical image of a CdS nanowire under focused 458 nm Ar⁺ laser illumination. The laser is focused on the center of the nanowire, producing photoluminescence from the nanowire body. Much of this emission is guided along the nanowire and diffracted at its end facets, as shown.

A photoluminescence image of a nanowire under localized excitation (Figure 4.1d) shows, in addition to emission from the nanowire body where the laser is focused, pronounced emission from the end facets due to waveguiding. For the primary experimental geometry, the excitation spot was scanned over a 40 x 100 pixel (8 × 20 μm) rectangle containing the nanowire of interest while the collection area was left positioned over the nanowire end facet. In this configuration, the excitation spot can be thought of as a moving light source in a type of modified absorption spectroscopy (Figure 4.2a), whereby the local photoluminescence of CdS generated by the incoming laser acts as the source and the bandwidth of this source (a single exciton-related peak from 2.30 to 2.45 eV at room temperature (300 K)) defines the effective range of the spectrographic method. Light which is guided between the source and collection area is recorded by the

spectrometer as one element of a 40×100 spectra matrix, the laser then moves to a neighboring spot and the process repeats. After the resulting 40×100 spectra are mapped out spatially, individual emission wavelengths as recorded by the spectrometer can be isolated in each pixel, producing a two-dimensional map of how much light at any particular energy was waveguided to the nanowire end facet (Figure 4.2b). A line profile was taken along the nanowire length and intensity versus distance data were extracted for each emission wavelength (Figure 4.2c). The first $1 \mu\text{m}$ from the detection point was removed to avoid convolution of source (laser spot) emission with waveguided emission. We assume linear optical losses which are constant along the length of the nanowire, leading us to fit line profiles to an exponential decay function, $Ae^{-\alpha(z-z_0)}$, where A is the amplitude and z_0 is fixed at the end facet. The decay constant from this function, α , we term the propagation loss coefficient of the nanowire at that wavelength since it includes any losses such as waveguide leaking and scattering losses as well as material absorption. The energy dependence of α then gives the propagation loss spectrum, which contains detailed information about the nanowire active waveguides.

The corresponding propagation loss spectrum for the same nanowire (Figure 4.1a) examined in Figure 4.2, obtained at room temperature, is plotted (black squares) alongside its waveguided photoluminescence spectrum (green line) for the emission range close to the room temperature bandedge of CdS $\sim 2.45 \text{ eV}$ ¹¹ in Figure 4.3. The waveguided photoluminescence spectrum is modulated by a series of periodic peaks attributed to Fabry-Pérot resonances, which occur in wavevector space at equally-spaced intervals of $|\mathbf{k}_z| = n\pi/L_z$ where \mathbf{k}_z is the real wavevector along the length of the nanowire waveguide, n is a positive integer, and L_z is the nanowire length. While these peaks are

useful insofar as they can be used to determine the waveguide dispersion of a given nanowire,¹² Fabry-Pérot etalons containing absorbing material have been shown to act as long-path absorption cells^{13, 14} which can report absorption higher than that of the same spacer not placed within the cavity due to light undergoing multiple passes.¹⁵

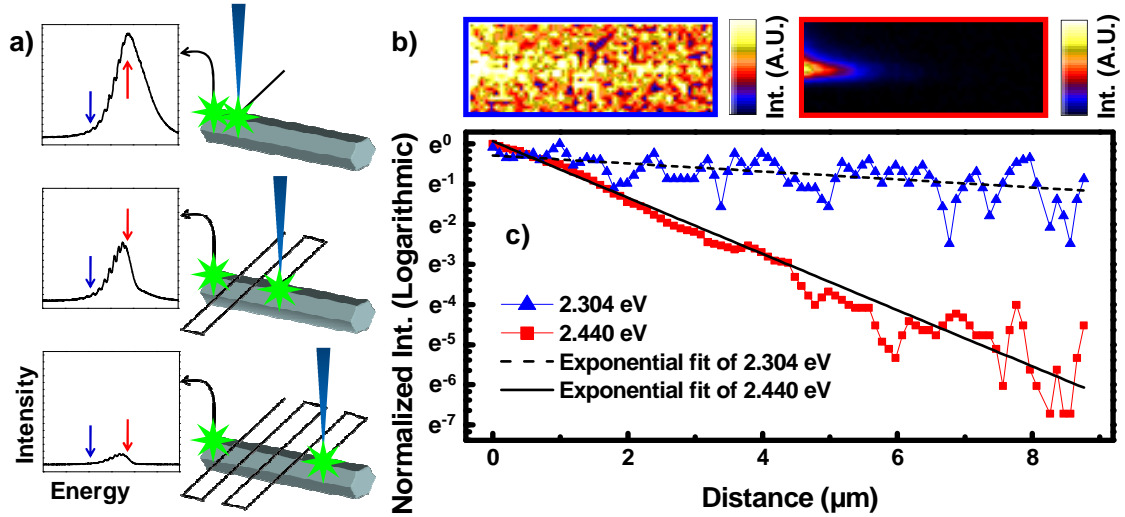


Figure 4.2: **a)** Illustration of CdS nanowire from Figure 4.1a) under focused 458nm Ar+ laser excitation at 300 K. A position-sensitive photodetector collects photoluminescence spectra from the end facet as the laser is scanned along the wire, generating a local light source as it travels. **b)** Spatially resolved excitation images of the wire shown in Figure 4.1a) obtained at energies 2.304 and 2.440 eV (highlighted in blue and red), respectively. Each pixel shows, for that specific energy, the relative intensity of light detected by the position-sensitive photodetector stationed over the leftmost end facet due to the laser being focused at that point. **c)** Normalized intensity vs. distance of the excitation laser from the end facet line profiles extracted from the spatially resolved images in b).

Propagation loss coefficients were obtained by fitting each line trace to the form $Ae^{-\alpha(z-z_0)}$, where α is the propagation loss coefficient, A is the amplitude, and z_0 is fixed at the nanowire end facet.

The exact ratio of measured to actual absorption is dependent on quantities difficult to ascertain for multimode, waveguiding nanowires such as end facet morphology and reflectivity and can therefore complicate the issue of drawing parallels

directly between experimentally obtained propagation loss coefficients and literature magnitudes for bulk CdS absorption. This is not without advantage, however, as it serves to highlight the ability of this technique to experimentally discern true propagation length (obtained by inverting the propagation loss coefficients) and its frequency dependence in individual nanowires where subtleties unique to each structure hinder the effectiveness of theoretical prediction.

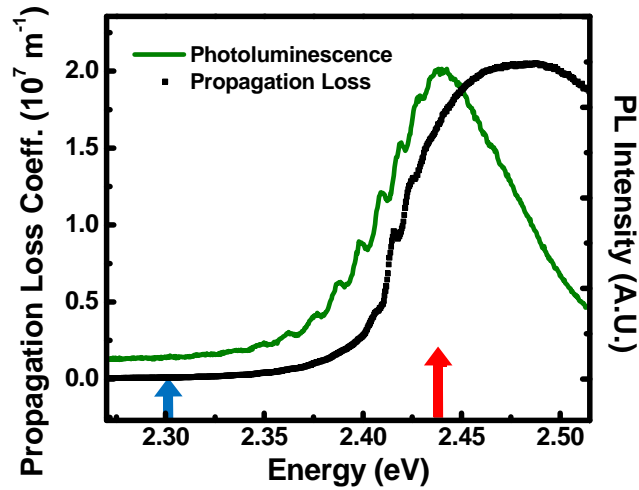


Figure 4.3: Propagation loss spectrum (black) for the wire shown in Figure 4.1a) at 300 K, plotted alongside photoluminescence (green) from the end facets, while the energies highlighted in Figure 4.2 are denoted blue and red. The closely-spaced peaks are longitudinal Fabry-Pérot resonances. Note that the propagation loss spectroscopy method provides enhanced range over the conventional photoluminescence due to its ability to track minute changes in emission as a function of distance even when the intensity of individual waveguided photoluminescence measurements is low.

4.2. Discussion

The propagation loss spectroscopy method lends itself well to judging the overall waveguiding ability of individual wires. The propagation loss spectrum in Figure 4.2 shows that this particular nanowire waveguides efficiently (propagation loss coefficient $\sim 15,000 \text{ m}^{-1}$) below 2.35 eV, while a sharp decrease in propagation length occurs as the

energy approaches the CdS room temperature bandedge. These observations are reinforced by the waveguided photoluminescence peaking significantly below the bandedge, again showing that waveguiding is favored at off resonance energies.¹⁶ Upon further comparing the two spectra, it is also immediately clear that the propagation loss spectrum provides sufficient intensity even at energies close to the band-edge where the photoluminescence output is relatively low. This extended range is possible because there is still enough intensity to track trends between spectra from neighboring pixels along the nanowire length in the propagation experiments even if the individual waveguided photoluminescence spectra do not show clear features themselves.

While room temperature measurements are effective in demonstrating the expanded range and feature-detection capability of the propagation loss spectroscopy technique over individual photoluminescence spectra, the finite intensity of each spectrum remains a limiting factor in the quality of the final propagation loss spectrum: changes between spectra cannot be detected when intensity is very low. Furthermore, laser damage limits the maximum excitation power, and microscopic sample drift limits total collection time. Therefore, to obtain the fine electronic structure of CdS in the region of electronic resonances by reducing temperature broadening as well as enhance our ability to detect it by increasing emission for a given excitation power and collection time, we cooled the sample to 77.6 K. The waveguided photoluminescence (green line) from an 8.96 μm long, 260 nm diameter CdS nanowire at 77.6 K is presented alongside its propagation loss spectrum (black squares) in Figure 4.4. Modulation peaks again attributed to Fabry-Pérot resonances are apparent in the photoluminescence spectrum, and aside from an overall blue shift, it appears qualitatively similar to that in the room

temperature measurement in Figure 4.3. Here as well there are no discernable features at energies higher than the global peak at 2.533 eV, but it is in this range that the advantages of low temperature measurement become apparent in the propagation loss measurements.

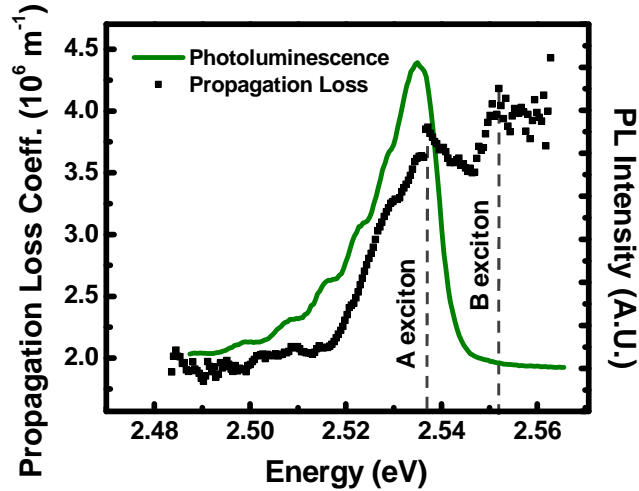


Figure 4.4: Propagation loss spectrum (black) for the nanowire shown in Figure 4.1b) at a cryostat-reported temperature of 77.6 K, obtained by plotting α as a function of energy.

A peak corresponding to the free A exciton was found at 2.537 eV, while a peak corresponding to the free B exciton was found at and 2.553 eV (dashed lines), implying a sample temperature of 105 K (see text). A waveguided photoluminescence spectrum from the same wire, exhibiting longitudinal Fabry-Pérot resonances, is shown in green.

Significant range enhancement of the propagation loss spectroscopy method is again demonstrated, as it produces useful information until ~ 2.560 eV compared with ~ 2.540 eV for waveguided photoluminescence. The two most prominent features in the propagation loss spectrum are the transition from relatively constant propagation loss constants at lower energies to a steadily-increasing propagation loss which occurs around 2.517 eV and the observation of two higher-energy peaks at 2.537 and 2.553 eV which do not appear in any individual photoluminescence measurements, pointing towards resonances which absorb more strongly than they emit. Hopfield and Thomas¹⁷ studied

reflection spectra from CdS crystals at 77 K, and reported free A and B exciton resonances at 2.544 and 2.559 eV, differing from our values by 7 meV, respectively. Considering that both of our values have the same offset to that reported by Hopfield and Thomas (and therefore, the spacing between the two is also approximately equal), we believe our high-energy peaks are a direct measurement of the free A and B exciton resonances. The 7 meV average discrepancy is likely attributed to nanowire temperature: though the substrate is held under vacuum, the nanowires sitting on its surface are not attached and it is likely that they are at a higher temperature than the cryostat-reported 77.6 K. From temperature-dependent exciton resonance data,¹⁸ we determine our resonances translate to an actual nanowire temperature of 105 K. This discrepancy is reasonable considering the nanowires are separated from the thermocouple by a thick Si/SiO₂ substrate and experience local heating due to the laser excitation of the sample.

At the A and B exciton resonances, the propagation loss coefficient peaks at $3.90 \times 10^6 \text{ m}^{-1}$ and $4.15 \times 10^6 \text{ m}^{-1}$, and in the region of constant propagation loss from 2.49-2.52 eV (still close to the electronic resonances) it averages $1.70 \times 10^6 \text{ m}^{-1}$. Shalimova and Khirin¹⁹ reported an absorption spectrum for polycrystalline CdS held at 77 K which qualitatively matches the shape of ours, though it differs in that their exciton absorption coefficients are within an order of magnitude but their lower-energy coefficients are multiple orders of magnitude smaller. Though our method appears qualitatively similar to absorption spectroscopy, our coefficients provide information on both absorption and waveguide losses, which are much more sensitive to the morphology, diameter, and surface conditions of each individual nanowire. While it would be difficult to infer conclusions from the small differences between coefficients at higher energies obtained

for nanowires in comparison to bulk CdS, the fact that our coefficients at lower energies are orders of magnitude higher suggests that, in addition to small waveguide losses, electronic losses greater than those seen in bulk CdS may also play a role in this energy range. Exciton-photon interaction has been shown to dominate over exciton-phonon interaction in CdS thin-films crystals (300-800 nm thick) near our experimental temperature,²⁰ which alters the dispersion of the material in the exciton resonance region. We believe that enhanced exciton-photon interaction in this nanowire, in comparison with bulk CdS, has increased the energy range over which excitonic absorption can take place, extending into what is the conventional “photonic” region in bulk. Other nanowires of similar diameters measured at this temperature also show a similarly marked increase in propagation loss coefficient at lower energies than the electronic resonances, suggesting an increase in light-matter interaction regardless of individual length or morphology and dependent only upon the confining dimension of the diameter (Figure 4.5 and Table 4.1).

A full model of the material dispersion relations in individual nanowires is necessary to understand important optical transport properties at the nanoscale where strong light-matter coupling becomes important,¹² but precise placement of resonance levels is required before any other parameters such as exciton transition strength and damping²¹ can be adjusted and modeled for a given system. Fortunately, the experimentally determined levels of the A and B exciton resonances from Figure 4.4 can be used to this end for all nanowires held at this temperature in our experimental setup, since the nanowire waveguides are much larger than the exciton Bohr radius in bulk CdS (~ 5 nm)²² and quantum confinement effects can be neglected. While the waveguide

modes of a bulk dielectric cylinder are well described by solving Maxwell's equations with appropriate boundary conditions²³ and using a Sellmeier type equation²⁴ to include bulk material dispersion, this fails to take into account changes in dispersion originating from strong light-matter interaction which can manifest in nanoscale cavities. To take this interaction into account, we recently developed a polaritonic waveguide model²⁵ with interacting excitons (A and B for CdS) which explicitly includes dispersive effects via the exciton-polariton model rather than the phenomenological Sellmeier model, and its strong dependence on exciton resonance levels is exploited here to confirm our values.

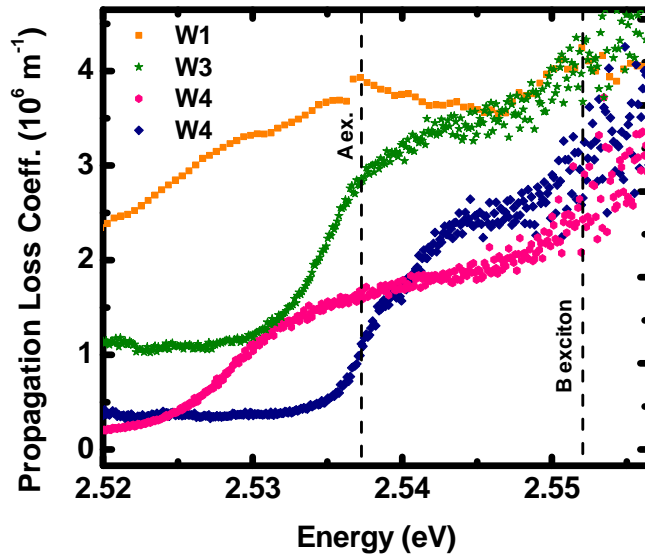


Figure 4.5: Propagation loss spectra of Wires 1-5 at 77.6 K, ordered according to propagation loss coefficient at 2.525 eV. Vertical lines are placed at the A- and B-free exciton resonances as determined for the nanowire discussed in Figure 4.4.

Wire	1	2	3	4
Diameter (nm)	260	425	185	220
Length (μm)	8.96	17.65	8.30	9.15
Prop. loss coeff. at 2.525 eV (10^6 m^{-1})	2.79	1.05	0.42	0.34

Table 4.1: Diameter, length, and propagation loss coefficients at 2.525 eV.

Figure 4.6 shows the results of numerical solutions for the eigenvalue equation of the fundamental mode of a dielectric cylinder, calculated using the above mentioned polaritonic waveguide model, plotted (right) alongside the waveguided photoluminescence (left) of a 9.58 μm long nanowire with a radius of 200 nm (Figure 4.1c) at a cryostat-reported temperature of 77.6 K. The square data points superimposed on the calculated lines form the experimental dispersion relation of the nanowire, obtained from the Fabry-Pérot peaks in the photoluminescence by plotting their energies at equally-spaced intervals of the real wavevector k_z .¹² The calculations were performed using Hopfield and Thomas' literature value for the B exciton resonance at 77 K (2.559 eV) as well as the experimentally obtained value obtained from Figure 4.4 (2.553 eV). From this graph it is clear that not only is the A exciton is inactive for this mode (possible when polarization is parallel to the crystallographic c-axis of wurtzite CdS),¹⁷ but more importantly the experimentally determined B exciton resonance produces a dispersion curve which fits, while the 77 K dispersion does not, reaffirming a clear increase in nanowire temperature to 105 K over the cryostat-reported value of 77.6 K. This fitting not only adds credence to our interpretation of the two peaks in Figure 4.4 as A and B

exciton resonances, but also demonstrates the utility of propagation loss spectroscopy as an potential aid in the engineering of single nanowire devices which would implicitly or explicitly depend on electronic resonance levels and encourages further experimental refinement of the polaritonic model with the resonance level variables now set in place as constants.

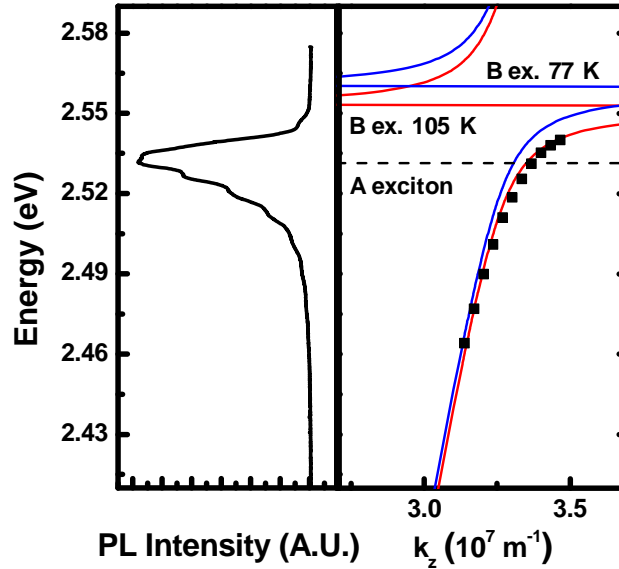


Figure 4.6: Photoluminescence (left) and dispersion (right) for the nanowire shown in Figure 4.1c) at a cryostat-reported temperature of 77.6 K. The solid lines are the results of numerical solutions for the eigenvalue equation of the fundamental mode of a dielectric cylinder, calculated using a polaritonic model,²⁵ the dashed line indicates the experimentally obtained A exciton resonance, and the square data points are determined from the longitudinal Fabry-Pérot resonances in the photoluminescence spectrum. The calculations were performed using literature values for the B exciton resonance at 77 K (blue) as well as the experimentally-obtained resonance value (corresponding to a temperature of 105 K) from Figure 4.4 (red).

In conclusion, we have demonstrated a method for obtaining the propagation loss spectra of single active nanowire waveguides, significantly enhancing the usable range of conventional photoluminescence and improving upon previous methods for optical analysis of individual nanowire structures by simultaneously utilizing fine spatial and

spectral resolution. In addition to producing spectra detailing wavelength-dependent propagation lengths in individual CdS nanowires, signatures of exciton-polariton propagation were detected clearly and precise positioning of the CdS A and B free exciton resonances was achieved. These resonances were utilized to determine the actual nanowire temperature and aid in the modeling of dispersion relations, which is key to obtaining a deeper understanding of active nanowire waveguides. Such fundamental understanding could facilitate the engineering of active nanophotonic circuit components such as switches, sensors, and waveguides operating in the photonic and polaritonic regions, where knowledge of total propagation length and dispersion is critical to overall device design.

References

1. Morales, A.M. & Lieber, C.M. A Laser Ablation Method for the Synthesis of Crystalline Semiconductor Nanowires. *Science (Washington, D. C., 1883-)* **279**, 208-211 (1998).
2. Hiruma, K. et al. MOCVD. *Journal of applied Physics* **77**, 447 (1995).
3. Voss, T. et al. High Order Waveguide Modes in ZnO Nanowires. *Nano Lett.* **7**, 3675-3680 (2007).
4. Barrelet, C.J., Greytak, A.B. & Lieber, C.M. Nanowire Photonic Circuit Elements. *Nano Lett.* **4**, 1981 (2004).
5. Yan, R., Pausauskie, P., Huang, J. & Yang, P. Direct photonic-plasmonic coupling and routing in single nanowires. *PNAS* **106**, 21045 (2009).
6. Hopfield, J.J. Theory of the contribution of Excitons to the Complex Dielectric Constant of Crystals. *Physical Review* **112**, 1555-1567 (1958).
7. Vugt, L.K.v. et al. Exciton-Polaritons Confined in a ZnO Nanowire Cavity. *Physical Review Letters* **97**, 147401 (2006).
8. Hoang, T.B. et al. Temperature dependent photoluminescence of single CdS nanowires. *Applied Physics Letters* **89**, 123123 (2006).
9. Agarwal, R., Barrelet, C.J. & Lieber, C.M. Lasing in Single Cadmium Sulfide Nanowire Optical Cavities. *Nano Lett.* **5**, 917-920 (2005).
10. Chung, H.S. et al. A generic approach for catalyst-supported vertically-aligned nanowire growth. *Nano Lett.* **8**, 1328 (2008).
11. Kittel, C. Introduction to Solid-State Physics (Wiley, 1995).
12. van Vugt, L.K., Zhang, B., Piccione, B., Spector, A.A. & Agarwal, R. Size-Dependent Waveguide Dispersion in Nanowire Optical Cavities: Slowed Light and Dispersionless Guiding. *Nano Lett.* **9**, 1684-1688 (2009).
13. Kastler, A. Atomes a l'interieur d'un Interferometre Perot-Fabry. *Applied Optics* **1**, 17 (1962).
14. Jackson, D.A. The Spherical Fabry-Perot Interferometer as an Instrument of High Resolving Power for use with External or with Internal Atomic Beams. *Proc. R. Soc. London Ser. A* **263**, 289 (1961).
15. Hernandez, G. Fabry-Perot with an absorbing etalon cavity. *Applied Optics* **24**, 3062 (1985).
16. Ruhle, S. et al. Nature of Sub-Band Gap Luminescent Eigenmodes in a ZnO Nanowire. *Nano Lett.* **8**, 119-123 (2007).
17. Thomas, D.G. & Hopfield, J.J. Exciton Spectrum of Cadmium Sulfide. *Physical Review* **116**, 573 (1959).
18. Anedda, A. & Fortin, E. Temperature Shift of Excitons in CdS. *Phys. Stat. Sol.* **36**, 385 (1976).
19. Shalimova, K.V. & Khirin, V.N. Mechanism for the optical absorption of Cadmium Sulfide. *Soviet Physics Journal* **12**, 487-491 (1969).
20. Voigt, J. Influence of Spatial Dispersion on the Transmission Spectra of CdS Single Crystals. *Physica Status Solidi (B)* **64**, 549 (1974).

21. Klingshirn, C.F. *Semiconductor Optics* (Springer-Verlag, Berlin, 2007).
22. Wang, Y. & Herron, N. Nanometer-Sized Semiconductor Clusters: Materials Synthesis, Quantum Size Effects, and Photophysical Properties. *J. Phys. Chem.* **95**, 525 (1991).
23. Snyder, W. & Love, J.D. *Optical Waveguide Theory* (Chapman and Hall, London, 1983).
24. Ninomiya, S. & Adachi, S. Optical properties of wurtzite CdS. *Journal of Applied Physics* **78**, 1995 (1995).
25. van Vugt, L.K., Piccione, B. & Agarwal, R. Incorporating polaritonic effects in semiconductor nanowire waveguide dispersion. *Applied Physics Letters* **97**, 061115 (2010).

Chapter 5. Variable Temperature Spectroscopy of As-Grown and Passivated

CdS Nanowire Waveguide Cavities

Reproduced in part with permission from The Journal of Physical Chemistry A, Volume 115, Issue 16, Pages 3827-3833. Copyright 2011 American Chemical Society.

Crystalline nanowires synthesized from wide bandgap semiconductor CdS are of interest due to their demonstrated ability to be assembled as active waveguides,^{1, 2} modulators,² optical cavities,³ and lasers,^{4, 5} and also because they form an intermediate class of crystals which exhibit optical confinement, in between electronically confined quantum dots⁶⁻⁸ and their bulk counterparts that show no optical and electronic confinement. With their diameters ranging from ~50-300 nm and lengths of up to several tens of micrometers, high crystalline nature and well defined crystal orientation, these crystals form a natural link between the classic bulk platelet literature⁹⁻¹¹ and present day nanophotonic applications such as wave guiding and lasing. CdS is particularly known for the strong coupling of its bound electron hole pairs (free excitons) to the light field due to the high oscillator transition strength and exciton stability up to room temperature¹². This results in the formation of exciton-polaritons which are a linear superposition of excitons and photons, resulting in reversible emission and absorption and the formation of anti-crossing lower and upper polariton branches in the energy-wavevector dispersion discussed in Section 1.2. The polaritonic behavior is typically characterized by (time resolved) photoluminescence, transmission and reflection measurements.^{13, 14} These polaritonic effects hold promise for exciting physical phenomena such as slow light,¹⁵ low threshold polariton lasing¹⁶ and Bose-Einstein condensation^{17, 18} and are therefore worthwhile to pursue in the nanowire geometry.

Before such advanced topics can be addressed in CdS nanowires, it is vital to have knowledge of the intrinsic electronic and optical resonances in the nanowires.^{1,3} Due to optical cavity formation and the strong coupling of the optical field with the electronic resonances, polaritonic effects are particularly important in CdS nanowires. The dependence of the polaritonic properties on sample geometry can obfuscate determination of the purely electronic resonances; therefore careful spatially resolved temperature dependent analysis of the electronic, optical and polaritonic resonances is necessary. Additionally, due to the large surface to volume ratio of these nanostructures the optical quality is largely determined by the surface even though the nanowires themselves are single crystalline with a low concentration of intrinsic defects. Traps formed by dangling bonds and adsorbed species at the surface can bind and ionize excitons, causing changes in exciton transition strength, energy and lifetime, all influencing the light-matter coupling strength. These effects can be negated by electronically passivating the surface by binding with a suitable (in)organic ligand thereby removing surface traps which create intra bandgap states and restoring superior optical quality.¹⁹ Temperature dependent optical characterization of the electronic resonance levels in unpassivated CdS nanowires has been reported before^{5, 20} however either the nanowire quality was not high enough to form optical cavities with low intrinsic defect concentrations or determination of the resonance levels was outside the scope of the study.

Here we show the spatially resolved photoluminescence characterization of CdS nanowire crystals at temperatures ranging from 77 K to 298 K. Due to the spatially resolved detection, a distinction can be made between purely electronic and polaritonic

resonances and their temperature dependence can be determined. To improve the optical quality of the nanowires a SiO₂ passivation layer is applied resulting in the observation of free excitons in contrast to the observation of defect bound excitons in unpassivated wires.

These results will facilitate the precise determination of light-matter coupling strength in CdS nanowires as well as its manipulation through temperature tuning of the electronic resonances and the optical cavity resonances, important for the utilization of polaritonic effects such as macroscopic coherence, nonlinearities and slow light for devices such as lasers, switches and sensors at the nanoscale.

5.1. Experimental methods

CdS nanowire crystals were obtained under the same conditions described in Section 4.1. The growth substrates were subsequently characterized by SEM and photoluminescence measurements in order to screen the samples for morphology and spectral quality. Photoluminescence was performed using the same setup as described in Section 4.1. CdS nanowire passivation with SiO₂ was carried out using Atomic Layer Deposition (ALD, Cambridge Nanotech) using alternating O₃, 3-aminopropyltriethoxysilane and H₂O pulses which deposited a conformal coating of ~5 nm on the nanowires. Fourier transform infrared spectroscopy (FTIR, Thermo Scientific) measurements were done on the uncoated and coated wires to check the coating process.

5.2. Results and discussion

Figure 5.1a shows the growth substrate imaged by SEM immediately after three hours of nanowire growth at 760 °C. The synthesis yielded wires of 100-300 nm diameters with an average length of 15 μm . Wires grown using sputter deposition of gold exhibit some variation in diameter and length, but optimization of growth parameters and careful monitoring of conditions resulted in wires with single-crystalline wurtzite structure. Figure 5.1b and the inset in Figure 5.1a show SEM images of an isolated 9.98 μm -long wire of diameter 130 nm after dry transfer to the silicon oxide covered optical measurement substrate. The diameter is uniform from base to tip with no visible morphology defects present along the wire length. The zoomed in SEM image of the tip in the inset of Figure 5.1a shows a clearly faceted particle, indicative of nanowire growth via the VLS mechanism with a gold nanoparticle acting as the catalyst.²¹⁻²⁶ Figure 5.1c shows the X-ray diffraction (XRD) pattern of a typical Si substrate after nanowire growth as shown in Figure 5.1a. The peaks in the diffractogram correspond exclusively to wurtzite CdS or the aluminum sample holder, and no evidence of CdS polymorphism (i.e. zinc blende CdS) was found.

Temperature-dependent optical measurements were performed in the experimental geometry as is shown in Figure 5.2a with the shown substrate glued to the cold finger of a continuous flow liquid nitrogen cryostat using silver paint. An individual nanowire lying on the SiO₂-coated Si substrate is excited from the far field by focusing an 800 nm diameter Ar-ion laser beam on the wire center, resulting in local photoluminescence. This local photoluminescence (termed body emission in the

remainder of this article) is generated in the wire core and can subsequently be guided to the wire ends due to optical confinement resulting from the high refractive index contrast between the CdS wire and its air cladding. At the wire ends this guided light can partly leak out and is scattered into the excitation direction due to diffraction from subwavelength apertures (ends), resulting in the observation of localized emission at the wire ends. Figure 5.2b and Figure 5.2c show real color optical micrographs of such a nanowire; Figure 5.2b shows the wire illuminated under white light, whereas Figure 5.2c shows the same wire excited in the manner illustrated in Figure 5.2a. Both the body (region where the nanowire is directly excited) and the end emission (waveguided emission from the ends) spots display the characteristic green CdS emission color.

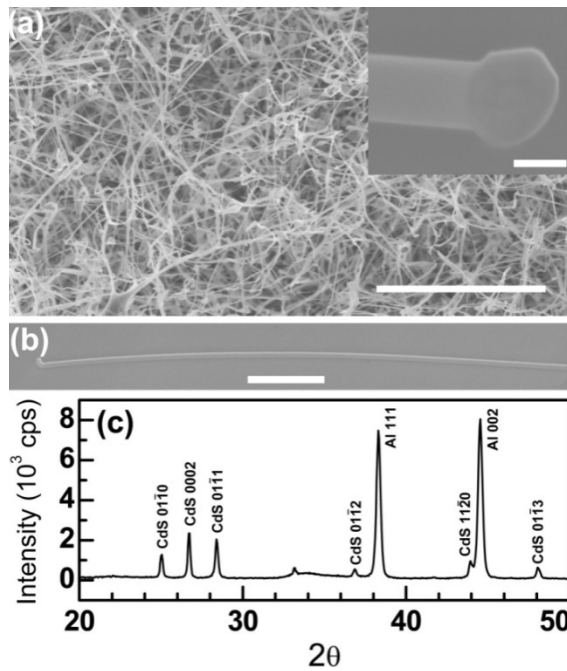


Figure 5.1: **a)** SEM image of the nanowire growth substrate. Scale bar, 1 μm. Inset: Detail of a catalyst particle on the tip of the nanowire shown in panel b). Scale bar, 100 nm. **b)** SEM image of an individual nanowire of width 130 nm and length 9.98 μm on the optical measurement substrate. Scale bar, 1 μm. **c)** X-ray diffractogram of the CdS nanowire covered substrate shown in panel a).

Room temperature (298 K) emission spectra from the body and the ends obtained in this manner for the wire shown in Figure 5.1b and c are displayed in Figure 5.3a (blue and black lines, respectively). It is immediately apparent that there is a large red shift of (39 meV) between the maxima of the body emission (2.4568 eV) and that of the end emission (2.4176 eV). The body emission is significantly broadened (FWHM 58.4 meV) and although emission takes place at energies that coincide with exciton levels obtained from established literature²⁷ (indicated by the two vertical arrows), the spectra do not show any features that can be assigned to discrete exciton lines. The end emission is periodically modulated with the period becoming shorter towards higher energies (in the vicinity of excitonic resonances). This intensity modulation is due to standing wave formation along the length of the nanowire, demonstrating that the nanowire acts as a longitudinal (z -direction) Fabry-Pérot cavity.²⁸⁻³⁰ In principle, the Fabry-Pérot interference peaks can be used to determine the effective length of the resonator, which may be different from the actual nanowire length. Although the observed end emission does originate from the actual ends of the nanowires, the ~ 500 nm optical resolution limit of our system gives rise to some uncertainty in determining the actual resonator length. In addition, due to the formation of exciton-polaritons in this energy region, a complete fitting of the experimental points to a full polaritonic model³ taking into account size dependent light-matter interactions is needed, which is outside the scope of this article.

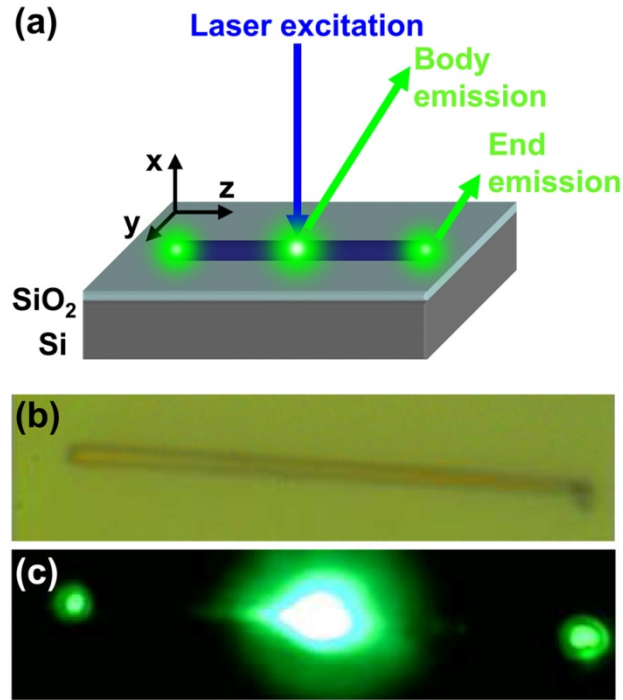


Figure 5.2: **a)** Spatially resolved optical measurement geometry. **b)** Reflected white light microscopy image of a single CdS nanowire. **c)** Photoluminescence image of the wire shown in panel b).

At 77.6 K the body and end emission spectra as shown in Figure 5.3b by the blue and black lines respectively, are markedly less broad (FWHM of 30 meV and 19 meV respectively) and the end emission maximum (2.5108 eV) is markedly less red-shifted (13.7 meV) from the body emission (2.5322 eV) than at room temperature. In wurtzite CdS the valence band is split in three due to spin-orbit coupling and the crystal field with the valence bands labeled A, B and C, resulting in the formation of excitons labeled A, B and C from lowest to highest energy.³¹ In the body emission spectrum there is now a clear feature at 2.5433 eV which we assign to the CdS free A-exciton based on the literature values (vertical arrows) whereas there are no features that can be attributed to

the wurzite CdS B and C excitons. It must be remarked that the majority of the body emission in this wire occurs at energies lower than the lowest exciton energy, indicating alternate radiative processes to spontaneous exciton recombination (e.g. exciton-exciton scattering, exciton-phonon scattering and exciton trapping, see Figure 5.4c for further discussion). The end emission now shows much clearer Fabry-Pérot resonator intensity modulations in comparison to 298 K, a sign that the lifetime of the species in the resonator is increased (increased cavity quality factor). This is a clear demonstration of the polaritonic nature of the guided light in the cavity since the photon lifetime in a purely photonic cavity would not significantly be influenced by the lowered temperature³² whereas polaritons would find less phonons to scatter, increasing their lifetime.

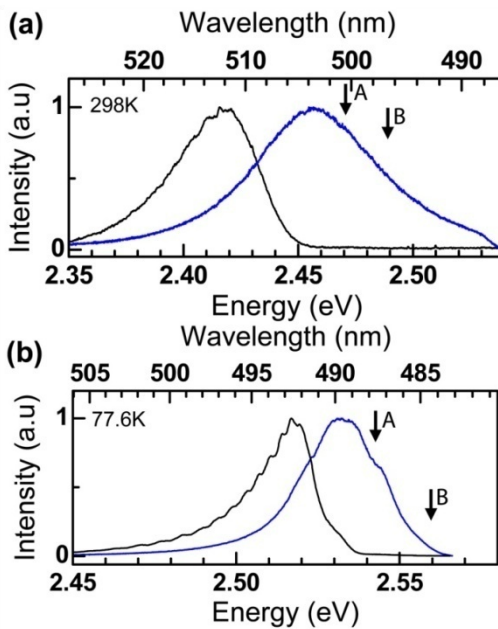


Figure 5.3: **a)** Room temperature photoluminescence spectra of the body emission (blue line) and the end emission (black line) of an unpassivated CdS nanowire **b)** 77.6 K photoluminescence spectra of the body emission (blue line) and the end emission (black line). In both panels the reference exciton energies²⁷ are indicated by the two vertical arrows.

Temperature-dependent body and end-emission of this same wire are shown in Figure 5.4a and Figure 5.4b, respectively. Aside from an overall red-shift in both spectra as temperature is increased due to a gradual reduction in bandgap, qualitatively features appear to maintain their overall form with no apparent drastic changes. To better understand the physical processes at work, individual peaks were tracked across multiple spectra at different temperatures with increments of 20 K and plotted in Figure 5.4c. Here, the upper and lower solid black lines show literature values for A- and B-excitons,²⁷ respectively, and the black and red dotted lines at low temperatures show discernable peaks in the body spectra which match these literature values well, suggesting they indeed originate from spontaneous free A- and B- exciton recombination. The magenta line immediately 12 meV (27 meV) beneath the free A-exciton (B-exciton) line indicates the energy of the body emission global maximum which corresponds to the near band-edge emission (NBE) observed in other temperature dependent studies on single CdS nanowires.²⁰ This line follows the literature exciton curves well and maintains near-constant distance throughout, suggesting it is exciton related. This peak falls in the energy range of the impurity bound B-exciton lines (19 to 32 meV below the B exciton^{33,34}) and since the emission is still visible at room temperature it follows that this emission does not originate from the A-exciton, since the 12 meV activation energy towards free A-exciton emission is easily overcome at elevated temperatures. All peaks at lower energetic positions than this magenta line indicate the positions of individual Fabry-Pérot cavity modes which red-shift with higher temperature as well. As an expression of the polaritonic nature of these modes it can be seen that the slope of the higher energy modes mimics that of the excitons whereas the lower energy (more

photonic) modes show a much smaller red-shift with temperature. Based on the data presented here we propose that in this (representative) uncoated CdS wire the dominant emission is excitonic but not from free excitons, and instead originating from deeply trapped (27 meV) B-excitons.

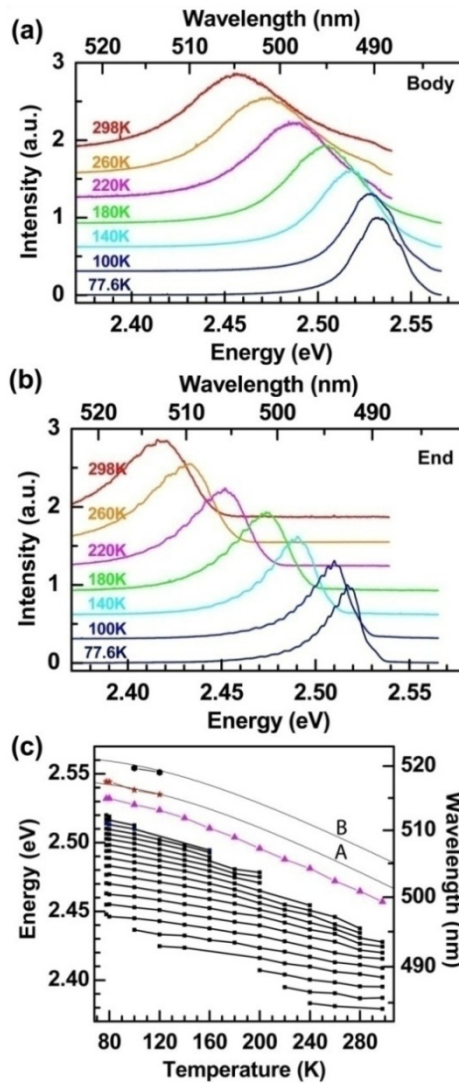


Figure 5.4: Photoluminescence spectra of the body **a)** and end **b)** emissions of an unpassivated CdS wire over the 77.6 K to 298 K temperature range. **c)** Temperature dependence of the observed photoluminescence peaks (the triangular magenta, star-shaped red, and hexagonal black data points) and the Fabry-Pérot peaks at lower energies (square black data points). The two solid black lines indicate reference data for the CdS A and B exciton energies.²⁷

Inspired by the positive effect of H_3PO_4 surface etching on the observation of excitonic features in CdS platelets,⁹ we grew a conformal SiO_2 shell around the CdS wires on the growth substrate using ALD with alternating pulses of O_3 , 3-aminopropyltriethoxysilane and H_2O . Figure 5.5a shows a TEM image of a CdS nanowire after 70 deposition cycles. A 5 nm amorphous shell can be discerned around the single crystalline CdS nanowire core as is indicated by the two lines. FTIR spectra obtained before and after SiO_2 deposition are displayed in Figure 5.5b.

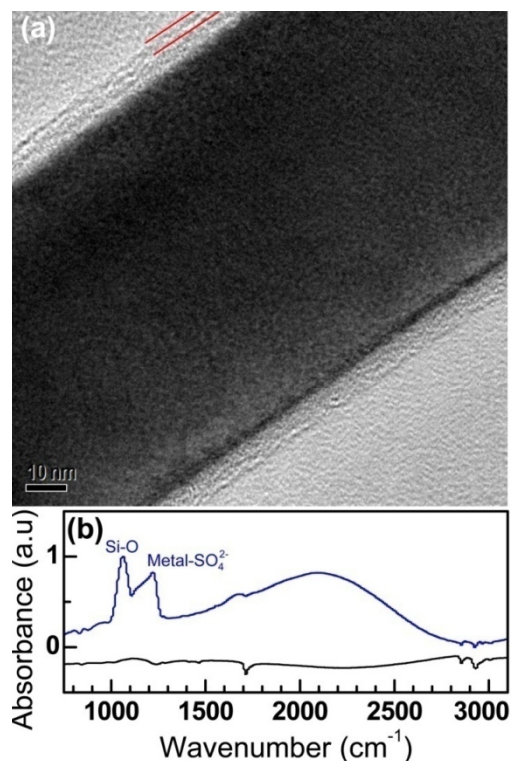


Figure 5.5: **a)** TEM image of a 5 nm SiO_2 ALD coated CdS nanowire. **b)** Fourier Transform Infrared absorption (FTIR) spectrum of an ensemble of SiO_2 passivated (blue line) and unpassivated (black line) CdS nanowires.

After deposition, peaks at 1062 cm^{-1} , 1221 cm^{-1} and 2080 cm^{-1} are clearly visible which can be attributed to Si-O-Si asymmetric stretching,^{35,36} M-SO_4^{2-} ³⁷ and nitrogen

compounds from the precursor³⁸ respectively. While the SiO₂ layer is amorphous and is not known to electronically passivate CdS surfaces, during the ALD treatment the first chemical pulse is O₃ which oxidizes the surface and causes the formation of sulfates which are known in literature to have an electronically passivating effect.^{32, 33} The amorphous silica shell further protects the sulfates against ad/desorption under the intense laser illumination and exposure to air. Thus we believe that the ALD treatment can result in a stable sulfate passivation of CdS nanowires, which will be further confirmed by optical spectroscopy.

In an analogue to Figure 5.3, Figure 5.6 shows body (blue) and end-emission (black) for a passivated 10.88 μm-long wire of diameter 186 nm at 298 K (a) and at 77.6 K (b) with literature values²⁷ for A- and B-exciton resonances in both indicated by vertical arrows. While the spectra at 298 K appear similar to their counterparts in Figure 5.3a (the Fabry-Pérot peak spacing is larger due to the shorter wire length) there is a slight (12 meV) blue shift of the maximum of the body emission. At 77.6 K the nanowire end spectrum shows a much sharper cutoff as it approaches the A-exciton resonance, while the body emission now is completely dominated by narrow peaks at both A- and B-resonances (2.5444 eV and 2.5597 eV) due to the absence of impurity bound excitons. We believe this enhancement of excitonic features to be the direct result of surface passivation due to the ALD SiO₂ deposition. In a logarithmic plot of the body emission from the coated wire at 77.6K shown in the inset of Figure 5.6b two additional peaks at lower energies of 2.5175 eV and 2.4772 eV can be discerned. These peaks are 41 meV and 82 meV separated from the B-exciton energy thus leading us to assign these peaks to the 1LO and 2LO phonon replicas of the B- exciton resonance. While most literature

reports an LO phonon energy of 37.6 meV^{34, 35} there is a study that reports of LO phonon energies at both 41 meV and 37.7 meV in ultra pure CdS crystals exhibiting free excitonic emission and less perfect crystals exhibiting bound exciton emission respectively.³⁶ Thus we assign the peaks 2.5175 eV and 2.4772 eV to the 1LO and 2LO phonon replicas of the B-exciton resonance in a high quality CdS crystal.

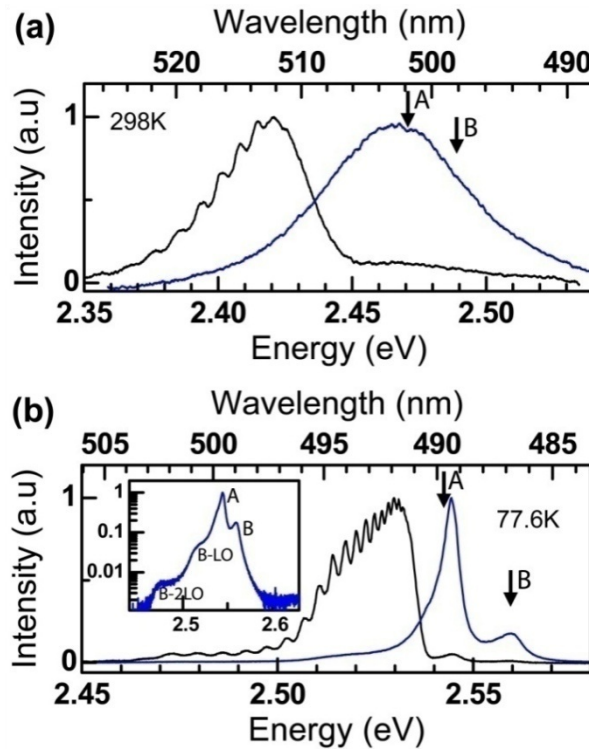


Figure 5.6: **a)** Room temperature photoluminescence spectra of the body emission (blue line) and the end emission (black line) of an unpassivated CdS nanowire. **b)** 77.6 K photoluminescence spectra of the body emission (blue line) and the end emission (black line). In both panels the reference exciton energies²⁷ are indicated by the two vertical arrows. The inset in panel b) shows the body emission at 77.6 K on a logarithmic scale.

Temperature-dependent measurements of both body- and end-emission from the SiO₂ coated wire are shown in Figure 5.7a and b, respectively, as well as a summary of

the observed PL and Fabry-Pérot lines in Figure 5.7c. The Fabry-Pérot resonances from the end emission are shown below the literature A- and B-exciton values in black,²⁷ while the four distinct peaks in the body emission are shown in black, red, magenta, and green. The black and red lines again follow literature exciton values and can be attributed to spontaneous free A- and B- excitonic emission. The magenta and green lines generally follow the curvature of both exciton lines, remaining a constant distance of 41 meV and 82 meV beneath the B-exciton energy throughout the temperature series. While the 2LO peak does not appear at temperatures above 240 K, the LO peak persists up to room temperature. Although the ALD coating process clearly improves the optical quality of the nanowires, we cannot remark on the absolute photoluminescence intensity before and after the process since the detected intensity in these single particle measurements depends too much on the nanowire alignment with the excitation and detection spots as well as the natural variation of properties between wires.

As shown in Chapter 4, by scanning the excitation laser over the nanowire whilst monitoring the spectrally resolved end emission, information about the energy-dependent propagation losses in the nanowires can be obtained.¹ The results of two separate experiments performed on the same passivated wire of 11.4 μm length and 185 nm diameter are shown in Figure 5.8. At left (a) are body (blue) and end (black) emission, and at right (b) is the propagation loss spectrum. The two images are aligned along the energy axis and the red lines drawn across all three show literature values²⁷ for the A- and B-free excitons at 77.6 K.

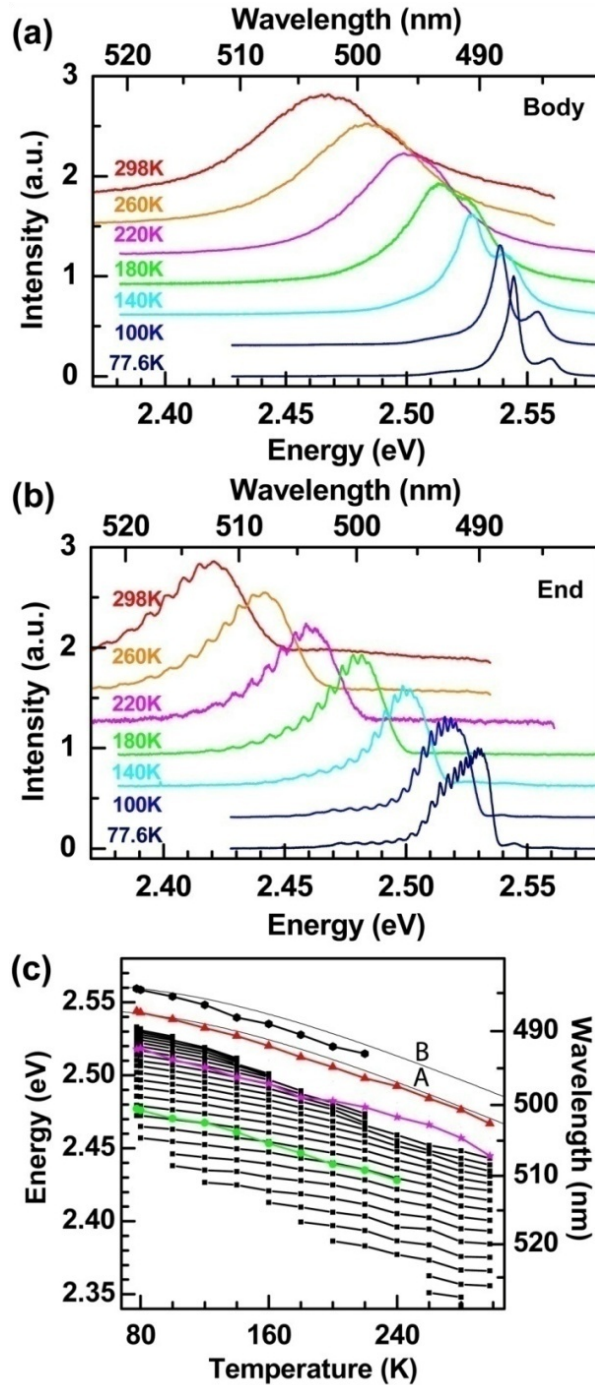


Figure 5.7: Photoluminescence spectra of the body **a)** and end **b)** emissions of SiO₂ coated CdS wire over the 77.6 K to 298 K temperature range. **c)** Temperature dependence of the observed photoluminescence peaks (the green, magenta, red and black data points) and the Fabry-Pérot peaks at lower energies (black square data points). The two solid black lines indicate reference data for the CdS A and B exciton energies.²⁷

Qualitatively, the shape of the propagation loss spectrum matches that of bulk CdS absorption³⁷ with the peak directly beneath the B-exciton ($6.240 \times 10^6 \text{ m}^{-1}$) showing more loss than the peak directly beneath the A-exciton ($3.138 \times 10^6 \text{ m}^{-1}$), and with a sharp drop in loss away from the excitonic region at energies below 2.535 eV. This sharp drop in propagation loss explains the significant red-shift of the guided emission shown in Figure 5.3 and Figure 5.6 as well as the decreased end emission width; since the detected end emission first has to travel to the nanowire end, the high loss in the excitonic region effectively shapes the guided spectrum and only allows detection of low loss emissions at lower energies. This shaping of the end emission is an absorptive process due to waveguiding phenomena, which causes less temperature sensitivity of the width of the end emission than that of the body emission. The two high-energy peaks at the A- and B-exciton resonances yield propagation lengths of 320 and 160 nm respectively, both significantly shorter than the nanowire length and within the same order of magnitude of free exciton diffusion lengths determined for CdS platelets.¹¹ Despite their very slight red-shift from literature values, this is further evidence that the peaks in propagation loss are indeed free-exciton related.

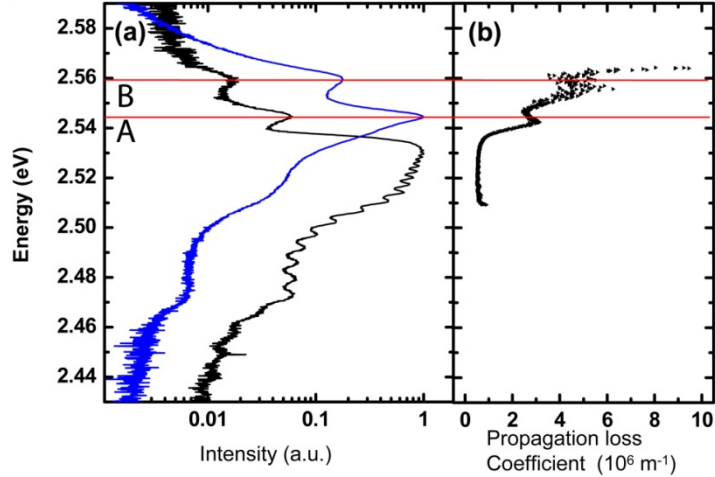


Figure 5.8: **a)** Photoluminescence spectra of the body (blue line) and end (black line) emissions of a SiO₂ coated CdS wire at 77.6 K. Wire length 11.4 μm and diameter 185 nm. **b)** Propagation loss spectrum of this same wire.

In conclusion, we have shown that the optical quality of wurtzite CdS nanowires can be dramatically improved by a conformal ALD coating with a 5 nm SiO₂ capping layer. The passivation effect is attributed to the formation of sulfates on the CdS nanowire surface due to reaction with O₃ during the ALD process, after which the amorphous SiO₂ layer seals the passivated wire against damage under laser illumination. As-grown unpassivated wurtzite CdS nanowires show only discernable free A- and B- exciton emission at temperatures below 120 K whereas the dominant emission at 12 meV lower energy than the A-exciton line, tentatively assigned to deep trapping of the B- exciton, persists up to 298K. Upon passivation, clear A- and B- free exciton peaks are observed that are resolvable up to 220 and 298 K respectively. Surprisingly, only the B- exciton seems to interact with optical phonons, and 1LO and 2LO peaks are observed at temperatures up to 298 K and 240 K respectively with an LO phonon energy of 41 meV. Propagation loss experiments on the passivated wires showed a clear correspondence

between observed exciton luminescence peaks and peaks in the propagation loss. These measurements explain the large red-shift of the guided emission emerging at the wire ends since at higher energies very close to the exciton resonances the absorption/propagation loss is too large (peak values of $3.138 \times 10^6 \text{ m}^{-1}$ and $6.240 \times 10^6 \text{ m}^{-1}$ for the A- and B- exciton, respectively) for the polariton to propagate to the end of the nanowire. These results demonstrate the high optical quality of the nanowire crystals and provide the fundamental input parameters for strong light-matter coupling studies in these CdS nanowire waveguide cavities, potentially leading to low threshold polariton lasers, sensitive sensors and optical switches at the nanoscale.

References

1. Piccione, B., Vugt, L.K.v. & Agarwal, R. Propagation Loss Spectroscopy on Single Nanowire Active Waveguides. *Nano Letters* **10**, 2251 (2010).
2. Andrew, B.G., Carl, J.B., Yat, L. & Charles, M.L. Semiconductor nanowire laser and nanowire waveguide electro-optic modulators. *Applied Physics Letters* **87**, 151103 (2005).
3. van Vugt, L.K., Piccione, B. & Agarwal, R. Incorporating polaritonic effects in semiconductor nanowire waveguide dispersion. *Applied Physics Letters* **97**, 061115 (2010).
4. Duan, X., Huang, Y., Agarwal, R. & Lieber, C.M. Single-nanowire electrically driven lasers. *Nature (London)* **421**, 241 (2003).
5. Agarwal, R., Barrelet, C.J. & Lieber, C.M. Lasing in Single Cadmium Sulfide Nanowire Optical Cavities. *Nano Letters* **5**, 917-920 (2005).
6. Ekimov, A.I. & Onushchenko, A.A. Quantum size effect in three-dimensional microscopic semiconductor crystals. *JETP Lett.* **34**, 345 (1981).
7. Wang, Y. & Herron, N. Nanometer-Sized Semiconductor Clusters: Materials Synthesis, Quantum Size Effects, and Photophysical Properties. *J. Phys. Chem.* **95**, 525 (1991).
8. Vossmeier, T. et al. CdS Nanoclusters: Synthesis, Characterization, Size Dependent Oscillator Strength, Temperature Shift of the Excitonic Transition Energy, and Reversible Absorbance Shift. *Journal of Physical Chemistry* **98**, 7665 (1994).
9. Thomas, D.G. & Hopfield, J.J. Exciton Spectrum of Cadmium Sulfide. *Physical Review* **116**, 573 (1959).
10. Voigt, J., Sengner, M. & Ruckmann, I. Quantitative Analysis of Interference Structures in the Transmission Spectrum of Very Thin CdS Platelets. *Phys. Stat. Sol. B* **75**, 213 (1976).
11. Klingshirn, C. et al. Optical Nonlinearities and Bistabilities in Highly Photo-Excited II-VI Compounds. *Journal of Luminescence* **40**, 64 (1988).
12. Hopfield, J.J. & Thomas, D.G. Polariton Absorption Lines. *Physical Review Letters* **15**, 22 (1965).
13. Hopfield, J.J. & Thomas, D.G. Theoretical and Experimental Effects of Spatial Dispersion on the Optical Properties of Crystals. *Physical Review* **132**, 563 (1963).
14. van Vugt, L.K. et al. Exciton-Polaritons Confined in a ZnO Nanowire Cavity. *Physical Review Letters* **97**, 147401 (2006).
15. Gibbs, H.M. & Khitrova, G. Semiconductors: Excitonic lattice control. *Nat Photon* **3**, 613-615 (2009).
16. Deng, H., Weihs, G., Snoke, D., Bloch, J. & Yamamoto, Y. Polariton lasing vs. photon lasing in a semiconductor microcavity. *Proceedings of the National Academy of Sciences of the United States of America* **100**, 15318-15323 (2003).

17. Hagele, D., Pfalz, S. & Oestreich, M. Towards Bose-Einstein Condensation of Semiconductor Excitons: The Biexciton Polarization Effect. *Physical Review Letters* **103**, 146402 (2009).
18. Kasprzak, J. et al. Bose-Einstein condensation of exciton polaritons. *Nature (London)* **443**, 409-414 (2006).
19. van Vugt, L.K., Veen, S.J., Bakkers, E.P.A.M., Roest, A.L. & Vanmaekelbergh, D.I. Increase of the Photoluminescence Intensity of InP Nanowires by Photoassisted Surface Passivation. *Journal of the American Chemical Society* **127**, 12357-12362 (2005).
20. Hoang, T.B. et al. Temperature dependent photoluminescence of single CdS nanowires. *Applied Physics Letters* **89**, 123123 (2006).
21. Jung, Y., Ko, D.-K. & Agarwal, R. Synthesis and Structural Characterization of Single-Crystalline Branched Nanowire Heterostructures. *Nano Letters* **7**, 264-268 (2006).
22. Wagner, R.S. & Ellis, W.C. VLS mechanism. *Applied Physics Letters* **4**, 89-91 (1964).
23. Wu, Y. & Yang, P. Direct Observation of Vapor-Liquid-Solid Nanowire Growth. *Journal of the American Chemical Society* **123**, 3165-3166 (2001).
24. Duan, X. & Lieber, C.M. General Synthesis of Compound Semiconductor Nanowires. *Advanced Materials* **12**, 298-302 (2000).
25. Bakkers, E.P.A.M. et al. Epitaxial growth of InP nanowires on germanium. *Nature Materials* **3**, 769-773 (2004).
26. Dick, K.A. et al. Failure of the Vapor-Liquid-Solid Mechanism in Au-Assisted MOVPE Growth of InAs Nanowires. *Nanoletters* **5**, 761 -764 (2005).
27. Imada, A., Ozaki, S. & Adachi, S. Photoreflectance spectroscopy of wurtzite CdS. *Journal of Applied Physics* **92**, 1793-1798 (2002).
28. Johnson, J.C., Yan, H., Yang, P. & Saykally, R.J. Optical Cavity Effects in ZnO Nanowire Lasers and Waveguides. *The Journal of Physical Chemistry B* **107**, 8816-8828 (2003).
29. van Vugt, L.K., Röhle, S. & Vanmaekelbergh, D.I. Phase-Correlated Nondirectional Laser Emission from the End Facets of a ZnO Nanowire. *Nano Letters* **6**, 2707-2711 (2006).
30. van Vugt, L.K., Zhang, B., Piccione, B., Spector, A.A. & Agarwal, R. Size-Dependent Waveguide Dispersion in Nanowire Optical Cavities: Slowed Light and Dispersionless Guiding. *Nano Lett.* **9**, 1684-1688 (2009).
31. Klingshirn, C.F. *Semiconductor Optics* (Springer-Verlag, Berlin, 2007).
32. Mayer, D., Hallmeier, K.H., Chassé, T. & Szargan, R. SXPS analysis of passivation and complexation on the CdS (101⁻ 0) surface. *Fresenius' Journal of Analytical Chemistry* **361**, 689-692 (1998).
33. Chang, S.-y., Liu, L. & Asher, S.A. Preparation and Properties of Tailored Morphology, Monodisperse Colloidal Silica-Cadmium Sulfide Nanocomposites. *Journal of the American Chemical Society* **116**, 6739 (1994).
34. Thomas, D.G. & Hopfield, J.J. Optical Properties of Bound Exciton Complexes in Cadmium Sulfide. *Physical Review* **128**, 2135 (1962).

35. Fan, H.M. et al. Orientation-Dependent Raman Spectroscopy of Single Wurtzite CdS Nanowires. *The Journal of Physical Chemistry C* **112**, 1865-1870 (2008).
36. Benoit À La Guillaume, C., Debever, J.-M. & Salvan, F. Radiative recombination in highly excited CdS. *Physical Review* **177**, 567 (1969).
37. Shalimova, K.V. & Khirin, V.N. Mechanism for the optical absorption of Cadmium Sulfide. *Soviet Physics Journal* **12**, 487-491 (1969).

Chapter 6. **Incorporating Polaritonic Effects in Semiconductor Nanowire Waveguide Dispersion**

Reproduced in part with permission from Applied Physics Letters, Volume 97, Issue 6, Page 061115. Copyright 2010 American Institute of Physics.

As discussed in Chapter 3, light propagation in semiconductor nanowires can be described by the energy-wavevector dispersion ($E-k$) and the group velocity can theoretically be obtained by solving Maxwell's equations with appropriate boundary conditions if the dielectric functions $\epsilon(\omega)$ of the core and cladding materials are known.¹ A common approach to include this material dispersion into waveguide dispersion calculations is by using a phenomenological Sellmeier-type equation in which the coefficients are obtained by numerical fitting to dielectric dispersion obtained from measurements on macroscopic crystals.² Although this approach gives satisfactory results at energies much lower than the electronic bandgap, deviations at energies close to the bandgap occur, particularly if excitons are present.³

As discussed in Section 1.2, excitons can strongly couple to the light field resulting in the formation of composite particles with both electronic and photonic character, exciton-polaritons,⁴ resulting in the formation of anti-crossing upper and lower polariton branches and drastic changes to the dielectric function. In order to describe the energy-wavevector dispersion and group velocity in these nanowire waveguides accurately, it is highly desirable to explicitly include physical quantities such as the transverse and longitudinal exciton resonance frequencies (which relates to light-matter coupling strength) and their damping constants in the analysis so that that nanoscale size effects can be readily incorporated. In this chapter we show how in CdS nanowires the

waveguide dispersion is altered due to the presence of excitons (binding energy 27 meV),⁵ which strongly couple to the confined photonic waveguide modes. After calculating the waveguide E - β dispersion for the purely photonic modes using a Sellmeier type equation, we introduce electronic resonance effects into the calculations via the polaritonic contributions to the dielectric function. Next, these calculations are compared with experimental data obtained on CdS nanowires and finally, we briefly discuss the implications of the strongly modified dispersion on photonic switching and sensing with nanowires.

CdS nanowires were obtained by the vapor-liquid-solid method using evaporation of CdS powder (99.999% Sigma Aldrich) and 5 nm Au/Pd covered silicon substrates.⁶ After synthesis, the nanowires were transferred to Si substrates covered with a 300 nm thermal oxide. The substrates contained markers so that individual wires could be characterized by both scanning electron (SEM) and optical microscopy. Optical experiments were carried out using a home-built microscope equipped with a Nikon 60X 0.7 NA objective as described previously.⁹

To calculate the confined photonic modes in the CdS nanowires, we simplified the wire geometry to that of a cylindrical step-index fiber of radius r with a CdS core (refractive index $n_{co}(\lambda)$) and air cladding ($n_{clad}=1$). It was previously shown that this simplification does not markedly influence the correspondence of the calculated modes with the experimental data. In addition, we omitted consideration of a small phase shift upon reflection at the nanowire ends^{3, 7} which is not significant for long nanowires. Generally, the waveguide modes of cylindrical waveguides are of a hybrid nature, that is

the electric and magnetic fields can have components in the propagation direction, z . The transverse electric (TE) and or transverse magnetic (TM) modes can be considered special cases of the hybrid modes where either the electric or the magnetic fields in the propagation direction vanish. From Maxwell's equations and the boundary condition of continuous tangential fields at the fiber surface, exact eigenvalue equations can be formulated for the various modes, as shown previously in Equations 3.1 through 3.6.¹ Subsequently, these eigenvalue equations were numerically solved for the propagation constant β at each wavelength using a core refractive index defined by a Sellmeier equation obtained from macroscopic CdS crystals.⁸ The results of these calculations are plotted in Figure 6.1a and Figure 6.1b as red dashed lines for two CdS nanowires with radii of 120 nm (a, TM₀₁ mode) and 255 nm (b, HE₁₂ mode) as determined from SEM imaging (inset in Figure 6.1a and Figure 6.1b), together with the dispersion of light in air (dotted). The calculated modes are to the right of the light line, showing that these modes are indeed confined to the nanowire core and are therefore waveguide modes.

Next, to include dispersive effects due to the presence of excitonic resonances and polariton formation, we introduce a dispersive core refractive index $n_{co}(\lambda)$ that is taken as the real part of the square root of the dielectric function, where the dielectric function in the vicinity of the CdS excitons A and B⁹ can be described by a coupled oscillator model for two closely spaced resonances:¹⁰

$$\epsilon(\omega) = \epsilon_b \left(1 + \frac{\omega_{BL}^2 - \omega_{AT}^2}{\omega_{BT}^2 - \omega_{AT}^2} \frac{\omega_{AL}^2 - \omega_{AT}^2}{\omega_{AT}^2 - \omega^2 - i\omega\Gamma_A} + \frac{\omega_{AL}^2 - \omega_{BT}^2}{\omega_{AT}^2 - \omega_{BT}^2} \frac{\omega_{AL}^2 - \omega_{AT}^2}{\omega_{BT}^2 - \omega^2 - i\omega\Gamma_B} \right) \quad \text{Eq. 6.1}$$

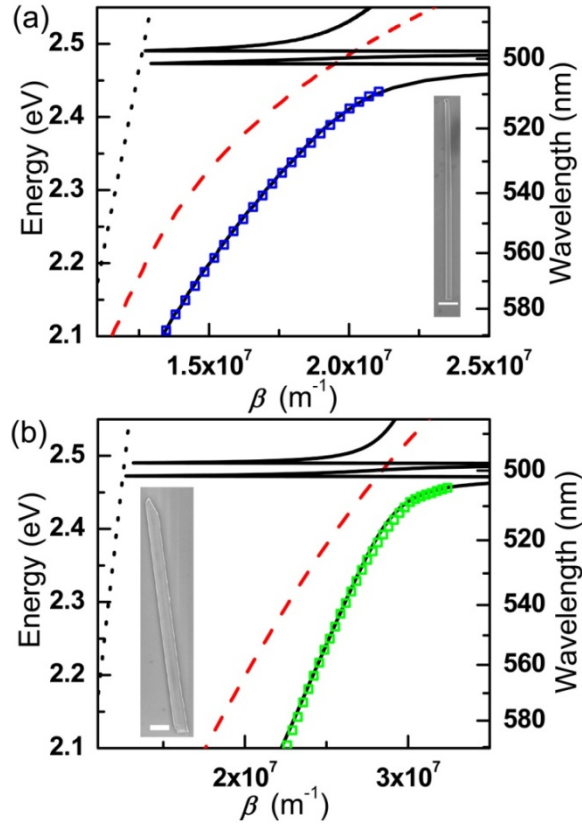


Figure 6.1: **a)** Waveguide dispersion for the TM_{01} mode of a CdS nanowire with a radius of 120 nm calculated using a Sellmeier equation² for material dispersion (dashed red line) and the polaritonic model (full black line). (Inset) SEM image of the wire. **b)** Waveguide dispersion for the HE_{12} mode of a CdS nanowire with a radius of 255 nm calculated using a Sellmeier equation for material dispersion² (dashed red line) and the polaritonic model (full black line). (Inset) SEM image of the wire. The dispersion of light in air is shown in both panels by the black dotted lines. The square data points are determined from the spectra shown in Figure 6.2. Scale bar, 500 nm.

Where ϵ_b is the background dielectric constant, ω_{AT} and ω_{AL} are the A-exciton transverse and longitudinal resonance frequencies, ω_{BT} and ω_{BL} are the B-exciton transverse and longitudinal resonance frequencies, Γ_A the A-exciton damping and Γ_B the B-exciton damping. We have omitted spatial dispersion since in our investigated energy range the UPB is severely damped and only modes on the LPB propagate along the

nanowire.¹¹ Numerically solving the mode eigenequations, which now include the resonance effects, with bulk parameters $\epsilon_b=8$,¹² $\hbar\omega_{AT}=2.4696$ eV,⁵ $\hbar\omega_{AL}=2.4715$ eV,¹² $\hbar\omega_{BT}=2.4882$ eV,⁵ $\hbar\omega_{BL}=2.4895$ eV,¹² $\hbar\Gamma_A=\hbar\Gamma_B=10$ μeV ¹³ leads to the dispersions plotted as black solid lines in Figure 6.1a and Figure 6.1b. At low energies the mode mimics a purely photonic mode but closer to the resonances the dispersion flattens out and resembles the dispersion of the electronic resonances. This is due to the dual nature of the exciton-polaritons having more electronic or photonic character depending on the energy and propagation constant.

To verify our calculations experimentally, CdS nanowires were excited non-resonantly across the bandgap at one end whereas the waveguided photoluminescence was collected at the other end of the wire. The collected spectra (Figure 6.2) consist of a strong peak of near band-edge emission which is periodically modulated. It has been previously demonstrated that these modulations are the result of standing wave formation inside the nanowire (i.e. the nanowire acts as a longitudinal Fabry-Pérot cavity^{14, 15}) with cavity modes equidistantly spaced in reciprocal space at integer multiples of π/L , with L the cavity (nanowire) length.^{12, 16} Thus, the interference peaks in the waveguided photoluminescence spectrum can be used to reconstruct the waveguide dispersion.^{3, 15, 16} The extracted peak positions for the spectra of the two wires are plotted in Figure 6.1a and Figure 6.1b. A striking resemblance between the experimental data and the calculated polaritonic dispersions can be seen, whereas the correspondence with the modes calculated using the Sellmeier equation is poor. This demonstrates that this method of incorporating polaritonic effects into nanowire waveguide dispersion is valid and more

appropriate than the phenomenological approach for its accuracy and flexibility towards incorporating real physical parameters.

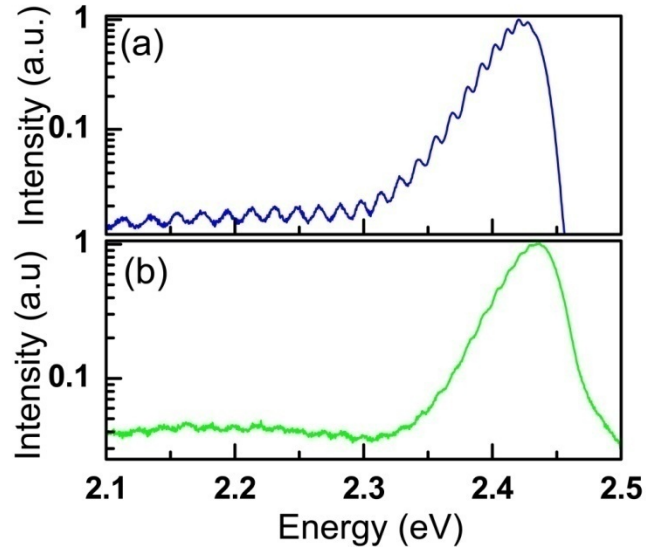


Figure 6.2: Emission spectra of guided photoluminescence light for **a)** a 9.59 μm long wire with a radius of 120 nm and **b)** a 9.10 μm long wire with a radius of 255 nm. Note the logarithmic intensity scale used to show the intensity modulations.

The strong coupling of light with matter whilst still maintaining a propagation length of at least twice the nanowire length as evidenced by the Fabry-Pérot interference peaks offers interesting opportunities. For instance, the strong curvature of the dispersion implies that the group index defined as $(dE/d\beta)_{\text{vacuum}}/(dE/d\beta)_{\text{mode}}$ dramatically goes up, reducing signal velocity, which can be beneficial for the sensitivity of a nanowire optical sensor due to an increased interaction time.¹⁷ In Figure 6.3, the group index of the photonic (dashed lines) and polaritonic (solid lines) modes are shown for the same nanowires. The photonic modes show a relatively constant low group index over the investigated energy range whereas the polaritonic modes reach up to a group index of 20.

Furthermore, since the slowing of the signal velocity is dependent on the presence of excitons, it can be expected that the signal retardation can be switched by using low modulation intensities since the exciton resonances can be bleached by pumping up to the CdS exciton Mott density.¹¹ At the Mott density, the exciton dissociates into free electron and holes due to screening and the resonance disappears from the spectrum and thus the waveguide dispersion reverts back to the purely photonic one.

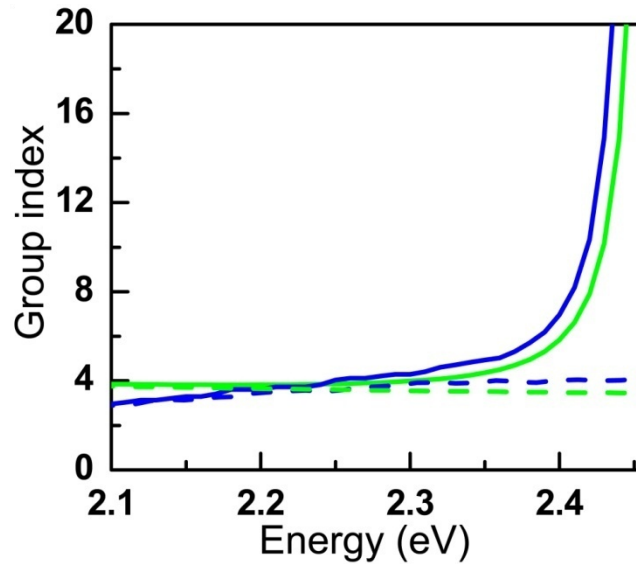


Figure 6.3: Group index vs. energy for purely photonic (dashed lines) and polaritonic (solid lines) modes of the 120 nm radius (blue) and 255 nm radius wire (green). The figure is cut-off at the highest group index that was experimentally determined.

In conclusion, we have shown that close to the electronic band edge in CdS nanowires, polaritonic contributions to the dielectric function need to be taken into account in order to accurately describe the experimentally observed E - β dispersion of the confined waveguide modes. Furthermore, we include these effects by using a physical model of coupled oscillators which takes into account the different excitons that are

present in the system. The coupled oscillator model has the advantage that it fits with basic exciton oscillator parameters such as their transverse and longitudinal resonance energies, which are directly related to the oscillator strength of the transitions, and their damping. The polaritonic effect in CdS nanowires at room temperature slowed the signal propagation velocity by a factor of 7 more when compared to purely photonic propagation, making polaritonic nanowires prime candidates for sensing and photonic switching applications.

References

1. Snyder, W. & Love, J.D. Optical Waveguide Theory (Chapman and Hall, London, 1983).
2. Ninomiya, S. & Adachi, S. Optical properties of wurtzite CdS. *Journal of Applied Physics* **78**, 1995 (1995).
3. Vugt, L.K.v., Piccione, B., Spector, A.A. & Agarwal, R. Size-Dependent Waveguide Dispersion in Nanowire Optical Cavities: Slowed Light and Dispersionless Guiding. *Nano Letters* **9**, 1684 (2009).
4. Hopfield, J.J. Theory of the contribution of Excitons to the Complex Dielectric Constant of Crystals. *Physical Review* **112**, 1555-1567 (1958).
5. Anedda, A. & Fortin, E. Temperature shift of Excitons in CdS. *Physica Status Solidi A: Applications and Materials Science* **36**, 385 (1976).
6. Jung, Y., Ko, D.K. & Agarwal, R. Synthesis and structural characterization of single-crystalline branched nanowire heterostructures. *Nano Letters* **7**, 264-268 (2007).
7. Bordo, V.G. Model of Fabry-Pérot-type electromagnetic modes of a cylindrical nanowire. *Physical Review B: Condensed Matter* **81**, 035420 (2010).
8. Ninomiya, S. & Adachi, S. Optical properties of wurtzite CdS. *Journal of Applied Physics* **78**, 1183 (1995).
9. The valence band in CdS is split into an A, B and C band due to spin-orbit coupling and the crystal field, resulting in the formation of A,B and C excitons. Due to the large energy difference of the highest energy C exciton with the A and B excitons and its lower oscillator strength, only the A and B excitons are taken into account.
10. Lagois, J. Dielectric Theory of Interacting excitonic Resonances. *Physical Review B: Condensed Matter* **16**, 1699-1705 (1977).
11. Klingshirn, C.F. Semiconductor Optics (Springer-Verlag, Berlin-Heidelberg-New York, 1997).
12. Voigt, J., Senoner, M. & Rückmann, I. Quantitative Analysis of interference structures in the transmission spectrum of very thin CdS Platelets. *Physica Status Solidi B: Basic Solid State Physics* **75**, 213 (1976).
13. For calculation purposes a finite damping was included.
14. Johnson, J.C., Yan, H., Yang, P. & Saykally, R.J. Optical Cavity Effects in ZnO Nanowire Lasers and waveguides. *Journal of physical chemistry B* **107**, 8816-8828 (2003).
15. Vugt, L.K.v., Rühle, S. & Vanmaekelbergh, D. Phase-correlated non-directional laser emission from ZnO nanowires. *Nano Letters* **6**, 2707-2711 (2006).
16. Kiselev, V.A., Razbirin, B.S. & Uraltsev, I.N. Additional Waves and Fabry-Perot Interference of Photoexcitons (Polaritons) in Thin II-VI Crystals. *Physica Status Solidi B: Basic Solid State Physics* **72**, 161-172 (1975).
17. Mortensen, N.A. & Xiao, S. Slow-light enhancement of Beer-Lambert-Bouguer absorption. *Applied Physics Letters* **90**, 141108 (2007).

Chapter 7. **One-Dimensional Polaritons With Size-Tunable and Enhanced Coupling Strengths in Semiconductor Nanowires**

Reproduced in part for noncommercial use from Proceedings of the National Academy of Sciences of the United States of America, Volume 108, Issue 25, Pages 10050-10055. Copyright 2011 The National Academy of Sciences.

Exciton-polaritons^{1, 2} are fundamental to many exciting observations due to their hybrid photonic-electronic properties, including reduced effective mass when compared with excitons, bosonic particle statistics, long coherence lengths and large scattering cross-sections.³ While strong optical coupling in the single-quantum limit provides tremendous possibilities for quantum information processing through quantum electrodynamic effects,^{4, 5} it is through the use of strong optical coupling in many particle systems that novel phenomena such as Bose-Einstein condensation in the solid state^{6, 7} and low-threshold polariton lasing and light emission^{8, 9} have been discovered. In addition, many particle strong coupling provides tremendous possibilities for slow-light¹⁰ and terahertz¹¹ applications using many particle effects.

The strong-coupling regime in the solid-state is generally obtained by confining excitons in semiconductor quantum dots (QD) and wells (QW) in order to enhance their oscillator transition strengths and coupling them to the low-loss optical mode of small mode volume optical cavities that enhance the electromagnetic field density.^{2, 12-15} The coupling strength is expressed as the Rabi frequency, $g \propto \sqrt{n * f / V_m}$,^{4, 13, 16} with n the number of oscillators, f their oscillator strength and V_m the mode volume, noting that the photon lifetime as determined by cavity quality factor (Q) should be long enough to allow for the Rabi oscillation to occur. The extremely high Q of micropillar cavities,¹³ photonic

slab crystals¹⁴ and micro-toroids¹⁷ have previously allowed QWs and QDs embedded at optical field antinodes to exhibit strong coupling, even though the oscillator strengths were not necessarily optimal due to the choice of material (GaAs) as dictated by the state of the art in thin-film processing technology. Additionally, these top-down fabricated structures have a large footprint coupled with the challenges of preventing surface roughness and exciton dead layers during etch processes for laterally confined systems, which strongly limits their potential to achieve very high coupling strengths.

The need for a very high Q cavity can be avoided by using semiconductors with high intrinsic exciton oscillator strengths such as ZnO, CdS and GaN,^{1, 3, 18} or organic materials,¹⁹ providing a logical starting point for the observation and manipulation of strong-coupling phenomena. Indeed, exciton-polariton formation in bulk ZnO and CdS crystals has been measured up to room temperature.¹ However these polaritons are a bulk phenomenon and consequently not much attention has been devoted to manipulating their coupling strengths beyond bulk values, aside from some studies where only the bulk polariton coupling strength was recovered in large lateral cavities by placing $\lambda/2$ and 2λ thick active GaAs layers between DBRs.²⁰

Here we demonstrate the manipulation of bulk polaritons into one-dimensional cavity-polaritons with size-tunable enhancement of the light-matter coupling strength, using self-assembled, surface-passivated excitonic CdS nanowire optical waveguide cavities exhibiting strong lateral confinement, circumventing surface roughness and electronically dead layer problems associated with top-down fabricated nanocavities. We extract the coupling strengths from these difficult-to-access cavities by fitting a recently

developed one parameter (coupling strength) model that incorporates nanowire waveguide dispersion and exciton-polariton formation, to Fabry-Pérot modes measured from the nanowire end facets^{21, 22} that otherwise obstruct angle resolved measurements due to diffraction at these subwavelength apertures. Additional surface passivation²³ allows us to push the observed vacuum Rabi splitting to values of up to 200 meV in comparison to bulk values of 82 meV. These results provide new avenues to achieve very high coupling strengths (beyond bulk) enabling application of exciting phenomena such as Bose-Einstein condensation of polaritons, efficient light-emitting diodes and lasers, optical switching, and slow-light applications, all in a subwavelength waveguide geometry with a small footprint that can be readily integrated into nanophotonic circuitry.

7.1. Materials and Methods

CdS nanowire crystals were obtained using the growth and passivation conditions described in Chapter 5. CdS nanowires were dispersed onto silicon oxide substrates and mounted with silver paint in a continuous flow optical microscopy cryostat, which was kept at 77 K using liquid nitrogen. The continuous wave 457.9 nm Ar ion excitation laser beam was directed at one end of each nanowire. Guided photoluminescence from the individual wires was collected in the same manner as described previously.

7.2. Experimental Results

In order to investigate the influence of cavity size and dimensionality on the light-matter coupling strength in CdS crystals, single-nanowire cavities were studied by SEM

(Figure 7.1a). From electron backscatter diffraction (EBSD) data (Figure 7.1a, upper inset), we determined that the CdS nanowires had the wurzite crystal structure with the $[10\bar{1}0]$ direction (a -axis) oriented along the nanowire long axis. The configuration of the optical experiments (Figure 7.1b) consists of a focused laser spot exciting one end of the nanowire cavity whilst detecting the spatially and spectrally-resolved emission which has been guided to the other end of the wire (Figure 7.1c). Emission spectra of the guided emission collected at the non-excited end of the wires (Figure 7.2a, c and e, for wires with diameters of 260, 190 and 200 nm and lengths of 7.9, 8.1 and 2.46 μm respectively) show multiple intensity modulations due to longitudinal Fabry-Pérot modes caused by reflections at the nanowire ends. The energetic positions of these cavity resonances were extracted by fitting with a series of Lorentzian line-shapes with quality factors ranging from 350-950 and can be used to reconstruct the energy-wavevector dispersion of the propagating mode by placing these peaks at integer multiples of π/L in the wavevector space.²¹ These experimental points are plotted in Figure 7.2b, d and f for the nanowires with diameters of 260, 190 and 200 nm respectively. It is apparent that these experimentally determined dispersion curves of the propagating modes show significant curvature which is not expected for purely photonic modes.²¹

We fitted these points to our model for the waveguide dispersion in a polaritonic circular cross-section step-index semiconductor waveguide²² with the transverse resonance frequencies of the CdS A and B excitons (at 77 K) as were determined in our propagation spectroscopy experiments,²⁴ and from the corresponding PL peaks.²³ For the 260 nm diameter wire of length 7.9 μm (Figure 7.2b), an excellent fit was obtained by

strong coupling of the B-exciton to the fundamental HE_{11} guided mode using the bulk value of 1.4 meV for the longitudinal-transverse splitting (ΔE_{LT}),²⁵ a quantity which is proportional to the square of the oscillator strength.²⁶ However, good fits to the HE_{11} fundamental mode can only be obtained for the 190 nm x 8.1 μm and 200 nm x 2.46 μm (diameter x length) wires by increasing ΔE_{LT} to 4.5 and 6 times the bulk value respectively. Good fits to other higher order waveguide modes such as the TE_{01} and TM_{01} could not be obtained and interestingly, the dispersions show no sign of coupling to the CdS A-exciton. This can be understood by considering the polarization properties of the involved excitons and the waveguide mode;²⁷ due to the wurtzite crystal structure and the a -axis along the growth direction of the nanowires, the A-exciton oscillator has no dipole moment along the transverse nanowire cavity directions,²⁵ which precludes any coupling to the transversely polarized fundamental HE_{11} mode.

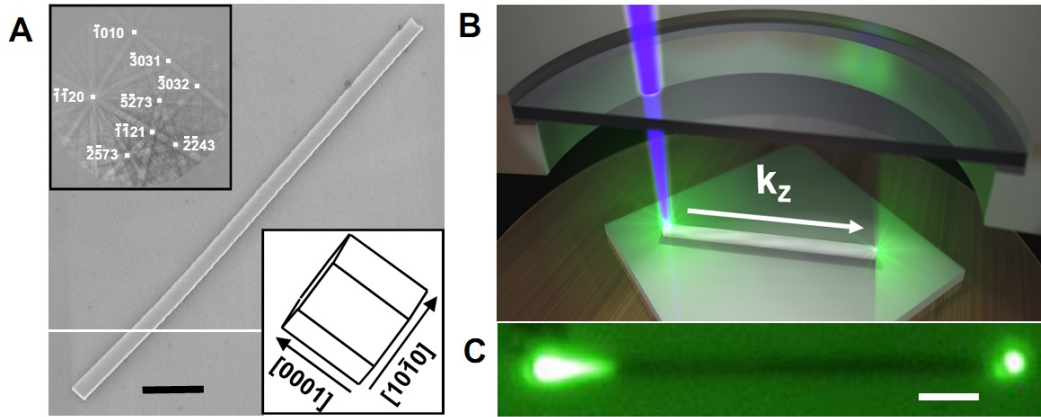


Figure 7.1: CdS nanowire waveguide cavity and low-temperature micro-photoluminescence experimental geometry. **a)** SEM picture of a CdS nanowire lying on the SiO_2 measurement substrate. Scale bar, 1 μm . In the top inset the electron backscatter diffraction pattern is shown, indicating wurtzite CdS with a unit cell orientation as shown in the lower inset. **b)** Schematic of the experimental geometry showing a nanowire laying on the substrate inside a cryostat at 77K. The wire is excited at the left end and only the wave-guided emission is collected at the right. **c)** Low-resolution optical micrograph of PL resulting from exciting the CdS nanowire from the left. The scale bar is 2 μm .

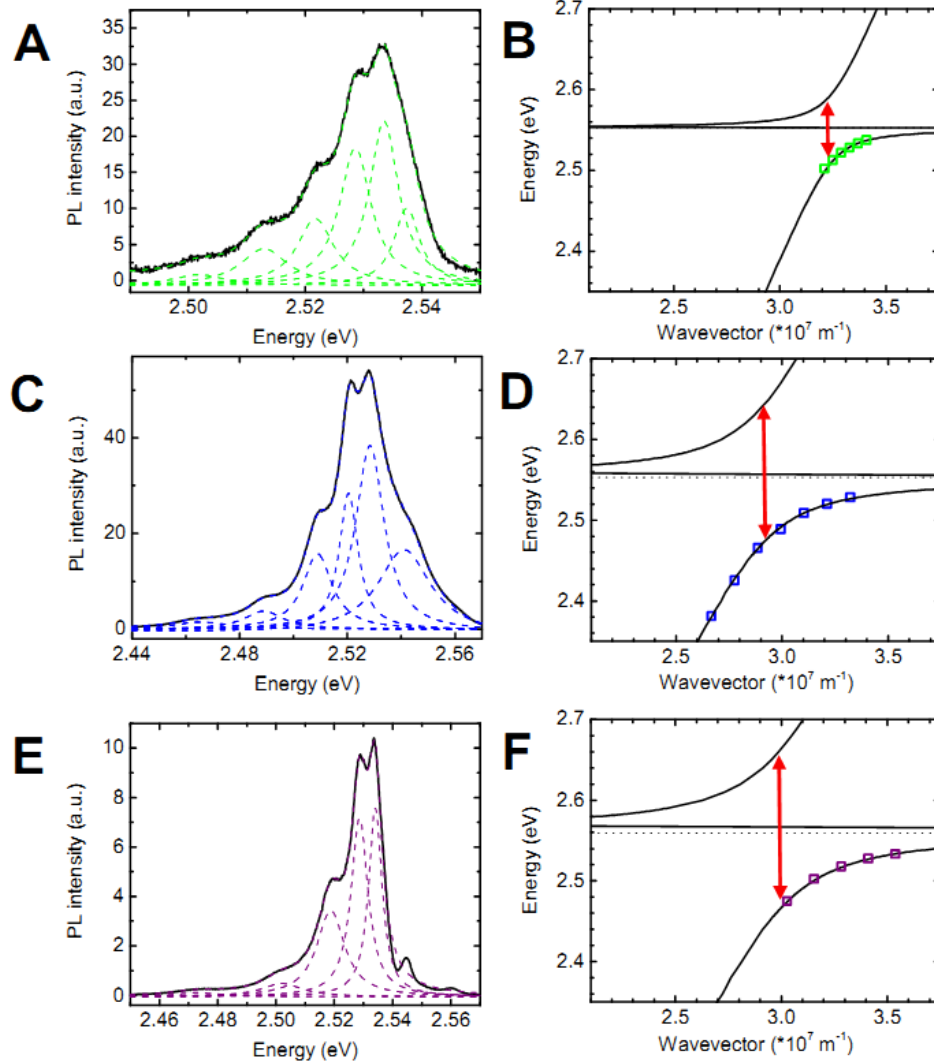


Figure 7.2: Photoluminescence spectra of the guided emission and size-dependent light-matter coupling strength. **a), c), e)** PL spectra of emission collected at the guided (non excited) ends of nanowires with diameter \times length dimensions of a) 260 nm \times 7.9 μm , c) 190 nm \times 8.1 μm and e) 200 nm \times 2.45 μm . The spectra show multiple Fabry-Pérot interference peaks, caused by reflection of guided light between the nanowire ends, which have been fitted by Lorentzian line shapes to determine the resonance energies. **b), d), f)** Energy-wavevector dispersion in the z -direction (along nanowire length) for the three wires shown in panels a), c) and e). The square data points indicate the Fabry-Pérot maxima, which have been placed in wavevector space at integer values of π/L_z with L_z the nanowire length. The solid lines show the results of numerical calculations for the fundamental HE_{11} guided mode including light-matter coupling with the CdS B-exciton (dotted horizontal line).²² Importantly, as is shown by the arrows indicating $2 \times \hbar g$, accurate fits could only be obtained by increasing the light-matter coupling strength (ΔE_{LT}) from 1x (bulk value) in panel d) to 4.5x in panel e), and to 6x in panel f).

7.3. Numerical mode volume calculations

To elucidate the strong dependence of light-matter coupling on individual nanowire dimensions, we numerically calculated the modal volumes of the confined fundamental modes in our nanowire waveguide cavities using full 3D and cross-sectional models. We calculated the mode volume V_m of our CdS nanowire waveguide cavities at the B-exciton resonance energy by numerically calculating the electric and magnetic fields of the purely photonic confined fundamental HE_{11} waveguide mode in waveguides with circular cross-sections laying on a SiO_2 substrate, using a finite element (FE) method (COMSOL). Maxwell's equations were solved for the magnetic field with continuous boundary conditions at the nanowire interfaces and a perfect magnetic conductor interface located at a distance of 10λ from the nanowire surface. The crystal structure was assumed to be uniaxial with the optical axis perpendicular to the length of the wire resulting in $\epsilon_x=\epsilon_z= 8.27$ for the in plane dimensions and $\epsilon_y=8.63$ for the out of plane direction y . Since the nanowire length is much longer than the lateral dimensions i.e. $L_z \gg L_x, L_y$, we can obtain the mode volume from the fields by using¹⁶:

$$V_{eff} = \frac{\int_V \epsilon(\vec{r}) |\vec{E}(\vec{r})|^2 d^3\vec{r}}{\left(\int_{V_{wire}} \epsilon(\vec{r}) |\vec{E}(\vec{r})|^2 d^3\vec{r} \right) / V_{wire}} = L * \frac{\int_A \epsilon(\vec{r}) |\vec{E}(\vec{r})|^2 d^2\vec{r}}{\left(\int_{A_{wire}} \epsilon(\vec{r}) |\vec{E}(\vec{r})|^2 d^2\vec{r} \right) / A_{wire}} \quad \text{Eq. 7.1}$$

$$V_m = \frac{\int_V \epsilon(\vec{r}) |\vec{E}(\vec{r})|^2 d^3\vec{r}}{(\epsilon(\vec{r}) |\vec{E}(\vec{r})|^2)_{\max}} = L/2 * \frac{\int_A \epsilon(\vec{r}) |\vec{E}(\vec{r})|^2 d^2\vec{r}}{(\epsilon(\vec{r}) |\vec{E}(\vec{r})|^2)_{\max}} \quad \text{Eq. 7.2}$$

with $V(A)$ the simulation volume (area), $V_{wire}(A_{wire})$ the actual nanowire volume (cross-sectional area), and the maximum values taken inside the wire domain. For large

volumes, Equation 7.1 returns the nanowire crystal volume, whereas at smaller nanowire diameters $V_{eff} > V$, caused by leaking of the waveguide field into the surroundings leading to a lower averaged field inside the nanowire. Calculated effective mode volumes were checked down to nanowire lengths of 2 μm by performing full three-dimensional FE and finite-difference time-domain (MEEP) calculations which yielded similar results.

Figure 7.3a shows a 2D projection of the obtained 3D electric field distribution $|\mathbf{E}|^2$ for the HE_{11} confined mode in a 200 nm x 5 μm nanowire at $\lambda=480$ nm resulting in a modal volume of 0.024 μm^3 ($5.3 (\lambda/n)^3$). The effective mode index (black line) of the confined HE_{11} mode as well as the modal volume at a fixed nanowire length of 2 μm (blue line) is shown as a function of nanowire diameter in Figure 7.3b. It can be seen that the mode volume steadily drops with decreasing nanowire width until the lowest mode volumes are reached at nanowire widths between 160 and 120 nm. Further reduction of the nanowire width results in a dramatically larger mode volume which coincides with the effective mode index dropping to that of the SiO_2 substrate (dashed line), indicating loss of confinement. Cross-sectional plots of the normalized electric field in nanowires with diameters of 520, 250, 160 and 110 nm (Figure 7.3c-f) respectively confirm that this increase in modal volume is caused by the loss of electric field confinement and leakage of the fields to the substrate. Thus, it is expected that minimum mode volume in our nanowire cavities can be achieved in the diameter range of 120-160 nm, given the same cavity lengths.

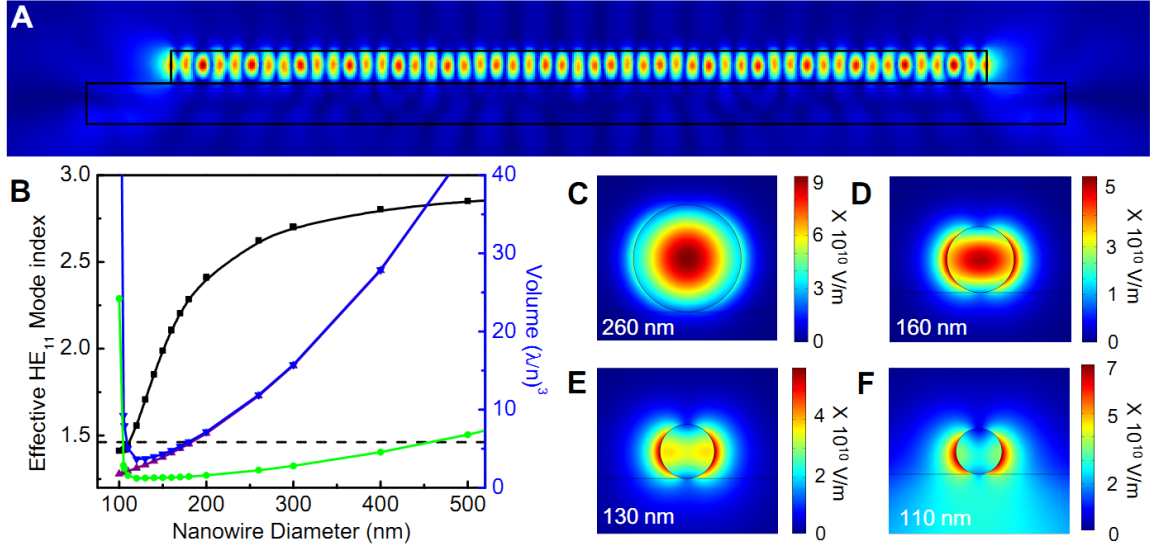


Figure 7.3: Numerical mode volume calculations of CdS nanowire waveguide cavities. **a)** 2D projection of the obtained 3D electric field distribution $|E|^2$ for the HE_{11} confined mode in a 200 nm wide and 5 μm long nanowire at $\lambda=480$ nm. **b)** Effective mode index of the fundamental HE_{11} mode (black line, left axis) and mode volume for a wire with a length of 10 μm (blue line, right axis) as a function of nanowire cavity width. As the nanowire width decreases, the mode volume and the effective mode index decrease until at a width of 120 nm the mode index attains the refractive index of SiO_2 substrate (dashed line), which causes a dramatic increase in mode volume. **c)-f)** Plots of the normalized electric field $|E|^2$ for nanowire diameters of **c)** 520 nm, **d)** 250 nm **e)** 160 nm and **f)** 110 nm, confirm that this increase in V_m is caused by loss of electric field confinement for the smallest cavities thus providing a lower limit on the nanowire cavity lateral dimensions.

7.4. Analysis of enhanced oscillator strengths

The results for the Rabi frequency, g , in 28 different nanowire cavities with diameters ranging from 130-575 nm and lengths ranging from 2.5 to 21 μm are summarized in Figure 7.4a, with square and circular data points for as-grown and SiO_2 surface-passivated nanowires respectively. As the mode volume is reduced, a transition from a region with constant coupling strength to a region with strongly enhanced, size-dependent coupling strength takes place. For large modal volume cavities, the coupling strength remains constant at $g=6.42 \times 10^{13}$ Hz over a large range spanning from $V_{\text{eff}} = 1.15$

to $3.5 \mu\text{m}^3$. This is consistent with the reported bulk polariton coupling strength in CdS of 41 meV (Rabi splitting, 82 meV) indicated by the blue dotted line in Figure 7.4a, and also obtained from:²⁶

$$g_{bulk} = \sqrt{\frac{\omega_0 \omega_{LT}}{2}} \quad \text{Eq. 7.3}$$

with ω_0 the CdS B-exciton resonance frequency and ω_{LT} its bulk longitudinal-transverse splitting. This consistency shows the validity of our Fabry-Pérot interference based experimental and theoretical analysis of these nanoscale cavities.

As we further decrease the cavity mode volume to values smaller than $1.15 \mu\text{m}^3$ ($210(\lambda/n)^3$), the coupling strength increases dramatically until at a mode volume of $0.079 \mu\text{m}^3$ ($20(\lambda/n)^3$) the coupling strength, g , becomes 2.4 times the bulk coupling strength ($2\hbar g=200$ meV). We note that for the smallest cavity sizes due to the large surface-to-volume ratio, surface passivation is essential to preserve the excitonic nature of the excitations²³ enabling the observation of such strongly enhanced coupling. In this regime of enhanced coupling strength, the data clearly follows the aforementioned square root dependence of coupling strength on inverse modal volume (Figure 7.4a, red dotted line) which demonstrates that we are now dealing with confined cavity-polaritons.^{2, 13, 26}

In order to extract the relevant oscillator strengths in our systems, we use the expression relating coupling strength with modal volume obtained for cavity-polaritons in microcavities, but with mode volume replaced by effective volume to account for the averaging effect of excitons not confined to positions at antinodes of the electric field:¹³

$$g_{cavity} = \sqrt{\frac{e^2}{4\epsilon_0\epsilon_r m_0} \frac{n(V)f(V)}{V_{eff}(V)}} \quad \text{Eq. 7.4}$$

with e the elementary charge, ϵ_0 the permittivity of vacuum, ϵ_r the relative permittivity of 8 for CdS, m_0 the electron mass, $n(V)$ the number of oscillators, $f(V)$ their oscillator strength and $V_{eff}(V)$ the mode volume. A good fit ($R^2=0.949$) of Equation 7.4 to the experimental data (Figure 7.4a, red dotted line) was obtained with effective oscillator strength $n(V) \times f(V) = 2.27 \times 10^7$ as a fit parameter. However, to determine the actual oscillator strength, f , for each nanowire, it is necessary to first consider its value in the bulk regime. To understand the constant coupling strength in the bulk regime, we propose that in this regime both $n(V)$ and $V_{eff}(V)$ are directly proportional to the nanowire cavity volume (see Figure 7.3b) while f remains constant, resulting in a constant effective oscillator strength per unit volume, and hence constant coupling strength.

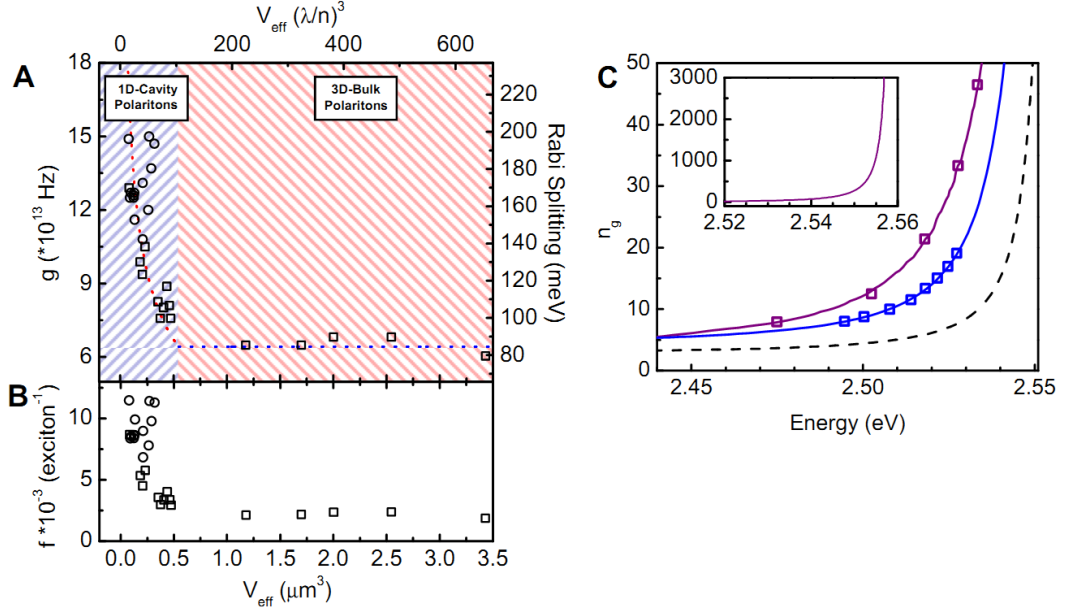


Figure 7.4: The transition from the bulk-polariton to the confined cavity-polariton regime. **a)** Coupling strength, g , vs. mode volume for 28 nanowire waveguides with diameters ranging from 160-575 nm and lengths ranging from 2.45 to 21 μm . For larger mode volumes, the coupling strength remains constant and can be fitted by Equation 7.4 with a constant quotient $n \times f / V_m$ (blue line). For smaller mode volumes, the coupling strength g increases by up to 2.4 times which can be fitted by Equation 7.4 with $n \times f = 3.06 \times 10^5$. **b)** In the bulk polariton regime the oscillator strength per oscillator f remains constant whereas in the cavity-polariton regime it peaks due to the increased electric field amplitude and giant oscillator strength effect. **c)** Group refractive index vs. energy for nanowires with Rabi splitting of 82 meV (bulk, dashed line), 140 meV (blue line), and 200 meV (purple line). The experimentally determined Fabry-Pérot peaks are indicated by squares. Inset: Group refractive index obtained for a wire with 200 meV Rabi splitting that is cut off at the highest observed guided emission for the lower polariton branch (see Figure 7.2e).

The validity of this hypothesis is proven by an excellent linear fit ($R^2 = 0.992$) to the values of $n(V) \times f(V)$ vs. crystal volume for the “bulk regime” data points, showing that the oscillator strength per oscillator remains constant in this bulk regime (see Figure 7.5). By extrapolating this linear relation to the volume per CdS exciton oscillator ($n(V) = 1$, $V_{\text{unitcell}}/2 = 4.98 \times 10^{-29} \text{ m}^3$) a value of $f_{\text{bulk}} = 2.27 \times 10^{-3}$ per B-exciton in wurtzite

CdS at 77 K is obtained, in excellent agreement with $f = 1.94 \times 10^{-3}$ in bulk CdS obtained from Dagenais et al.[†] This result also signifies that the exciton-polariton wavefunction is delocalized over the entire nanowire crystal, even up to our largest volume sample measuring 575 nm in diameter and 13.2 μm in length.

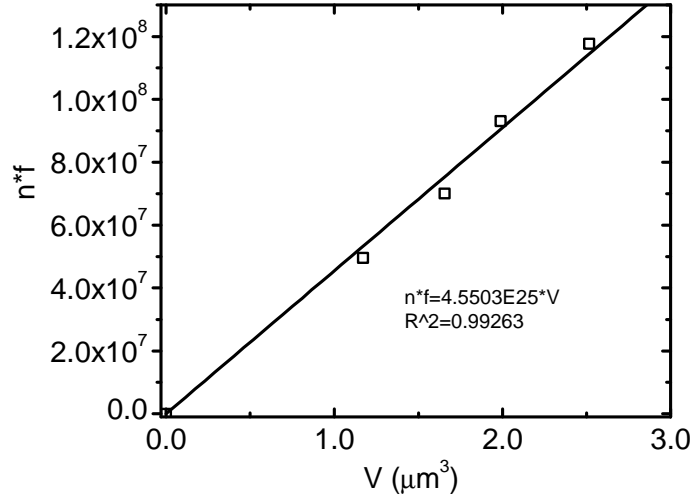


Figure 7.5: $n \times f$ for nanowires in the constant coupling strength regime plotted against real nanowire volume V .

In the cavity regime ($V_{eff} < 5.47 \times 10^{-19} \text{ m}^3$), values for the oscillator strength are obtained from Equation 7.4 by determining for each nanowire the value of $n(V)$ from the volume, the volume per oscillator, and the corresponding values of V_{eff} and coupling

[†] The explicit bulk oscillator strength for the B-exciton at 77K per molecule CdS can be calculated via:²⁸

$$f_{ex} = 2E_G E_{LT} \epsilon_b \frac{\epsilon_0 m_0}{e^2} \frac{\Omega}{\hbar^2} \quad \text{Eq. 7.5}$$

where E_G is the band gap energy, E_{LT} is the longitudinal-transverse splitting, ϵ_b is the background dielectric constant, and Ω is the volume of one CdS molecule. Using $E_G=2.582 \text{ eV}$,²⁹ $E_{LT}=1.4 \text{ meV}$,³⁰ $\epsilon_b=8$,³¹ and $\Omega=4.98 \times 10^{-29} \text{ m}^3$,²⁸ we obtain $f_{ex}=2.09 \times 10^{-3}$.

strength. The obtained oscillator strengths in the cavity regime are plotted as a function of V_{eff} in Figure 7.4b, where it can be seen that for the highest coupling strength the oscillator strength reaches a value of 1.15×10^{-2} , a sixfold enhancement over the bulk value. We note that the oscillator strength values obtained here represent upper limits because the exciton diffusion length in CdS is more than the nanowire diameters so that the excitons can preferentially move to positions of high optical field,³² making it necessary to account for this exciton distribution by using a volume in Equation 7.4 that lies in between the mode volume that would be used for oscillators at the antinodes of the optical field and the effective volume as used in this paper for a spatially averaged field (see Figure 7.3b).

Enhancement of exciton oscillator strengths is known to occur in semiconductor crystals when several oscillators coherently combine into one larger dipole with quadratically higher strength, mediated by coupling to the same optical mode.³³ The oscillator strength enhancement has an optimum value at intermediate crystal dimensions approximately equal to the wavelength of light in the material (~ 170 nm for CdS) due to the optimization of the number of oscillators constructively contributing to the dipole.³⁴³⁵ Therefore, we assign the observed enhanced oscillator strength in nanowires to such a polaritonic effect, where the crystal sizes are in between the quantum-confined and macroscopic regimes. We must also stress that our cavity dimensions are two orders of magnitude larger than those where quantum confinement effects in CdS arise, excluding these effects as the source of the enhanced oscillator strength and strong light-matter coupling.

We propose that the remarkable enhancement of light-matter coupling strength in these nanowire cavities is the result of two complementary processes; firstly, the reduction of modal volume directly results in increased coupling by increasing the electromagnetic energy density in the cavity, analogous to microcavities (Equation 7.4). This is corroborated by our experimental observation that shorter wires display higher coupling strength for a fixed diameter. Secondly, the formation of a coherent dipole with giant oscillator strength contributes strongly to the enhanced coupling strength at smaller modal volumes since in this regime the nanowire diameter approaches the optimum dipole size of ~ 100 nm for maximum oscillator strength. Although, we did not find an expected maximum in the coupling strength due to the significant evanescent field intensities for nanowire diameters smaller than ~ 120 nm (see Figure 7.3) precluding observation of Fabry-Pérot modes required for our analysis, our cavities provide an excellent natural match between minimal modal volume and maximal oscillator strength, resulting in the observed exceptional strong light-matter coupling.

Due to the increased coupling strengths, the group refractive index of the nanowires also increases dramatically, as shown in Figure 7.4c. The maximum group index enhancement for light that made at least a round trip in the cavity (Fabry-Pérot peaks) is sixfold when compared to the bulk group index (Figure 7.4c) and hundred-fold when compared to the light line in CdS, which occurs when there are no excitons present. The group index of light corresponding to the lower-polariton branch that traveled along the entire length of the nanowire (Figure 7.4c, inset) can even reach values three orders of magnitude larger than in the purely photonic case, although the propagation distance is small due to large damping (i.e. absence of Fabry-Pérot modes). This demonstrates that

the size-dependent strong-coupling can be used to tune the signal velocity over a wide range in nanowire waveguides and illustrates the importance of tunable light-matter coupling strength for slow-light applications such as switching and sensing.¹⁰

References

1. Hopfield, J.J. & Thomas, D.G. Polariton Absorption Lines. *Physical Review Letters* **15**, 22-25 (1965).
2. Weisbuch, C., Nishioka, M., Ishikawa, A. & Arakawa, Y. Observation of the coupled exciton-photon mode splitting in a semiconductor quantum microcavity. *Physical Review Letters* **69**, 3314-3317 (1992).
3. Klingshirn, C.F. *Semiconductor Optics* (Springer-Verlag, Berlin-Heidelberg-New York, 1997).
4. Yamamoto, Y., F.Tassone & Cao, H. *Semiconductor Cavity Quantum Electrodynamics* (Springer, Berlin Heidelberg, 2000).
5. Khitrova, G., Gibbs, H.M., Kira, M., Koch, S.W. & Scherer, A. Vacuum Rabi splitting in semiconductors. *Nature Physics* **2**, 81-90 (2006).
6. Kasprzak, J. et al. Bose–Einstein condensation of exciton polaritons. *Nature (London, United Kingdom)* **443**, 409-414 (2006).
7. Balili, R., Hartwell, V., Snoke, D., Pfeiffer, L. & West, K. Bose-Einstein Condensation of Microcavity Polaritons in a Trap. *Science (Washington, D. C., 1883-)* **316**, 1007-1010 (2007).
8. Deng, H., Weihs, G., Snoke, D., Bloch, J. & Yamamoto, Y. Polariton lasing vs. photon lasing in a semiconductor microcavity. *Proceedings of the National Academy of Sciences* **100**, 15118-15323 (2003).
9. Tsintzos, S.I., Pelekanos, N.T., Konstantinidis, G., Hatzopoulos, Z. & Savvidis, P.G. A GaAs polariton light-emitting diode operating near room temperature. *Nature (London)* **453**, 372-375 (2008).
10. Krauss, T.F. Why do we need slow light? *Nature Photonics* **2**, 448 (2008).
11. Todorov, Y. et al. Strong Light-Matter Coupling in Subwavelength Metal-Dielectric Microcavities at Terahertz Frequencies. *Physical Review Letters* **102**, 186402 (2009).
12. Vahala, K.J. Optical microcavities. *Nature (London, United Kingdom)* **424**, 839-846 (2003).
13. Reithmaier, J.P. et al. Strong coupling in a single quantum dot–semiconductor microcavity system. *Nature (London, United Kingdom)* **432**, 197-200 (2004).
14. Yoshie, T. et al. Vacuum Rabi splitting with a single quantum dot in a photonic crystal nanocavity. *Nature (London, United Kingdom)* **432**, 200-203 (2004).
15. Peter, E. et al. Exciton-photon strong-coupling regime for a single quantum dot embedded in a microcavity. *Physical Review Letters* **95**, 067401 (2005).
16. Andreani, L.C., Panzarini, G. & Gerard, J.M. Strong-coupling regime for quantum boxes in pillar microcavities: Theory. *Physical Review B: Condensed Matter and Materials Physics* **60**, 13276-13279 (1999).
17. Peter, E. et al. Exciton-photon strong-coupling regime for a single quantum dot embedded in a microcavity. *Physical Review Letters* **95** (2005).
18. Vugt, L.K.v. et al. Exciton-Polaritons Confined in a ZnO Nanowire Cavity. *Physical Review Letters* **97**, 147401 (2006).

19. Lidzey, D.G. et al. Strong exciton-photon coupling in an organic semiconductor microcavity. *Nature (London)* **395**, 53 (1998).
20. Tredicucci, A. et al. Controlled Exciton-Photon Interaction in Semiconductor Bulk Microcavities. *Physical Review Letters* **75**, 3906-3909 (1995).
21. Vugt, L.K.v., Piccione, B., Spector, A.A. & Agarwal, R. Size-Dependent Waveguide Dispersion in Nanowire Optical Cavities: Slowed Light and Dispersionless Guiding. *Nano Letters* **9**, 1684 (2009).
22. Vugt, L.K.v., Piccione, B. & Agarwal, R. Incorporating polaritonic effects in semiconductor nanowire waveguide dispersion. *Applied Physics Letters* **97**, 061115 (2010).
23. van Vugt, L.K. et al. Variable Temperature Spectroscopy of As-Grown and Passivated CdS Nanowire Optical Waveguide Cavities. *The Journal of Physical Chemistry A* **115**, 3827-3833 (2011).
24. Piccione, B., Vugt, L.K.v. & Agarwal, R. Propagation loss spectroscopy on single nanowire active waveguides. *Nano Letters* **10**, 2251 (2010).
25. Koteles, E.S. & Winterling, G. Direct Measurement of 3-Branch Exciton-Polariton Dispersion in Cds. *Physical Review Letters* **44**, 948-951 (1980).
26. Andreani, L.C. Confined Electrons and Photons: New Physics and Applications (eds. Burstein, E. & Weisbuch, C.) (Plenum Press, New York, 1993).
27. Li, H.Y., Ruhle, S., Khedoe, R., Koenderink, A.F. & Vanmaekelbergh, D. Polarization, Microscopic Origin, and Mode Structure of Luminescence and Lasing from Single ZnO Nanowires. *Nano Letters* **9**, 3515-3520 (2009).
28. Dagenais, M. & Sharfin, W.F. Linear- and nonlinear-optical properties of free and bound excitons in CdS and applications in bistable devices. *Journal of the Optical Society of America B* **2**, 1179 (1985).
29. Thomas, D.G. & Hopfield, J.J. Exciton Spectrum of Cadmium Sulfide. *Physical Review* **116**, 573 (1959).
30. Koteles, E.S. & Winterling, G. Direct Measurement of Three-Branch Exciton-Polariton Dispersion in CdS. *Physical Review Letters* **44**, 948 (1980).
31. Voigt, J., Sengner, M. & Ruckmann, I. Quantitative Analysis of Interference Structures in the Transmission Spectrum of Very Thin CdS Platelets. *Phys. Stat. Sol.* **75**, 213 (1976).
32. Oulton, R.F. Plasmon lasers at deep subwavelength scale. *Nature* **461**, 629-632 (2009).
33. Dicke, R.H. Coherence in spontaneous radiation processes. *Physical Review* **93**, 99-110 (1954).
34. Scheibner, M. Superradiance of quantum dots. *Nature Physics* **3**, 106-110 (2007).
35. van Vugt, L.K., Piccione, B. & Agarwal, R. Incorporating polaritonic effects in semiconductor nanowire waveguide dispersion. *Applied Physics Letters* **97**, 061115 (2010).

Chapter 8. **All-Optical Active Switching in Individual Semiconductor Nanowires**

Submitted for publication in Nature Nanotechnology.

Self-assembled, single-crystalline semiconductor nanowires have the ability to fulfill a number of roles relevant to nanophotonic applications: lasers,¹ electro-optic modulators,² waveguides^{3, 4} and photodetectors,⁵ all of which have been demonstrated. However, one key application which has not yet been demonstrated in semiconductor nanowires is all-optical active switching, an equally important tool relevant to photonic routing,⁶ modulation,⁷ and processing. Footprints smaller than comparable silicon-based devices⁸ and low propagation losses with respect to plasmonic nanowires⁹ position semiconductor nanowires as unique systems towards attainment of all-optical light manipulation on a technologically relevant dimensional scale. Nanowires from direct bandgap semiconductors such as ZnO, GaN, CdS and CdSe in particular are attractive for their wide range of bandgap energies as well as potential for both tunable electric field confinement and strong coupling between electron-hole pairs (excitons) to the light field¹⁰ due to the high oscillator transition strength and exciton stability to room temperature.¹¹ In this work, we exploit the highly nonlinear scattering behavior¹² of exciton-polaritons, to demonstrate reliable all optical active switch in single CdS nanowires by realizing a new device architecture and extend the concept to configure a NAND logic gate. Unlike switches fabricated from weakly coupled systems, which require large quality factor ($>10^4$) cavities and utilize changes in refractive index achieved with high excitation intensities,⁸⁻¹⁰ our nanowires do not rely on cavity quality,

nor do they require the high intensities necessary for the large refractive index changes under other forms of conventional optical bistability in active materials.¹³

8.1. Experimental setup

One of the biggest challenges to realize a nanowire-based optical switch is to be able to couple a suitable probe light into a nanowire waveguide. An ideal probe light should be bright with very narrow bandwidth, and most importantly, wavevector matched to the nanowire switch growth axis (k_z) for maximum in-plane coupling to the waveguide mode. Due to the wavevector mismatch for direct coupling of a free-space laser into a nanoscale waveguide in addition to large in-coupling losses at the length scales involved, it is not trivial to couple the probe beam in individual nanowires. In order to overcome this obstacle we developed a unique design utilizing a nanometer scale gap etched in a nanowire optical waveguide (Figure 8.1a) grown and passivated under the same conditions outlined in Chapter 5, which serves the critical functions of structurally isolating two optical waveguides while providing efficient optical coupling between them to inject the probe light generated by one segment into another via butt coupling. Such an arrangement requires perfectly aligned nanowire waveguides, which we achieved by “cutting” a small nanoscale region from a single nanowire optical waveguide (5 to 460 nm gaps) using the Ga⁺ source of a FEI Strata DB235 electron/focused Ga⁺ dual beam microscope (Figure 8.1a). Nanowires were centered at 20000x magnification using a 5 kV electron beam, tilted such that their growth axes were perpendicular to the ion source, and cut with 10 to 30 pA Ga⁺ beam current with nominal milling parameters (dwell time 1 μ s, overlap ranging from 40 to 60%) to achieve control over the gap size. Sample damage was minimal and not found to significantly affect photoluminescence properties.

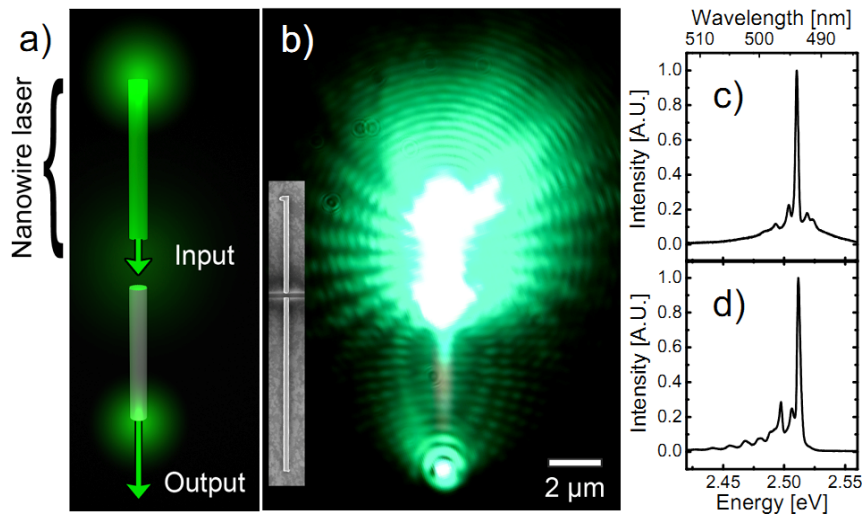


Figure 8.1: Creation of on-chip laser light sources for optical switching. **a)** Illustration of the switching device concept with a single CdS nanowire cut in two with a focused Ga ion beam, resulting in two nanowires of identical diameters aligned end-to-end, structurally isolated from one another and separated by a distance of 5 to 500 nm. A frequency-doubled Ti:Sapphire laser at 458 nm is used to optically pump the upper portion to lasing conditions; the resultant on-chip laser light emitted by the nanowire is then transmitted through the gap and waveguided to the bottom end facet. **b)** True color optical microscope image of a 10.9 μm long, 205 nm diameter CdS nanowire device at 77 K under the conditions explained in a). Note strong interference fringes emanating from both portions of the nanowire indicate successful transmission of laser light across the 160 nm wide ion-milled gap. Inset: SEM micrograph of the nanowire device. **c)** and **d)** Photoluminescence spectra collected using a position-sensitive photodetector positioned at the top (c) and bottom (d) end facets. Aside from minor changes due to Fabry-Pérot resonances in the lower portion and attenuation of short wavelengths, the two spectra are similar and the laser peak at 2.510 eV remains intact.

Following ion milling, substrates were then moved to a cryostat held at 77 K and one half of each “cut” nanowire was optically pumped to lasing conditions using a frequency-doubled pulsed Ti:Sapphire laser focused to a Gaussian spot size smaller than the nanowire segment (see Figure 2.2 and Figure 8.1b). The spectral output of the lasing portion (Figure 8.1c), shows laser peaks attributed to exciton-exciton scattering (Figure 8.2).¹ This on-chip laser output traversed the nanoscale gap and was waveguided through

the lower portion to the bottom nanowire end facet, resulting in a spectral output profile (Figure 8.1d) very similar to that of the input, and most importantly, maintaining the integrity of the most intense laser peak, thus satisfying all the required attributes of a “probe” for switching experiments.

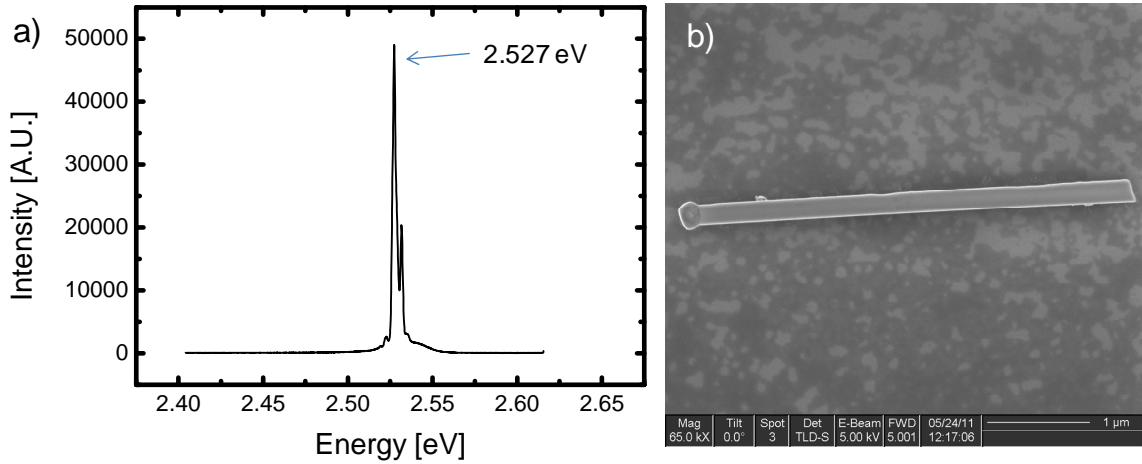


Figure 8.2: a) PL spectrum collected from nanowire end facet at 4.1 K showing laser emission at 2.527 eV, consistent with known literature values for exciton-exciton lasing in CdS nanowires.¹ b) SEM image of measured SiO₂-passivated CdS nanowire, 210 nm in diameter and 4.4 μm long.

8.2. Results

With a suitable probe light source in place, we then tested the feasibility of all-optical switching in individual nanowires (Figure 8.3a). With the upper portion continuously emitting probe light, a continuous wave Ar⁺ laser at 2.708 eV was focused to a Gaussian spot of width ~1 μm on the center of the lower portion (structurally unconnected to the on-chip nanowire laser). The Ar⁺ laser was repeatedly turned on and off while monitoring the output of the transmitted probe signal by collecting emission from the bottom end facet. The result of one such experiment for a nanowire with a 5 nm gap is shown in Figure 8.3b. As seen in the cascade plot, the on-chip laser continuously

emitted, and transmitted to the switch, a single laser peak centered at 2.510 eV. At $t=3$ s, 380 μW of Ar^+ laser power was applied, causing an immediate drop in transmitted laser intensity (the sharp peak corresponding to exciton-exciton scattering at 2.510 eV is completely extinguished) and instead only showing a much broader peak centered at 2.514 eV primarily attributed to CdS photoluminescence produced from the Ar^+ excitation waveguided to the end facet. Turning the Ar^+ laser off resulted in a complete restoration of on chip laser transmission (probe light), and the cycle was repeated five times to demonstrate repeatability. Both peaks were tracked as a function of time (Figure 8.3b, inset), showing an on/off ratio of approximately 5:1 for the transmitted laser peak. It should be noted that this is merely the measured ratio at 2.510 eV, and the actual switching capability is much higher: output collected when the Ar^+ laser is turned on is actually a nonlinear, overlapping combination of both the incoming probe light and local CdS photoluminescence excited by the Ar^+ laser, so a true ratio would take this into consideration and subtract out local photoluminescence. It should also be noted that the time scale of this demonstration is not meant to indicate the speed of the switching mechanism, as the sample geometry renders such measurements extremely difficult. Sufficiently high-frequency modulation of the system is not possible due to the low photon counts which would be result. To determine any possible influence of near-field coupling between the cavities and rule out the possibility of the Ar^+ laser affecting the operation of the nanowire laser probe source itself, the experiment was successfully repeated for multiple nanowires with cuts as wide as 460 nm (Figure 8.3c). Results for the largest cut width are shown in Figure 8.3c and Figure 8.3d, demonstrating relative indifference of the switching efficiency towards distance from the probe source.

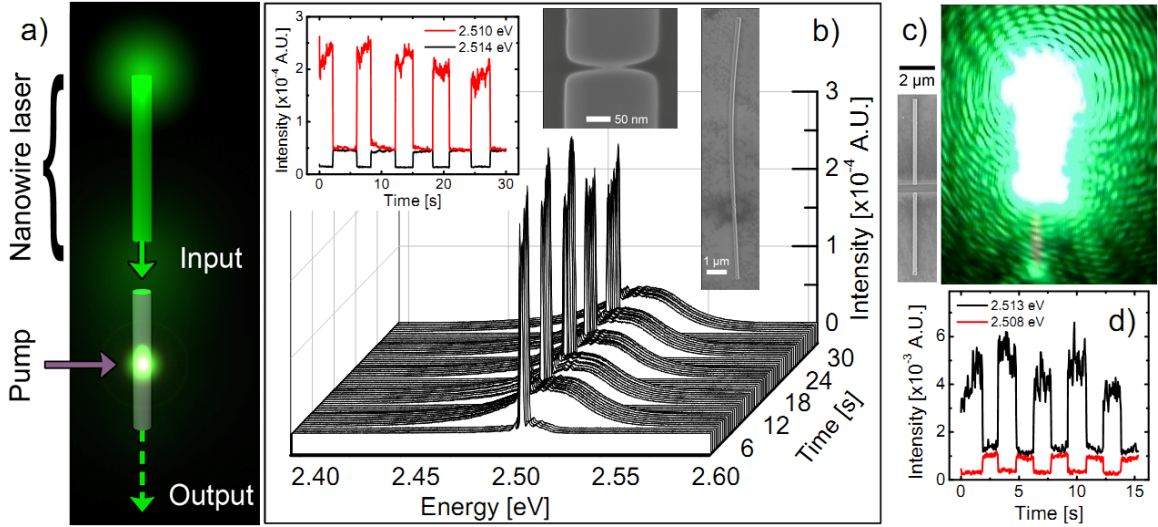


Figure 8.3: All optical active switching in CdS nanowires. **a)** Schematic of all-optical switching experimental setup. As in Figure 8.1a), on-chip laser light is generated in the top portion and transmitted across an ion-milled gap. An Ar⁺ laser at 457.9 nm is focused on the center of the bottom portion and turned on and off while the position-sensitive photodetector remains fixed on the bottom facet, collecting spectra once every 30 ms. **b)** Cascaded plot of the spectra collected from the bottom facet of a 13.2 μm long, 190 nm diameter nanowire device with a 5 nm gap as a function of time. At $t=0$ s, only the on-chip laser is on. Ar⁺ laser (380 μW of power) is turned on at 3s and turned off at 6s, and this process is repeated. Left inset: Cross-section of the waterfall plot, tracking the laser peak intensities at 2.509 and 2.514 eV. Right inset: SEM micrographs of the nanowire device with a 5 nm gap. **c)** Left: SEM micrograph of a 9.9 μm long, 205 nm diameter nanowire switching device with a 460 nm gap. Right: true color optical image of the top portion of the nanowire device being optically pumped to lasing at 77 K. **d)** Cross-sectional plot for the above nanowire device under an applied pump power of 165 μW (Ar⁺ laser to the bottom portion), tracking the laser peak intensities at 2.513 and 2.508 eV and demonstrating switching phenomena. Minor variations in detected nanowire laser intensity over the duration of each experiment are observable due to vibrations of the optical setup.

8.3. Analysis of Switching Mechanisms

Physical phenomena with the potential for actuating all-optical switching are well documented for large CdS platelets:¹³ among those relevant to the pump-probe geometry are induced absorption, whereby an absorptive spectral feature is redshifted onto the probe, and dispersive bistability, whereby cavity maxima and minima are tuned to switch

between transmissive and absorptive states, respectively. Induced absorption was ruled out in our nanowires by tracking the A and B free exciton resonances as a function of applied pump power (Figure 8.4). Had bandgap renormalization or significant nanowire heating occurred at higher applied pump power intensities, the transverse A- and B- free exciton resonances would redshift, potentially inducing absorption due to significant propagation losses documented³ on resonance. Nanowires which exhibited emission of free exciton peaks did not show any exciton resonance shifts to indicate renormalization or heating at high excitation intensities.

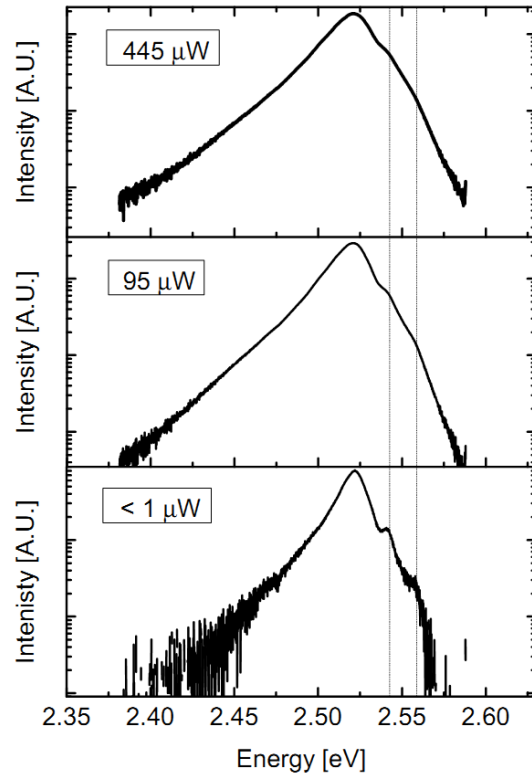


Figure 8.4: Photoluminescence collected from the center of a 200 nm diameter, 7.5 μm -long surface passivated CdS nanowire held at 77K under applied pump powers of 445, 95, and $< 1 \mu\text{W}$. Dotted lines at 2.544 and 2.559 eV show literature values¹⁴ for A- and B- free exciton resonances in CdS at 77K, respectively. The exciton resonances do not shift in energy with respect to applied pump power, ruling out induced absorption due to either bandgap renormalization or heating as a possible switch mechanism.

Dispersive bistability as a switching mechanism was ruled out by observing probe beam indifference towards shifting cavity resonances. The intense probe light was shown indifferent to relatively low Q -factor (< 500) Fabry-Pérot maxima and minima within the switch cavities, and light-matter coupling as determined from numerically calculated¹⁵ waveguide dispersion relations only increased up the highest intensities used, indicating that nanowires remained in the strong-coupling regime upon application of the Ar⁺ pump laser. Figure 8.5 demonstrates this for the nanowire presented in Figure 8.3c. Intrinsic nanowire longitudinal Fabry-Pérot-type cavity resonances are first revealed in the collected photoluminescence spectrum (Figure 8.5a, red line) upon application of a low-intensity pump beam (used to approximate cavity conditions with no applied pump). Individual cavity resonances redshift upon application of a 165 μ W pump (Figure 8.5a, blue line) due to an increase in excited carrier density.¹⁰ The incoming probe (Figure 8.5a, black line) traverses the switch at a cavity minimum with no applied pump, and a cavity maximum when the pump is turned on, meaning that cavity effects would dictate an enhancement in probe intensity upon application of the pump. The dramatic de-enhancement presented in Figure 8.3d shows this is not the case, and cavity-based switching is therefore ruled out as a potential mechanism.

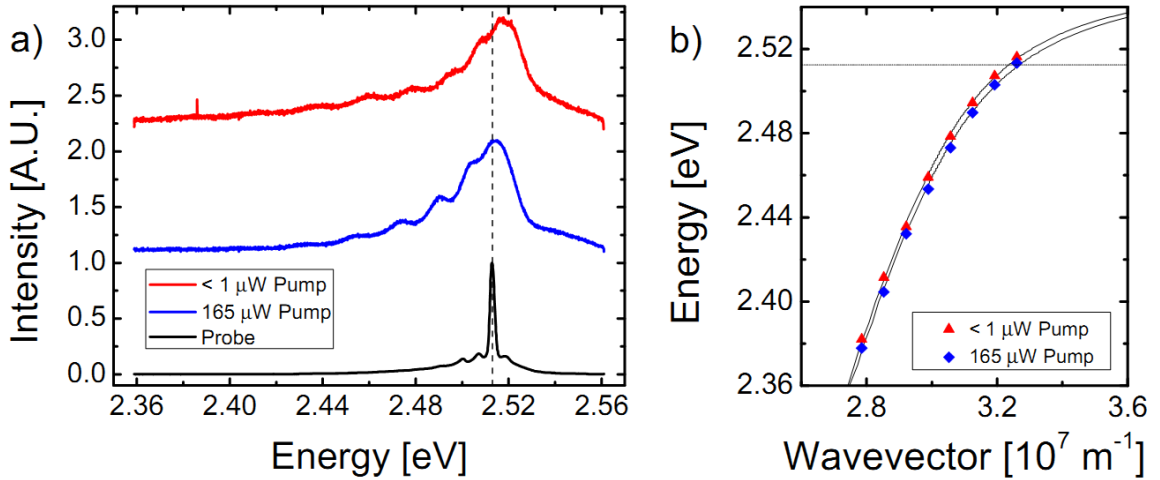


Figure 8.5: **a)** Photoluminescence spectra collected from bottommost facet of the nanowire discussed in Figure 8.3c. Spectra showing emission from application of $< 1 \mu\text{W}$ and $165 \mu\text{W}$ pump power are shown in red and blue, respectively, to highlight the spectral position of longitudinal Fabry-Pérot cavity⁴ resonances with respect to applied pump power. The spectrum of the probe light with no applied pump is shown in black. At low applied pump power, the probe is traversing a cavity minimum, while at high applied pump power, cavity resonances redshift, meaning the probe beam must now traverse a cavity maximum. Had cavity effects dominated switch behavior, amplification, rather than the de-amplification exhibited in Figure 8.3d, would occur upon application of the $165 \mu\text{W}$ pump. **b)** Experimental dispersions⁴ for $< 1 \mu\text{W}$ and $165 \mu\text{W}$ applied pump power shown in red and blue, respectively, plotted alongside numerically calculated¹⁵ dispersions (solid black lines) for each as well as the energy level of the probe (dotted black line). An increase in longitudinal-transverse B-exciton resonance splitting (ΔE_{LT}) from 5.4x to 6x bulk CdS values due to an increase in excited carrier density with increasing applied pump power¹⁰ causes a slight redshift in individual cavity resonances.

In evaluating remaining potential mechanisms for the observed switching in CdS nanowires, we note that in all our measurements switching occurred only between 2.482 and 2.531 eV, well within the 77 K CdS exciton-polariton thermalization bottleneck regime¹⁶ where light is of mixed photonic and excitonic character (polariton formation)¹⁰ and relaxation to lower momentum states is hindered when exciton-photon coupling is strong due to the small density of available states.^{17, 18} A collapse of this bottleneck and fast relaxation into lower momentum states is possible, however, in the low-density,

strong-coupling regime via stimulated polariton-polariton scattering¹⁹⁻²¹ by an applied probe beam to a final state where light is more photonic in character. Though enhancement from a spectrally well-defined pump resonant with the exciton-polariton bottleneck reservoir is a common focus of stimulated scattering literature, direct observation of initial state depopulation²² as well as scattering from nonresonant pump excitation into a broad distribution of final state momentums²³ have also been reported. Figure 8.6a shows a nanowire with 40 nm-wide cut, as well as optical images of the upper portion lasing under Ti:Sapphire excitation and the lower portion emitting photoluminescence under focused Ar+ excitation (Ti:Sapphire pumping off). Spectra collected from the bottom end facet are shown for each case in Figure 8.6b and Figure 8.6c, respectively, and the experimental waveguide dispersion for the lower portion as culled from the Fabry-Pérot peaks⁴ in Figure 8.6c is plotted alongside the numerically-calculated fundamental mode dispersion.¹⁵ As shown in Figure 8.6c, the addition of the Ar+ laser not only creates additional polaritons at the same momentum as the dominant laser peak at 2.505 eV, but also partially occupies many final states over the momentum range $k_z = 2.1 \times 10^7$ to $2.5 \times 10^7 \text{ m}^{-1}$. We believe scattering of the primary laser peak to lower momentum values (k_z), as can be seen (Figure 8.6e) by the simultaneous de-enhancement of the primary (2.505 eV) and enhancement of the secondary laser peaks at 2.497 eV upon the application of increasing Ar+ laser power (up to 450 μW) to be the mechanism of the observed switching phenomena in CdS nanowires. Other lower-momentum emission is also enhanced slightly, but preexisting state occupancy at the secondary peak momentum is higher and is likely the preferred final state¹⁸ as a result. The power dependence of integrated peak intensity loss is also nonlinear (Figure 8.6f),

further suggesting stimulated scattering of polaritons is responsible for the observed switching in nanowires.²² Because scattering occurs only where the Ar+ laser pump is focused, the interaction volume responsible for switching is extremely small ($\sim 0.015 \mu\text{m}^3$) and presents the limit on the miniaturization of nanowire switches.

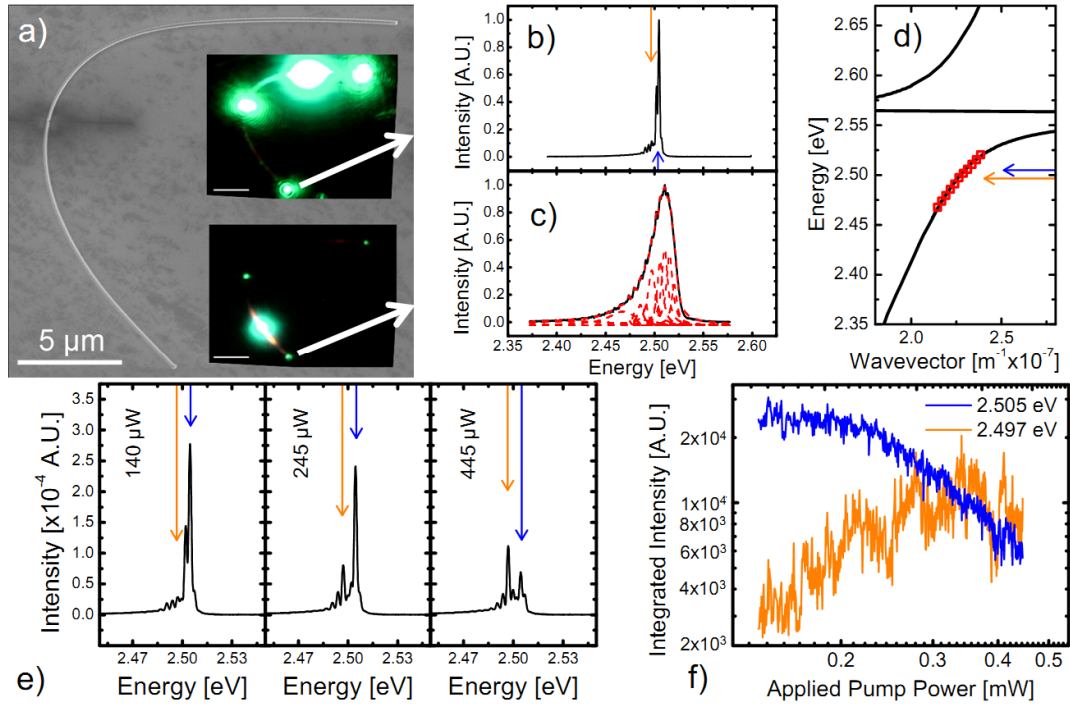


Figure 8.6: Mechanism of switching phenomena. **a)** SEM micrograph of a 31 μm long, 140 nm diameter nanowire device with a 40 nm gap. Top inset: Optical image of the device showing the top portion being optically pumped to lasing conditions at 77 K by a Ti:Sapph laser. Bottom inset: Optical image showing the bottom portion under focused Ar+ excitation at 77 K (Ti:Sapph laser is off). **b)** and **c)** Photoluminescence collected from the bottom end facet under Ti:Sapph and only Ar+ excitation, respectively. **d)** Numerically calculated¹⁵ dispersion (black line) of the switching portion (cavity length 13 μm), showing enhanced (3.1 times bulk CdS) light-matter coupling strength (ΔE_{LT}) for the nanowire,¹⁰ as determined from the Fabry-Pérot resonances (red squares) in **c)**. The 2.505 eV laser peak from **b)** is indicated with a blue arrow and the 2.497 eV laser peak is indicated with an orange arrow. **e)** Spectra collected from the bottom end facet of the switch with the nanowire laser emitting, and the bottom portion under 140, 245, and 445 μW applied Ar+ pump power. The 2.497 eV peak (orange line) is enhanced, while the 2.505 eV peak (blue line) is de-enhanced. **f)** Integrated intensity of both peaks plotted as a function of applied Ar+ power. Nonlinear de-enhancement of the 2.505 eV peak is observed simultaneously with the enhancement of the 2.497 eV peak, implicating a polariton scattering mechanism for the observed switching phenomena.

In order to demonstrate the utility of our devices in an optical processing context, we utilized the nanometer-scale gaps to create a working NAND logic gate (Figure 8.7) with functional completeness. Here, the outputs from the two nanowire switches are combined via evanescent coupling. The Ti:Sapphire laser simultaneously pumps both the segments to lasing and is continuously left on, creating two on-chip laser sources with the right laser cavity (“Laser 2”) emitting a primary peak centered at 2.499 eV, and the left laser cavity (“Laser 1”) outputting a primary peak centered at 2.511 eV. With no Ar⁺ pumps applied to the switch portions, this corresponds to the (0 0 1) logic condition.[†] When the Ar⁺ laser is focused on the right switch (“Input 2”) this stops transmission from Laser 2 and results in the red spectrum shown in Figure 8.7c, corresponding to the (0 1 1) logic condition. The reverse holds true and produces a (1 0 1) condition in Figure 8.7d, while centering the Ar laser spot directly between Inputs 1 and 2 (Figure 8.7e) results in cutting off nearly all transmission, corresponding to the 1 1 0 condition. The initial (0 0 1) condition differing slightly in Figure 8.7c-e (shown in black) is a result of system vibrations and reflects only instabilities inherent to the pinpoint optical pumping of Lasers 1 and 2 under an open-flow cryostat: the switching process itself is stable.

[†] The nanowire device in Figure 8.7 follows NAND gate logic. Each switch is considered “ON” (1) when the argon ion laser is on, and “OFF” (0) when the argon ion laser is off. Output states are considered “ON” (1) when the integrated intensity drop over the range of both laser peaks is less than 66%, and “OFF” (0) when the drop is greater than 83%.

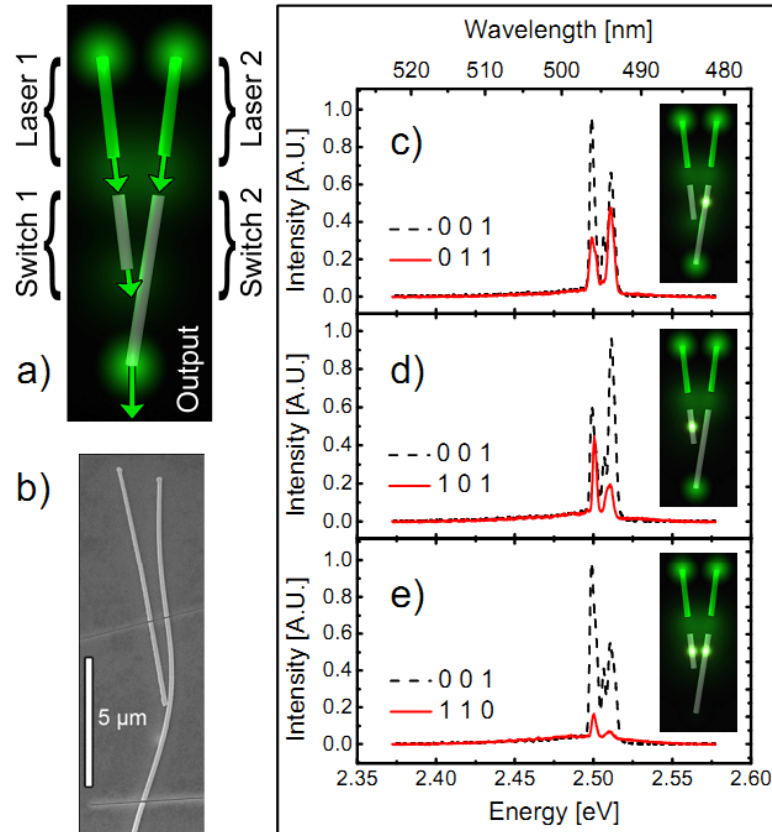


Figure 8.7: All optical nanowire NAND gate. **a)** Schematic of an all-optical nanowire NAND gate. The design requires two on-chip laser sources and two nanowire switches with their outputs combined through evanescent coupling in a waveguide. With no applied Ar⁺ pump, this illustration corresponds to the 0 0 1 logic condition. **b)** SEM micrograph of all-optical nanowire NAND gate device. **c-e)** Spectra collected from the output, illustrating the 0 0 1 (black) and 0 1 1 (red) (c), 0 0 1 (black) and 1 0 1 (red) (d), and 0 0 1 (black) and 1 1 0 (red) (e) logic conditions upon the application of 1 mW Ar⁺ power to each switch. Minor differences between the three initial (0 0 1) logic spectra are due to optical table vibrations.

In summary, we have demonstrated on-chip all-optical switching using individual CdS nanowires and leveraged the concept into a working all-optical, semiconductor nanowire NAND gate. We believe stimulated scattering of exciton-polaritons to be the most likely physical mechanism for the observed active switching phenomena. Reduced effective mode volumes, and therefore increased electromagnetic energy density, from

strong dielectric confinement in the radial direction¹⁰ allow for the onset of nonlinear optical phenomena at low powers in nanowire structures. The nanowire geometry and our unique experimental configuration have thereby enabled observation of this strong optical nonlinearity, occurring on a length scale facilitative of high device densities. The study underscores the potential of strong light-matter coupling in compound semiconductor nanostructures as well as the importance of continued research alongside their easily integrated yet weakly-interacting silicon counterparts.

References

1. Agarwal, R., Barrelet, C.J. & Lieber, C.M. Lasing in Single Cadmium Sulfide Nanowire Optical Cavities. *Nano Letters* **5**, 917-920 (2005).
2. Greytak, A.B., Barrelet, C.J., Li, Y. & Lieber, C.M. Semiconductor nanowire laser and nanowire waveguide electro-optic modulators. *Applied Physics Letters* **87**, 151103 (2005).
3. Piccione, B., Vugt, L.K.v. & Agarwal, R. Propagation Loss Spectroscopy on Single Nanowire Active Waveguides. *Nano Letters* **10**, 2251 (2010).
4. van Vugt, L.K., Zhang, B., Piccione, B., Spector, A.A. & Agarwal, R. Size-Dependent Waveguide Dispersion in Nanowire Optical Cavities: Slowed Light and Dispersionless Guiding. *Nano Lett.* **9**, 1684-1688 (2009).
5. Hayden, O., Agarwal, R. & Lieber, C.M. Nanoscale avalanche photodiodes for highly sensitive and spatially resolved photon detection. *Nat Mater* **5**, 352-356 (2006).
6. Keil, R. et al. All-optical routing and switching for three-dimensional photonic circuitry. *Sci. Rep.* **1** (2011).
7. Schönenberger, S. et al. Ultrafast all-optical modulator with femtojoule absorbed switching energy in silicon-on-insulator. *Opt. Express* **18**, 22485-22496 (2010).
8. Xu, Q. & Lipson, M. All-optical logic based on silicon micro-ring resonators. *Opt. Express* **15**, 924-929 (2007).
9. Guo, X. et al. Direct Coupling of Plasmonic and Photonic Nanowires for Hybrid Nanophotonic Components and Circuits. *Nano Letters* **9**, 4515-4519 (2009).
10. van Vugt, L.K., Piccione, B., Cho, C.-H., Nukala, P. & Agarwal, R. One-dimensional polaritons with size-tunable and enhanced coupling strengths in semiconductor nanowires. *Proceedings of the National Academy of Sciences* **108**, 10050-10055 (2011).
11. Hopfield, J.J. & Thomas, D.G. Polariton Absorption Lines. *Physical Review Letters* **15**, 22 (1965).
12. Tassone, F. & Yamamoto, Y. Exciton-exciton scattering dynamics in a semiconductor microcavity and stimulated scattering into polaritons. *Physical Review B* **59**, 10830-10842 (1999).
13. Wegener, M., Klingshirn, C., Koch, S.W. & Banyai, L. Three types of electronic optical bistabilities in CdS. *Semiconductor Science Technology* **1**, 366 (1986).
14. Thomas, D.G. & Hopfield, J.J. Exciton Spectrum of Cadmium Sulfide. *Physical Review* **116**, 573 (1959).
15. van Vugt, L.K., Piccione, B. & Agarwal, R. Incorporating polaritonic effects in semiconductor nanowire waveguide dispersion. *Applied Physics Letters* **97**, 061115 (2010).
16. Heim, U. & Wiesner, P. Direct Evidence for a Bottleneck of Exciton-Polariton Relaxation in CdS. *Physical Review Letters* **30**, 1205-1207 (1973).
17. Tassone, F., Piermarocchi, C., Savona, V., Quattropani, A. & Schwendimann, P. Bottleneck effects in the relaxation and photoluminescence of microcavity polaritons. *Physical Review B* **56**, 7554-7563 (1997).

18. Huang, R., Tassone, F. & Yamamoto, Y. Experimental evidence of stimulated scattering of excitons into microcavity polaritons. *Physical Review B* **61**, R7854-R7857 (2000).
19. Senellart, P. & Bloch, J. Nonlinear Emission of Microcavity Polaritons in the Low Density Regime. *Physical Review Letters* **82**, 1233-1236 (1999).
20. Dang, L.S., Heger, D., André, R., Bœuf, F. & Romestain, R. Stimulation of Polariton Photoluminescence in Semiconductor Microcavity. *Physical Review Letters* **81**, 3920-3923 (1998).
21. Boeuf, F. et al. Evidence of polariton stimulation in semiconductor microcavities. *Physical Review B* **62**, R2279-R2282 (2000).
22. Senellart, P., Bloch, J., Sermage, B. & Marzin, J.Y. Microcavity polariton depopulation as evidence for stimulated scattering. *Physical Review B* **62**, R16263-R16266 (2000).
23. Alexandrou, A. et al. Stimulated scattering and its dynamics in semiconductor microcavities at 80 K under nonresonant excitation conditions. *Physical Review B* **64**, 233318 (2001).

Chapter 9. **Future Work**

Though much progress has been made in the quantification of light-matter coupling strength, and the transition from three-dimensional bulk to one-dimensional cavity polaritons has been observed in a solid state system for the first time, there is still room for improvement in the theoretical modeling of active semiconductor nanowire waveguides. In “Model of Fabry-Pérot-type electromagnetic modes in a cylindrical nanowire,”¹ Bordo improved upon our models by treating nanowires as *finite* dielectric cylinders dielectric when solving Maxwell’s equations. In doing so, the Bordo model includes effects induced from electromagnetic fields originating at nanowire end facets, resulting in a wavelength-dependent “effective phase shift” for reflection of waveguided modes not taken into account in our infinite cylinder treatment. This more rigorous treatment could be combined with the dielectric function detailed in Chapter 6 for a more complete model of active nanowire waveguides and used to revisit our previous results, though the minor corrections to absolute wavevector predicted to occur when incorporating finite length effects in nanowires of our high length-to-diameter ratios may not be worth the significant additional computational overhead at present.

There are few experiments imaginable which would significantly benefit from the slight improvements offered by Bordo’s treatment; however, one which may be worth investigating involves the use of near-field scanning microscopy (NSOM). The 20-nm lateral resolution² made possible by exploiting the properties of evanescent waves close to a sample surface could allow for direct imaging of standing waves within individual nanowires, potentially aiding in experimental determination of absolute wavevectors (as

opposed to the “relative” wavevectors currently measured using the far-field Fabry-Pérot method) by iterating well-defined injected wavelengths and counting the number of maxima present in the resultant NSOM images. Comparing the obtained absolute experimental wavevectors to the Bordo model may well aid in revealing any remaining deficiencies in the theory. Attempts at evaluating the feasibility of this method were hampered by a limited range of available input wavelengths, but plans for ultimately attaching the frequency-doubled Ti:Sapph laser to the NSOM could allow for this in the future. In addition to utilizing NSOM for analysis, the nanowires themselves could potentially be used in a type of novel NSOM probe. In analogue to carbon nanotubes used as atomic force microscope (AFM) probes,³ active semiconductor nanowire waveguides attached to pulled-fiber NSOM probes could allow for enhanced spatial resolution in the transparent regime owed to their extremely high aspect ratios. Techniques for constructing such probes have been described elsewhere,⁴ placing the idea in the realm of plausibility.

In regards to other applications, the most logical step after demonstrating all-optical switching via successful light transmission across ion-milled gaps is utilizing them in some other context. Our unpublished results on the size-dependence of transmission across gaps as a function of ion beam cut width (Figure 9.1) show that transmission is very sensitive to minor variations in distance between source and detector, and this sensitivity could potentially be exploited. Introduction of a gas, analyte, or biological sample of interest between source and detector could alter transmission intensity through either a change in refractive index or scattering, while continuous monitoring of the waveguided output would allow for detection. Converting

the emitting half into an LED and the receiving half into a photodetector could also free the device from the confines of a far-field micro-photoluminescence setup and potentially see deployment in real-world applications.

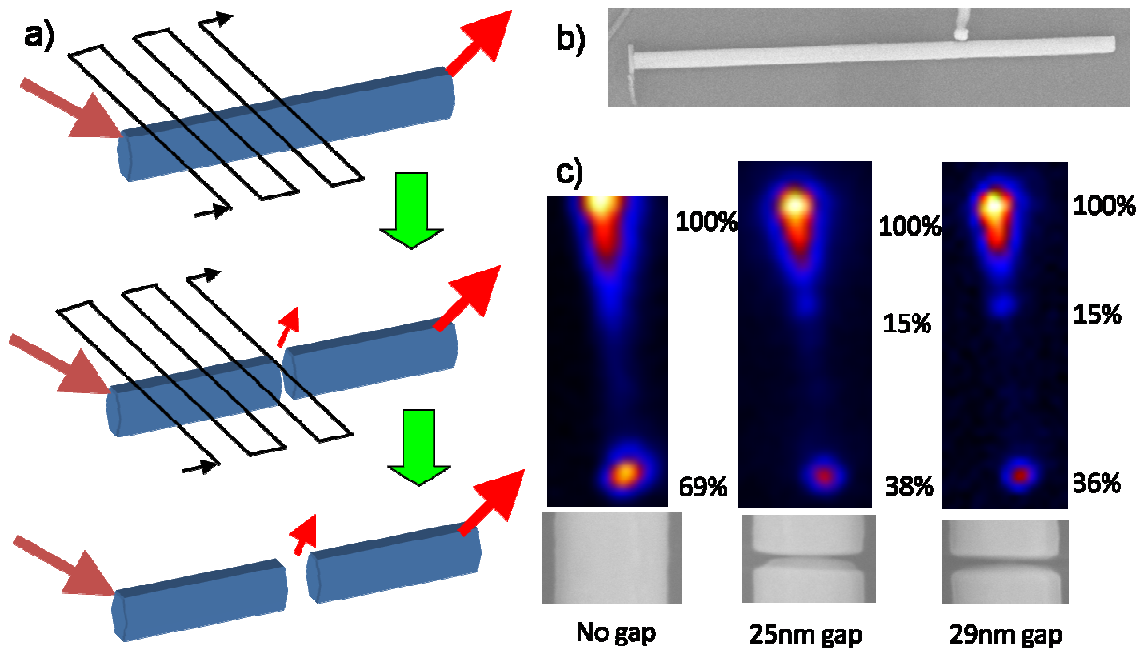


Figure 9.1: a) Scanning detection experiment setup. A laser spot is focused on one end facet of a nanowire, while a position-sensitive photodetector is scanned through the resulting optical image, resulting in the images shown in c). The experiment is repeated after a FIB cut is made in the nanowire, and again after further enlarging the cut width. b) SEM image of a 9.8 μm long, 345 nm wide ZnSe nanowire. c) Panchromatic detector scans of the nanowire in b), excited at the top end facet, shown with no cut, a 25 nm cut, and a 29 nm cut. After the first incision is made, light begins to escape from the cut, reducing the total light intensity waveguided to the bottom end facet. The total waveguided intensity is further reduced after enlarging the gap to 29 nm.

The ion milling process is primarily useful only in prototype nanowire device creation due to its severe speed limitations in comparison with the massively parallel processes used in commercial integrated circuit manufacture and substantial peripheral damage caused by even a well-focused ion beam. As shown in Figure 9.2, preliminary

attempts at healing damage through annealing show promise, but further experimentation is necessary to optimize the healing process. Such optimization would likely find use in healing nanostructures following other, similarly damaging, top-down modifications, potentially making this a worthwhile pursuit concurrent with construction of future devices.

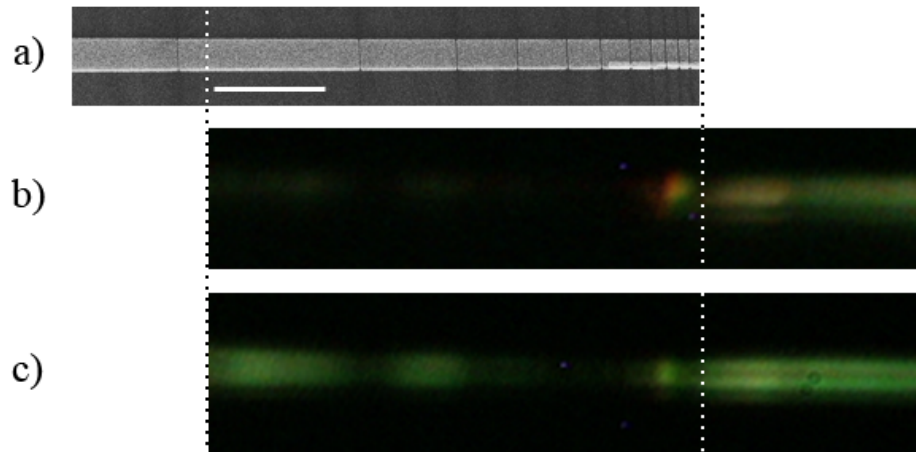


Figure 9.2: a) SEM image of CdS nanowire cut using a focused beam of gallium ions. Contrast has been artificially enhanced to accentuate the thin ~ 30 nm cuts. b) Real color optical image of the nanowire under diffuse, super-bandgap excitation. c) Real color optical image of the nanowire under the same excitation conditions after annealing under vacuum at 527 K for five hours. Scale bar in a) is $2 \mu\text{m}$ and common to all three images, which are aligned horizontally.

In addition to annealing, there are a number of potential avenues for future work similarly under the umbrella of more traditional materials science. The two materials grown during the course of this dissertation and the surface passivation techniques invoked hardly cover the range of what is possible using the existing experimental framework. With its bandgap of 3.37 eV at room temperature and exciton binding energy 60 meV,⁵ ZnO is an obvious choice for further study, as its excitons are stable well

beyond room temperature and non-toxicity could aid in gaining approval for commercial applications. Aside from merely altering the material of the nanowire core, however, changes during growth could result in branched structures,⁶ superlattice structures,⁷ or core-multishell structures,⁸ among other variations. Recent advances in superlattice growth are particularly interesting from an application standpoint, as single quantum dots grown along the nanowire length have allowed for both photon emission⁹ and detection.¹⁰ One can envision that with better control over dot placement, interaction with longitudinal Fabry-Pérot modes through placement at a cavity maximum could give rise to significant enhancement of the chosen wavelength via the Purcell effect.¹¹ Selective enhancement or suppression of chosen wavelengths should also be attainable through distributed Bragg reflectors built using controlled superlattice growth, though again, the accuracy and precision required of such a structure likely lie beyond the capabilities of the techniques currently used.

References

1. Bordo, V.G. Model of Fabry-Pérot-type electromagnetic modes of a cylindrical nanowire. *Physical Review B* **81**, 035420 (2010).
2. Durig, U., Pohl, D.W. & Rohner, F. Near-field optical-scanning microscopy. *Journal of Applied Physics* **59**, 3318-3327 (1986).
3. Wilson, N.R. & Macpherson, J.V. Carbon nanotube tips for atomic force microscopy. *Nat Nano* **4**, 483-491 (2009).
4. Yan, R. et al. Nanowire-based single-cell endoscopy. *Nat Nano* **7**, 191-196 (2012).
5. Numerical Data and Fundamental Relationships in Science and Technology (Springer-Verlag, Berlin, 1982).
6. Jung, Y., Ko, D.-K. & Agarwal, R. Synthesis and Structural Characterization of Single-Crystalline Branched Nanowire Heterostructures. *Nano Letters* **7**, 264-268 (2006).
7. Gudiksen, M.S., Lauhon, L.J., Wang, J., Smith, D.C. & Lieber, C.M. Growth of nanowire superlattice structures for nanoscale photonics and electronics. *Nature* **415**, 617-620 (2002).
8. Lauhon, L.J., Gudiksen, M.S., Wang, D. & Lieber, C.M. Epitaxial core-shell and core-multishell nanowire heterostructures. *Nature* **420**, 57-61 (2002).
9. Minot, E.D. et al. Single Quantum Dot Nanowire LEDs. *Nano Letters* **7**, 367-371 (2007).
10. van Kouwen, M.P. et al. Single quantum dot nanowire photodetectors. *Applied Physics Letters* **97**, 113108-3 (2010).
11. Proceedings of the American Physical Society. *Physical Review* **69**, 674-674 (1946).

Chapter 10. **Conclusions**

Explicit quantification of light-matter coupling strength in individual nanowires was not possible before the development of the tools presented in this dissertation. Beginning with the measurements of ZnSe nanowires in Chapter 3, we demonstrated strong size-dependent optical dispersions and group velocities. Using Fabry-Pérot resonances observed in micro-photoluminescence measurements, experimental energy-wavevector dispersion relations were determined from individual nanowires. The early theoretical model presented here, treating the nanowires as dielectric cylinders using an empirical approximation of the bulk refractive index from literature values, provided an adequate baseline for comparison in the transparent spectral region to show dispersionless guiding and slowed light close to electronic resonances.

With an experimental technique for evaluating optical properties of individual nanowires established, computer control over the excitation spot position was used to obtain propagation loss spectra, containing information from waveguide loss, loss to the substrate, and absorption within CdS. The method was found to significantly enhance the usable spectral range of conventional photoluminescence and again confirm the presence of exciton-polaritons in our nanowires. Peak positions were used to determine exact transverse exciton resonance frequencies, an important parameter for accurate dispersion modeling.

Following the development of surface passivation techniques, the waveguide dispersion model was refined to explicitly include interacting exciton resonances in the dielectric function. This modification to our earlier model is necessary to accurately

describe the experimentally observed dispersion of confined waveguide modes in active materials. Using the transverse exciton resonances determined from propagation loss spectroscopy, the numerical model was fit to experimental data using the longitudinal-transverse exciton splitting as a fitting parameter, again showing significant enhancement with regards to bulk material and paving the way for explicit quantification of the exciton transition oscillator strength.

With an accurate model in hand, we observed, for the first time, the transition from three-dimensional bulk exciton-polaritons to one-dimensional cavity-polaritons by reducing the cavity size, mostly by lateral optical confinement using CdS nanowire waveguides. The squeezing of the polaritons results in a drastic increase of the light-matter coupling strength, much beyond the bulk values, which we attribute to the superior surface properties, increased electric-field intensity inside the small mode volume cavities and matching the size of our cavities with the maximum coherent dipole length scale resulting in giant oscillator strength effects. Besides increasing the robustness of strong light-matter coupling for high carrier concentration applications such as polariton lasing and condensation, and a dramatic increase of the phase shift for optical bistability-based switching applications, the large coupling enhancement also reduces the signal group velocity by more than three orders of magnitude in comparison to the speed in vacuum.

Using the knowledge gleaned from all previous studies, we took advantage of the enhanced oscillator strength to demonstrate an application, in the form of all-optical switching. Probe light was injected into a switch using novel on-chip laser source, and

light was found to switch due to a stimulated polariton scattering mechanism. The output from multiple switches was combined to form an all-optical NAND gate, demonstrating the first such device to be constructed from nanowires.

The discoveries made during the course of this work have contributed to a small but significant step forward in understanding light-matter interaction within semiconductor nanostructures. It is hoped that the knowledge gained here will allow for further studies into this rich field, and perhaps lead to practical applications taking advantage of the unique properties made possible by the nanowire morphology. Regardless of impact, what was previously unknown is now slightly less so; this alone has motivated the work, and stands as an objective demonstration of its success.